EFFECTS OF THE RELATIVE SIZES OF INHOMOGENEITIES ON THE MECHANICAL BEHAVIOR OF COMPOSITE MATERIALS

PROJECT THESIS

Presented by

Silvia Zulaika Arkauz

Under the supervision of

Javier Aldazabal

Donostia-San Sebastián, may 2015

Held at the

Institute for Lightweight Design and Structural Biomechanics, TU Vienna

Under the supervision of

Helmut J. Böhm

CONTENTS

ABSTRACT

This thesis examines the influence of monomodal vs. bimodal aspect ratio on the effective elastic moduli of composites reinforced by aligned continuous cylindrical fibers. The elastic modulus of a porous material with analogous morphology is also analyzed.

For the transversally isotropic fiber reinforced composite, out of the five independent elastic constants, the transverse elastic and shear moduli give similar behaviors, increasing their values with decreasing diameter ratio for small volume fractions and reversing this behavior for higher volume fractions. Apart from this, the axial Young's modulus and Poisson's ratio do not show a significant dependence on diameter ratio, giving very similar or identical values for most of the analyzed cases. The axial shear modulus is found to be higher for greater difference between fiber diameters. Finally, the transverse bulk modulus and the transverse Poisson's coefficient show some minor differences only for some volume fractions, appearing to be largely independent of the diameter ratio.

When analyzing the porous material, similar results were obtained. The axial elastic modulus and the axial Poisson's coefficient do not depend on the diameter ratio. The transverse elastic and shear moduli show the opposite behavior to the non-porous case. The axial shear modulus and the transverse bulk modulus show some minor dependence on the diameter ratio, decreasing their values with decreasing ratio. Finally, the transverse Poisson's coefficient shows some dependence on the diameter ratio for higher volume fractions, increasing its value as the fiber diameters become more equal to each other.

1. INTRODUCTION

Composites of great stiffness and strength have emerged as lightweight materials of major technological significance in recent years. By a proper combination of, say fibers and a matrix, a wide range of elastic properties can be achieved. In order to fully use their potential, a more complete in-depth study is required as to how the properties of composites depend on the geometric parameters of their constituents.

The present work is concerned with the theoretical study of the elastic properties of materials containing reinforcing inhomogeneities, in the form of infinitely long fibers, aligned unidirectionally, or cylindrical voids of analogous geometry. It is assumed that both the fiber and matrix materials are linearly elastic, isotropic and homogeneous. The inhomogeneities are taken to be uniformly distributed in the transverse plane. Because of the fiber orientation the composite is macroscopically and randomly transversely isotropic; it therefore has five independent elastic constants. The problem, then, is to find expressions for the effective elastic moduli of the reinforced material in terms of the geometry of the fibers, characterized here by the diameter ratio, and the properties of the composite at various fiber concentrations.

1.1 IMPORTANCE OF COMPOSITE MATERIALS

It is a truism that technological development depends on advances in the field of materials. One does not have to be an expert to realize that the most advanced turbine or aircraft design is of no use if adequate materials are not available to bear the service loads and conditions. Whatever the field may be, the final limitation on advancement depends on materials. Composite materials in this regard represent a giant step in the ever-constant endeavor of optimization in materials.

Strictly speaking, the idea of composite materials is not a new or recent one. Nature is full of examples wherein the idea of composite materials is used. The coconut palm leaf, for example, is essentially a cantilever using the concept of fiber reinforcement. Wood is a fibrous composite: cellulose fibers in a lignin matrix. The cellulose fibers have high tensile strength but are very flexible (i.e. low stiffness), whereas the lignin matrix joins the fibers and furnishes the stiffness. Bone is yet another example of a natural composite that supports the weight of various members of the body.

In addition to these naturally occurring composites, there are many other engineering materials that are composites in a very general way and that have been in use for a very long time. Rubber containing carbon black, Portland cement or asphalt mixed with sand, and glass fibers in resin are common examples. Thus, we see that the idea of composite materials is not that recent. Nevertheless, one can safely mark the origin of the distinct discipline of composite materials at the beginning of the 1960s. A concerted research and development effort in composite materials began in 1965. Since the early 1960s, there has been an increasing demand for materials that are stiffer and stronger yet lighter in fields as diverse as aerospace, energy and civil engineering. The demands made on materials for better overall performance are so great and diverse that no one material can satisfy them. This naturally led to a resurgence of the ancient concept of combining different materials in an integral-composite material to satisfy the user requirements [1].

Such composite material systems result in a performance unattainable by the individual constituents, and they offer the great advantage of a flexible design; that is, one can, in principle, tailor-make the material as per specifications of an optimum design. This is a much more powerful statement than it might appear at first sight. It implies that, given the most efficient design of, say, an aerospace structure, an automobile, a boat, or an electric motor, we can make a composite material that meets the need. Composites have introduced extraordinary fluidity to design engineering, in effect forcing the designer-analyst to create a different material for each application as he pursues savings in weight and cost [1, 2].

The fact that our society has become very energy conscious must also be considered, as it has led to an increasing demand for lightweight yet strong and stiff structures in all walks of life. Composite materials are increasingly providing the answers. Glass fiber reinforced resins have been in use since the early twentieth century. They are very light and strong materials although their stiffness (modulus) is not very high, mainly because the glass fiber itself is not very stiff. The third quarter of the twentieth century saw the emergence of the so-called advanced fibers of extremely high modulus, for example boron, carbon, silicon carbide and alumina. These fibers were used for reinforcement of resin, metal and ceramic matrices. Fiber reinforced composites have been more prominent than other types of composites for the simple reason that most materials are stronger and stiffer in the fibrous form than in any other form. By the same token, it must be recognized that a fibrous form results in reinforcement mainly in fiber direction. Transverse to the fiber direction, there is little or no reinforcement [1, 3].

There may also be specific non-mechanical objectives for making a fibrous composite. For example, creating an abrasion- or corrosion-resistant surface or solving the problem of flux-pinning in superconductors [1].

1.2 STATE OF THE ART OF MICROMECHANICAL MODELING

1.2.1 CONTEXT OF MICROMECHANICAL MODELING

Micromechanical methods allow evaluating the full homogenized stress and strain tensors for any pertinent loading condition and for any pertinent loading history. Compared to semi-empirical constitutive laws, micromechanically based constitutive models have both a clear physical basis and an inherent capability for “zooming in” on the local phase stresses and strains by using localization procedures [4, 17].

The input data needed for a micromechanical study is related to the constituents’ defining data. Fiber material properties as well as matrix material properties have to be introduced; apart from this, the fiber volume fraction is also a given data that must be entered to the micromechanical model. The composite’s properties are evaluated from the mentioned input data as a result of the micromechanical model.

The results obtained from micromechanical studies on continuously reinforced composites correspond to a single unidirectional layer, which is later used as input data for Lamination Theories’ purposes. The laminate model is used to describe laminated solids and shells. In this construction, adjacent layers (or laminae, or plies) are arranged as shown in the figure below.

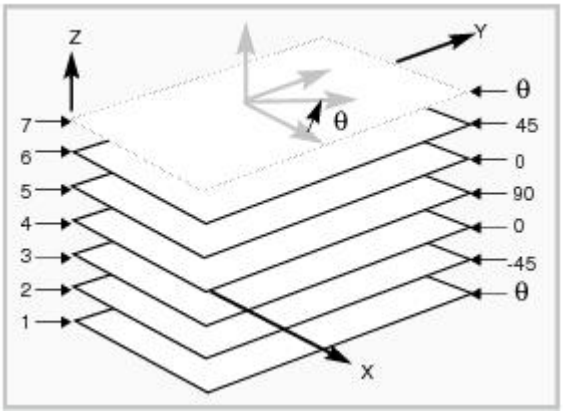

FIGURE 1: LAMINATE DEFINITION CONVENTIONS

The orientation of each layer is defined by a single constant angle Θ. Each layer may be a unique material and have a unique constant thickness. The laminate model

uses Classical Lamination Theory to calculate the membrane, bending and membrane-bending coupling stiffness matrices for a laminated shell [13].

The input data for the lamination model are the results obtained from micromechanics as well as the unidirectional layer's thickness and orientation. After applying lamination theories, shell stiffnesses are obtained.

1.2.2 MODELING APPROACHES

The following paragraphs quite closely follow reference [4].

The evaluation of the local responses of the constituents is especially important for studying and evaluating local strength relevant behavior, such as the onset and progress of plastic yielding or damage, which can, of course, have major repercussions on the macroscopic behavior. For valid descriptions of local strength responses details of the microgeometry tend to be of major importance and may, in fact, determine the macroscopic response.

Because for realistic phase distributions the analysis of the spatial variations of the microfields in large volume elements tends to be beyond present capabilities, approximations have to be used. For convenience, the majority of the resulting modeling approaches may be treated as falling into two groups. The first of these comprises methods that describe interactions, e.g., between phases or between individual reinforcements, in a collective way in terms of phase-wise uniform fields. This first group comprises:

Mean-Field Approaches (MFAs) and related methods: the microfields within each constituent of an inhomogeneous material are approximated by their phase averages. The phase geometry enters these models via statistical descriptors, such as volume fractions, phase topology, reinforcement aspect ratio distributions, etc.

Mean-field approaches tend to be formulated in terms of phase concentration tensors, they pose low computational requirements, and they were highly successful in describing the thermoelastic response of inhomogeneous materials. Their use in modeling nonlinear composites is a subject of active research. Their most important representatives are effective field and effective medium approaches. MFA implicitly postulate the existence of a representative volume element and typically assume some idealized statistics of the phase arrangement at the microscale.

Variational Bounding Methods: variational principles are used to obtain upper and (in many cases) lower bounds on the overall elastic tensors, elastic moduli, secant moduli, and other physical properties of inhomogeneous materials, the

microgeometries of which are described by statistical parameters. Many analytical bounds are obtained on the basis of phase-wise constant stress polarization fields. Bounds are tools of vital importance in assessing other models of inhomogeneous materials. Furthermore, in many of the cases one of the bounds provides good estimates for the physical property under consideration, even if the bounds are rather slack [18].

The second group of approximations is based on studying discrete microgeometries, for which they aim at evaluating the microfields, thus fully accounting for the interactions between phases. It includes:

Periodic Microfield Approaches (PMAs), also referred to as periodic homogenization schemes or unit cell methods. In these methods the inhomogeneous material is approximated by an infinitely extended model material with a periodic phase arrangement. The resulting periodic microfields are usually evaluated by analyzing repeating unit cells via analytical or numerical methods. Unit cell approaches are often used for performing materials characterization of inhomogeneous materials in the non-linear range, but they can also be employed as micromechanically based constitutive models. The high resolution of the microfields provided by PMAs can be very useful in studying the initiation of damage at the microscale. However, because they inherently give rise to periodic configurations of damage and patterns of cracks, PMAs are not suitable for investigating phenomena such as the interaction of the microgeometry with macroscopic cracks.

Periodic microfield approaches can give detailed information on the local stress and strain fields within a given unit cell, but they tend to be computationally expensive. This approach is the main method that was used to achieve the goals of this project.

Windowing approaches: subregions (“windows”), which are usually of rectangular or hexahedral shape, are randomly chosen from a given phase arrangement and subjected to boundary conditions that guarantee energy equivalence between the micro- and macroscales. Accordingly, windowing methods describe the behavior of individual inhomogeneous samples rather than of inhomogeneous materials and give rise to apparent rather than effective macroscopic responses. For the special cases of macrohomogeneous stress and strain boundary conditions, respectively, lower and upper estimates and bounds on the overall behavior of the inhomogeneous material can be obtained.

Embedded Cell or Embedding Approaches: the inhomogeneous material is approximated by a model consisting of a “core” containing a discrete phase

arrangement that is embedded within some outer region to which far field loads are applied. The material properties of this outer region may be described by some macroscopic constitutive law, they can be determined self-consistently or quasi-self-consistently from the behavior of the core, or the embedding region may take the form of a coarse description and/or discretization of the phase arrangement. ECAs can be used for materials characterization, and they are usually the best choice for studying regions of special interest in inhomogeneous materials. They can resolve local stress and strain fields in the core region at high detail, but tend to be computationally expensive. [4]

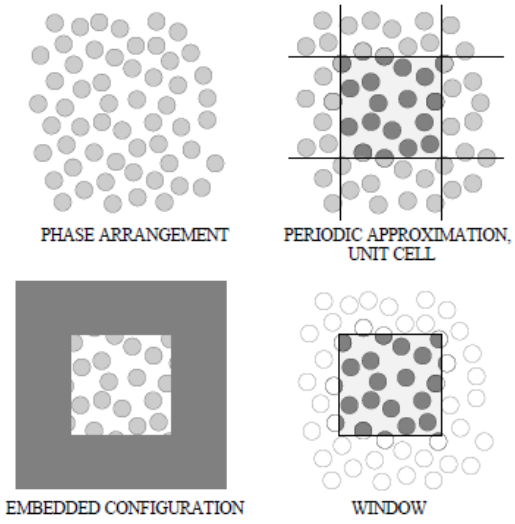

FIGURE 2: RANDOM MATRIX-INCLUSION MICROSTRUCTURE AND THE VOLUME ELEMENTS USED BY DIFFERET METHODS [4]

1.2.3 CHOSEN APPROACHES

Mean field approaches were used in this project to obtain analytical results for both the composite and the porous material. Unlike full-field approaches only partial information about the microstructure is needed in order to solve the micromechanical problem. Only material properties and volume fractions are needed in order to determine the effective properties analytically, this simplicity being one of the main advantages of mean field approaches [14]. Apart from this, MFAs also predict correctly the qualitative features of a system in most cases.

The essence of the mean-field theory is the assumption of statistical independence of the local ordering. In this way, all the reinforcement interaction terms considered in numerical approaches are replaced by an effective “mean field” term. In this way, all the information on correlations in the fluctuations is lost.

Two bounding methods were used in order to provide analytical bounds for the computed numerical values:

The first of them are the Hashin-Shtrikman-Type bounds; they are formulated in terms of a homogeneous reference material and of stress polarization fields that describe the difference between microscopic stress fields in the inhomogeneous material and a homogeneous reference medium [16].

The studied case in this thesis consists of a macroscopically transversely isotropic composite that consists of an isotropic matrix reinforced by aligned continuous isotropic fibers. A set of scalar Hashin-Shtrikman bounds applies to this kind of composites [16].

On the other hand, three-point bounds were used in order to provide additional limits for the obtained numerical values. These bounds require statistical information on the phase arrangement, and are significantly tighter that Hashin-Shtrikman type expressions [4].

Three-point bounds can tell the difference between composites reinforced by inhomogeneities of different sizes. However, such data at present is only available for spherical particles, see, e.g. [23], but not for aligned fibers.

The aim of this thesis is, as mentioned before, the analysis of the influence of relative fiber diameters on the mechanical behavior of composite and porous materials. These are second order effects that are much weaker than the ones of, say, fiber volume fraction or phase properties. Numerical methods appear to be well suited for catching these minor differences, providing additional understanding of the stiffness behavior in composite and porous materials. Therefore, the periodic microfield approach was the major method used to analyze the composites' behavior.

2. METHODS

2.1 BASIC CONCEPTS OF UNIT CELL MODELS

Unit cell methods are an approach to studying the stress and strain fields in periodic configurations. This is achieved by describing the microgeometry with a periodically repeating unit cell to which the investigations may be limited without loss of information [4].

Periodic geometries and appropriate boundary conditions must be set to make a correct use of unit cell models. Figure 3 shows two examples of geometries modeled with unit cells.

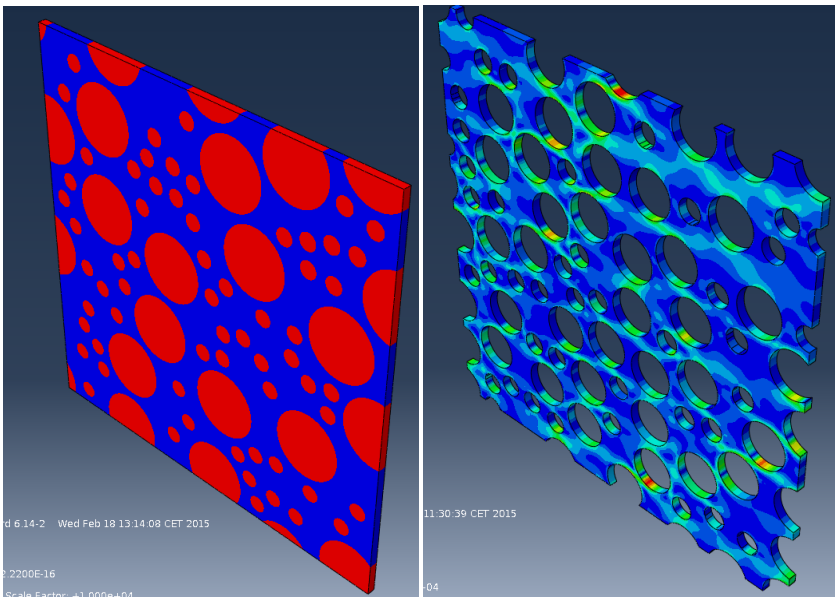

FIGURES 3: EXAMPLES OF UNIT CELLS – COMPOSITE (LEFT) AND POROUS MATERIAL (RIGHT)

The main disadvantage of the unit cell approach is oversimplification: this approach requires a high regularity of the material structure. Such materials do not actually exist, as neither do homogeneous loading conditions.

The main advantages of this approach are that it does not require excessive computational effort for using relatively fine grained geometrical descriptions, and that it allows the study of complex effects by running relatively simple computational analysis [4, 5].

Unit cell models allow studying, the following issues[5]:

- Effect of the arrangement of phases on the mechanical behavior of the composite. Evaluation of the stress and strain fields in relevant microgeometries at high resolution.

- Mechanisms of damage initiation and failure behavior, which may depend on details of material microgeometry.
- Initial stages of void formation and growth.

2.1.1 Unit Cell Models for Composites Reinforced by Unidirectional Continuous Fibers

Composites reinforced by continuous, aligned fibers typically show a statistically transversely isotropic overall behavior that can be studied well with periodic homogenization. Materials characterization with the exception of the overall axial shear behavior can be carried out with two-dimensional unit cell models employing generalized plane strain conditions. To analyze the overall axial shear response (required for obtaining macroscopic elasticity tensors) three-dimensional models with appropriate periodicity boundary conditions are needed [4].

In many cases simple periodic microgeometries do not provide truly satisfactory descriptions or reinforced materials, as most actual composites show considerable randomness in their microstructure.

As mentioned above, microgeometries of real inhomogeneous materials are at least to some extent random, and, in the majority of cases, their detailed phase arrangements are highly complex. As a consequence, exact expressions for the mechanical strain and stress concentration tensors as well as for the microscopic strain and stress fields cannot generally be given. Therefore approximations must be introduced. These approximations are typically based on the hypothesis that the heterogeneous material is statistically homogeneous. This implies that sufficiently large volume elements selected at random positions within the sample have statistically equivalent phase arrangements and give rise to the same averaged material properties [4].

2.1.2 Representative Volume Elements

Ideally, the homogenization volume should be chosen to be a proper representative volume element (RVE); it must be of sufficient size to contain all information necessary for describing the behavior of the composite. Representative volume elements were defined by requiring them to be statistically representative of the geometry, the resulting “geometrical RVEs” being independent of the physical property to be studied. Physical RVEs are defined by requiring all such volume elements to give identical predictions of a given physical property; the size of physical RVE in general depends on the property considered.

An RVE must be sufficiently large to allow a meaningful sampling of the microfields and sufficiently small for the influence of macroscopic gradients to be negligible and for an analysis of the microfields to be possible [4].

2.1.3 Statistical Volume Elements

To approximately meet the requirement of Representative Volume Elements to be statistically representative of the geometry, Statistical Volume Elements (SVEs) were used in this thesis. As SVE on its own is known to be of insufficient size to be a proper representative volume element. Nevertheless, ensemble averaging over a number of results obtained from sets of SVEs can be used to obtain estimates for the effective material properties, as a number of SVEs of comparable size pertaining to a given inhomogeneous material are realizations of the same statistical process. [4]

The number of different statistical volume elements required for a given level of accuracy of the ensemble averages decreases as the sizes of the SVEs increase. To assess the quality of the ensemble averaged results obtained from sets of SVEs, confidence intervals were proposed in the literature [19]. In this context an error measure can be defined in terms of the standard deviation S(Y) of some given modulus or tensor element Y, as:

$$err(Y) = 1.96\, S(Y)/\sqrt{n_{sve}} \quad (1)$$

Here n_{sve} is the number of statistically equivalent SVEs used in ensemble averaging [4].

2.1.4 Periodicity boundary conditions

Boundary conditions for unit cells must be specified in order to avoid gaps and overlaps between neighboring unit cells. In this work, periodicity boundary conditions were used, the necessary tools for doing so being available at the ISLB.

To describe a two-dimensional periodic phase arrangement, a suitable unit cell and two linearly independent periodicity vectors (p_1 and p_2) are required. These periodicity vectors are neither unique nor do they have to be orthogonal. For any given periodic microgeometry the “minimum unit cells” have the same volume but can take a wide range of shapes as shown in Figure 4.

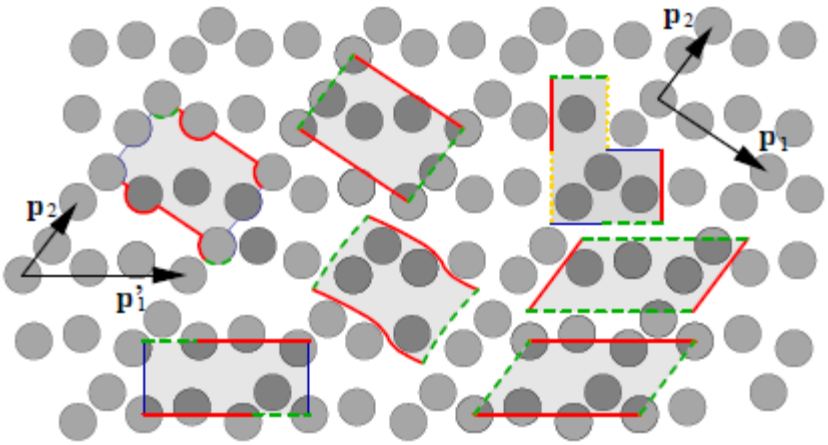

FIGURE 4: SEVEN EQUIVALENT PERIODIC UNIT CELLS [4]

The surfaces of periodic unit cells are made up of pairs of “homologous faces”; in Figure 4 such pairs are drawn in the same color and line style. In two-dimensional cases there are at least two and in three-dimensional cases at least three such pairs of faces.

For the present work, a standardized nomenclature was used for the faces, edges and vertices of three-dimensional unit cells as shown in Figure 5. The designations N, S, E, W, T and B stand for north, south, east, west, top and bottom, respectively. the following type of three dimensional periodic unit cell was used:

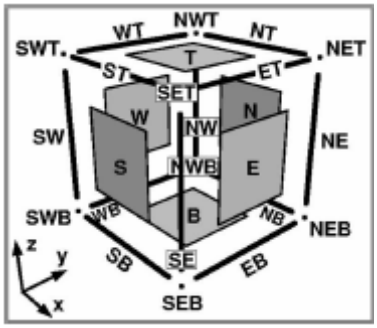

FIGURE 5: CUBE SHAPED PERIODIC UNIT CELL [4]

Neighboring unit cells must fit into each other in both undeformed and deformed states. To achieve this objective, equation (2) maybe used, which allows expressing, for each pair of surface elements, periodicity boundary conditions in the small strain regime:

$$\Delta U_k = U_{k+} - U_{k-} = U(S_k + C_k) - U(S_k) = \langle \varepsilon \rangle * C_k \qquad (2)$$

Here S_k and $S_k + C_k$ are the position vectors of pairs of “homologous” points on the surface elements k^- and k^+ respectively. These surface elements may correspond,

for example, to the faces N and S. On the other hand, u_{k-} and u_{k+} are the displacements at this pair of homologous points, and $\langle\varepsilon\rangle$ is the macroscopic strain tensor.

The vector linking the homologous points in a deformed state is:

$$C_{k,def} = C_k + \Delta U_k \tag{3}$$

The special case of an initially rectangular two-dimensional unit cell is shown in Figure 6. Such two-dimensional cells were not used in this work, but it is useful as their properties can be generalized to the three-dimensional case, the one that was used for the purposes of this project.

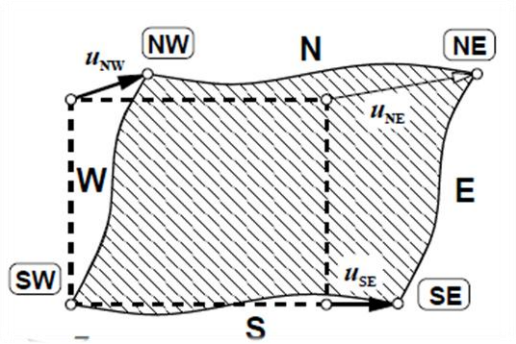

FIGURE 6: SKETCH OF PERIODICITY BOUNDARY CONDITIONS AS USED WITH AN INITIALLY RECTANGULAR TWO-DIMENSIONAL UNIT CELL

For this case, equation (2) leads to the expressions below, where vertex SW is assumed to be fixed. Z_1 and Z_2 are the local coordinates of the master nodes.

$$U_N(Z_1) = U_S(Z_1) + U_{NW} \tag{4}$$

$$U_E(Z_2) = U_w(Z_2) + U_{SE} \tag{5}$$

Equations (4) and (5) directly imply that:

$$U_{NE} = U_{NW} + U_{SE} \tag{6}$$

For numerical analysis the two faces making up a homologous pair of surfaces must be discretized in a compatible way, i.e., the nodal points on them must be positioned at equal values of the face coordinates z_k. Equations (4) and (5) then become sets of linear constraints, each of which links three nodal displacements. The displacements of the “master nodes” SE and NW contain the information on the macroscopic strain tensor. The displacements of the master nodes and of faces S and W fully control the displacements of the slave faces N and E.

In the case of the three-dimensional cubic cell, the SWB node would be fixed, and nodes NWB, SEB and SWT would be the master nodes. Therefore, face T follows

the movement of face B in directions 1 and 2, face E follows the movement of face W in directions 2 and 3, and face N follows the movement of face S in directions 1 and 3.

2.1.5 APPLICATION OF LOADS: METHOD OF MACROSCOPIC DEGREES OF FREEDOM

The periodic volume elements must be subjected to appropriate loads in the form of macroscopic uniform stresses, strains and/or homogeneous temperature changes. Loading by uniform temperatures does not pose much of a difficulty for typical FE codes, whereas applying stresses and strains is not necessarily straightforward. This is the reason why the method of macroscopic degrees of freedom was used to apply stresses and strains to the unit cells in this thesis.

By using the method of macroscopic degrees of freedom, far field stresses and strains can be applied to the unit cell via concentrated nodal forces or prescribed displacements at the master nodes. In this case, nodal forces were applied to the master nodes, which can be evaluated via the divergence theorem [20].

For the configuration of Figure 6, the concentrated forces acting on the master nodes acting on the master nodes SE and NW can be shown to be given by the surface integrals

$$F_{SE} = \int_{Surface\ E} T^a(Z) dS_E \tag{7}$$

$$F_{NW} = \int_{Surface\ N} T^a(Z) dS_N \tag{8}$$

The vector T^a is given by the expression:

$$T^a(Z) = \sigma^a * N_{surface}(Z) \tag{9}$$

It stands for the homogeneous surface traction vector corresponding to the applied macroscopic stress field σ^a at some given point Z on the cell's surface and $N_{Surface}$ is the local normal vector of the appropriate face. For square or rectangular unit cells, equations (7) and (8) simplify to the expressions (in terms of components):

$$f_{SE,1} = \sigma_{11} * S_E \tag{7.1}$$

$$f_{SE,2} = \sigma_{12} * S_E \tag{7.2}$$

$$f_{NW,1} = \sigma_{12} * S_N \tag{8.1}$$

$$f_{NW,2} = \sigma_{22} * S_N \tag{8.2}$$

Equations (7) and (8) can be generalized to require that each master node is loaded by a force corresponding to the surface integral of the surface traction vectors

over the face slaved to it via an equivalent of equations. Analogous procedures hold for three-dimensional cases [4].

2.2 STRUCTURE OF THE TRANSVERSELY ISOTROPIC ELASTICITY TENSOR AND LOAD CASES REQUIRED FOR EVALUATION OF RESULTS

In general, the overall stress tensor within a unit cell can be evaluated by volume averaging or by using the concentrated or reaction forces acting on the master nodes.

$$\langle\sigma\rangle = \frac{1}{\Omega_{UC}} \int_{\Omega UC} \sigma(Z) d\Omega = \frac{1}{\Omega_{UC}} \int_{Surface\ UC} \boldsymbol{T}\ x\ \boldsymbol{Z}\ dSurface \tag{10}$$

Here Ω_{UC} stands for the volume of the unit cell.

In Voigt or Nye notation the elasticity tensor of a transversally isotropic elastic material has the structure

$$\begin{pmatrix} E_{11} & E_{12} & E_{13} & 0 & 0 & 0 \\ E_{12} & E_{11} & E_{13} & 0 & 0 & 0 \\ E_{13} & E_{13} & E_{33} & 0 & 0 & 0 \\ 0 & 0 & 0 & E_{44} & 0 & 0 \\ 0 & 0 & 0 & 0 & E_{44} & 0 \\ 0 & 0 & 0 & 0 & 0 & E_{66} = 0.5(E_{11} - E_{12}) \end{pmatrix} \tag{11}$$

Here 3 is the axial direction and 1-2 is the transverse plane of isotropy. The vector of coefficients of linear thermal expansion has the structure

$$\propto = (\propto_A \quad \propto_A \quad \propto_T \quad 0 \quad 0 \quad 0) \tag{12}$$

and, accordingly, the coefficient of volumetric thermal expansion takes the form

$$\beta = \alpha_A + 2\alpha_T \tag{13}$$

Five independent elastic moduli are required for describing the elastic material behavior and two independent coefficients of thermal expansion are needed for the thermal expansion response. Appropriate parameters that were used in this project include the axial Young's modulus E_A, the transverse Young's modulus E_T, the axial shear modulus G_A, the transverse shear modulus G_T, the axial and transverse effective Poisson's ratio ν_A and ν_T and the effective transverse bulk modulus K_T.

The transverse "in-plane" properties are related via GT=ET/2(1+ ν T), but there is no linkage between the axial properties for general transversally isotropic materials.

The load cases that were applied to obtain these moduli are:

- Axial loading in 1-direction.

- Axial loading in 2-direction.
- Axial loading in 3-direction.
- Shear loading in 12-direction.
- Shear loading in 13-direction.
- Shear loading in 23-direction.

In addition to the above, to obtain the thermal coefficients, a temperature load case was run in order to obtain the thermal coefficients.

2.3 Evaluation of microfields

The evaluation of the microfields was done using the Finite Element Method. The reason for using this method is its geometrical flexibility. The Finite Element method can deal with all kinds of different geometries and catch small differences between them. The evaluation was done using the commercial FE-code ABAQUS/Standard (Simulia, Dessault Systèmes) program; another reason behind the use of the Finite Element Method is that there is no need to develop any new program to do so, as there is already a range of available software in the market.

2.4 Closest transversely isotropic tensor

Effective elasticity tensors were obtained by ensemble averaging elasticity tensors evaluated from a number of SVEs using the in-house code Avgelt. A further improvement was achieved by finding the closest transversally isotropic tensors to the ensemble averaged results using an algorithm published by Moakher and Norris [24]. This was done by an in-house program, closelt.

2.5 Analytical methods used for comparison

As noted in section 1.3, two different analytical methods were used to compare numerical results with analytical bounds. The first of them is the Hashin-Shtrikman bounding method. It is a two-point bound method that does not recognize the difference between various diameter ratio arrangement cases. Therefore, the results given by these bounds can be compared to all diameter ratio cases studio.

The three-point bounds, on the other hand, are sensitive to different fiber diameters. However, the statistical parameters used in these bounds are available only for the case of identical fibers [26]. Consequently, only comparisons for the 1:1 diameter ratio case can be done with the three-point bounds method in this thesis.

Provided statistical parameters are available, the results given by the three-point bounds are more accurate than the ones given by the Hashin-Shtrikman bounds. This is why, in following sections, numerical results will always be closer to the first ones, as they provide quite tight approximations.

To obtain these analytical bounds, an ILSB's program called compcomp was used. It provides a range of analytical methods to obtain estimates and bounds for different kinds of materials and various cases of reinforcement types. For more information on this program see [11].

2.6 ANALYSIS STEPS

2.6.1 PREPROCESSING

2.6.1.1 GENERATION OF VOLUME ELEMENTS: RSI

First, the generation of the microstructure was carried out. For this purpose, random sequential addition was used as implemented in the in-house code Arigen [7], which is a program for generating periodic or non-periodic random arrangements of inhomogeneities in a square or in a cube-shaped box.

By using random sequential addition, also known as random sequential insertion (RSI), positions for new reinforcements are created by random processes, a candidate inhomogeneity being accepted if it does not collide with any of the existing ones and rejected otherwise. [4]

Apart from RSI, Segurado's Monte-Carlo based algorithm [25] and a method using vectorial shifting compression were used to achieve higher fiber volume fractions. These methods must be employed due to the fact that reinforcement volume fractions that can be reached by RSA methods tend to be moderate due to jamming or "geometrical frustration".

As an example, three random geometries that were created with Arigen are shown in Figure 7. They all pertain to a fiber volume fraction of 0.45 and a 0.25 fiber diameter ratio. All of them have 80 fibers and are periodic, but the geometrical arrangement of each of them is different thanks to the random sequential insertion algorithm.

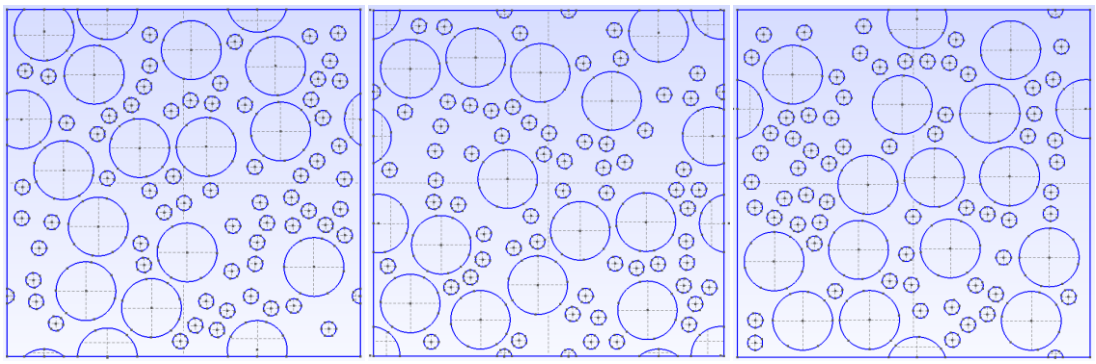

FIGURE 7: THREE DIFFERENT BUT EQUIVALENT REALISATIONS OF FIBER ARRANGEMENT FOR DIAMETER RATIO 0.25 AND 0.45 VOLUME FRACTION

The program Arigen offers different capabilities for creating geometry arrangements. For this thesis, it was asked to create geometries of 80 fibers and diameter ratios of 1, 0.5, 0.3 and 0.25, respectively. The program was required to create fibers of circular cross section ranging in volume fraction from 0.3 to 0.65 for each of the cases stated above. Arigen also offers the possibility to set different minimum distances between inhomogeneities, which are necessary for avoiding a number of difficulties in meshing. These values must be changed and made smaller as the target volume fractions increase, as the conditions to create the same number of fibers but at a higher volume fraction become more and more challenging.

A further visual example of the capabilities offered by Arigen is shown in Figure 8. Two very different geometry arrangements are shown. The one on the left side shows an arrangement of 80 fibers with a diameter ratio of 0.25 and a volume fraction of 0.65, whereas on the right side an example of 80 identical fibers with a fiber volume fraction of 0.45 is presented.

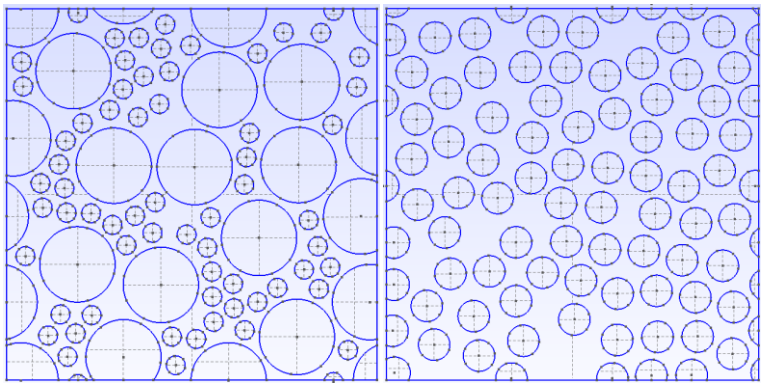

FIGURE 8: DIFFERENT GEOMETRIES CREATED BY ARIGEN

2.6.1.2 MESHING

After the geometries were created, a second step was carried out, the meshing phase. For this purpose, three different programs were used.

The first of them, called convl2g, is an ILSB in-house program that converts the .lst file written by Arigen into an input geometry file readable by gmsh, the program used to do the actual meshing task. In order to achieve this goal, the inputs stated below must be provided to convl2g:

- The type of geometry to be set up: between all available options, the following basic periodic geometries were chosen:
    - Composite geometry, for non-porous composite tests, allows gmsh to mesh inhomogeneities.
    - Pore geometry, for porous material tests, makes gmsh mesh just the matrix area of the geometry.
- Mesh seed: it sets the refinement level of the mesh gmsh will produce. In most cases, coarser meshes will produce a smaller number of elements and consequently a smaller computational time, at the expense of reducing the accuracy of results. A study was carried out to analyze the most suitable mesh seed. Seeds in the range 0.005-0.045 were studied, giving the results shown in table 1 (for 50 fibers of equal diameter):

Mesh Seed	Number of elements	Wall clock time (SEC)	Nel/Time
0,005	109192	286	381,79021
0,01	32850	76	432,236842
0,015	21526	46	467,956522
0,02	26158	60	435,966667
0,025	37066	89	416,47191
0,03	48400	113	428,318584
0,035	63918	163	392,134969
0,04	67172	164	409,585366

TABLE 1: ELEMENT NUMBER, TIME AND NEL/TIME RELATIONSHIP ACCORDING TO MESH SEED

The mesh seed that produces the highest relationship between the produced element number and the required computational time could obviously be one of the best choices, but it must also be taken into account that the 0.015 mesh seed provides the lowest element count, which could lead to some inaccuracy of the results.

It must also be noted that the computational time for the ABAQUS analysis for this 50 fiber case is not so high in any of the cases. As the number of inhomogeneities rises, so does the computational time.

Taking all this data into account a mesh seed of 0.01 was set, as it provides one of the best element number/time relationships offering a higher number of elements that the 0.015 case.

The reason why the 0.02 mesh seed wasn't chosen is that the mesh sizes are more irregular in different areas of the microgeometry, which could give rise to some problems during the gmsh file writing process or at further steps of the testing process.

Figures 9 and 10 show the difference between the 0.01 and the 0.02 mesh seeds for volume elements containing 50 fibers at a volume fraction of 0.35:

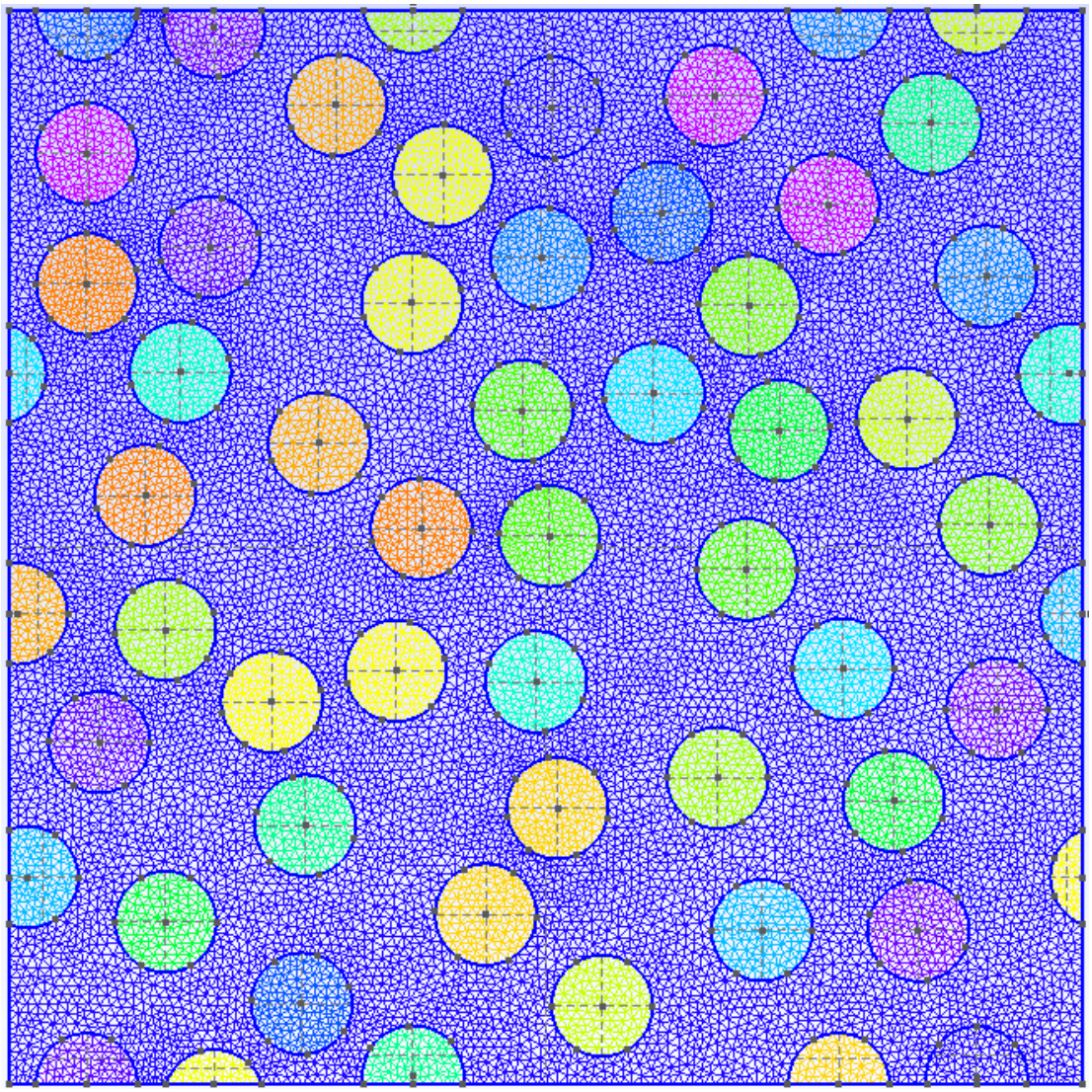

FIGURE 9: MESH OBTAINED WITH THE 0.01 SEED VF AND DR 1

In Figure 9, the mesh size is more or less the same in all areas of the microgeometry, regardless of whether there is an inhomogeneity close of not. There are sufficient numbers of elements between inhomogeneities

In Figure 10, which shows the mesh obtained with the 0.02 seed, it can be noticed that the mesh is coarser in some areas and finer in other areas. The global element number is a little lower than in the 0.01 seed case.

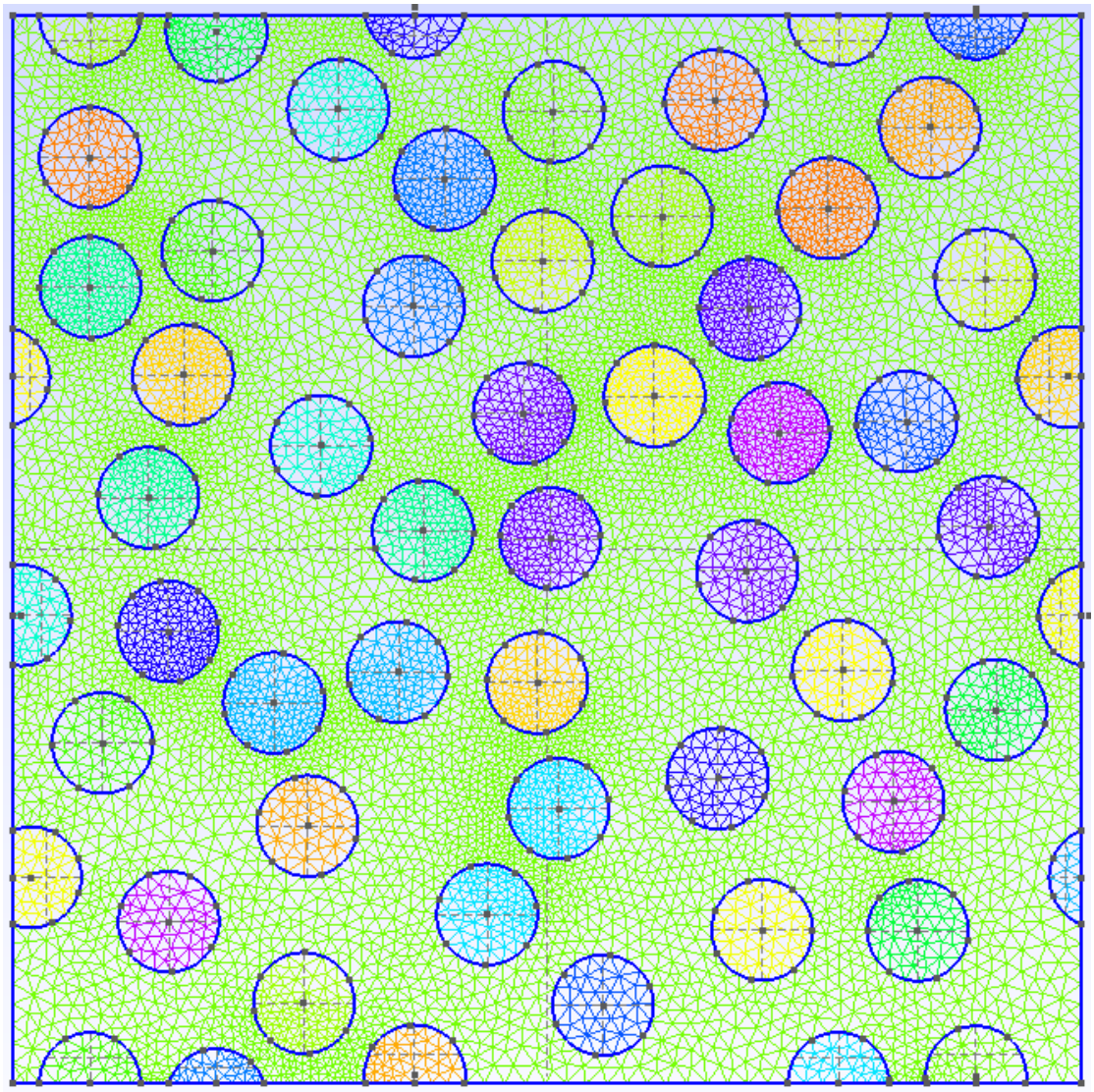

FIGURE 10: MESH OBTAINED WITH THE 0.01 SEED (IDENTICAL FIBERS, VOLUME FRACTION 0.45)

Figures 11 to 13 show the relationships between mesh seed and number of elements, analysis-time of the solver and the quotient between number of elements and analysis time, respectively.

As mentioned before, the actual meshing was carried out with the program gmsh, which is a 2D and 3D finite element mesh generator with a built-in CAD engine and post-processor. It provides a fast, light and user friendly meshing tool with parametric input. It also offers advanced visualization capabilities. The input for all modules of gmsh can be entered either vie the graphical interface or by using ASCII text files. These files must be written in gmsh's own scripting language [8].

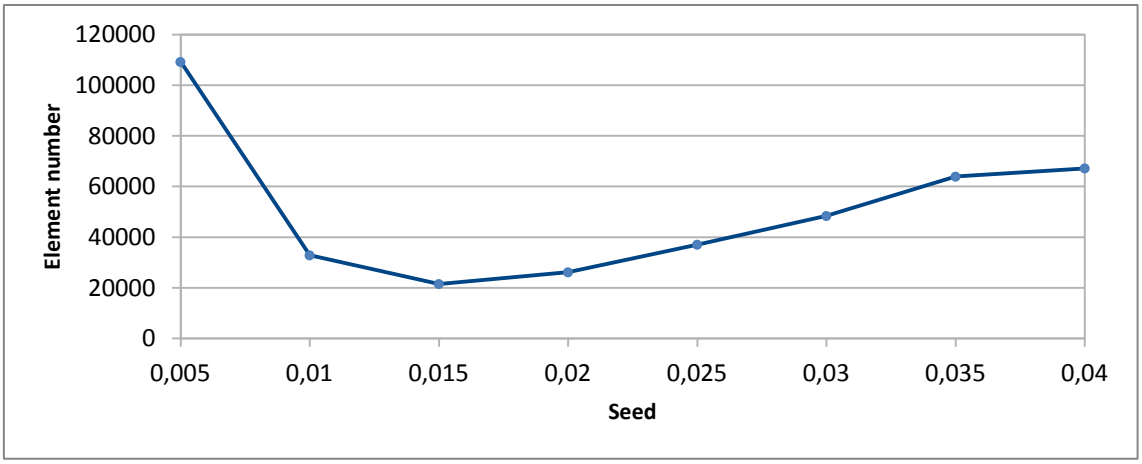

FIGURE 11: NUMBER OF ELEMENTS AS A FUNCTION OF THE MESH SEED

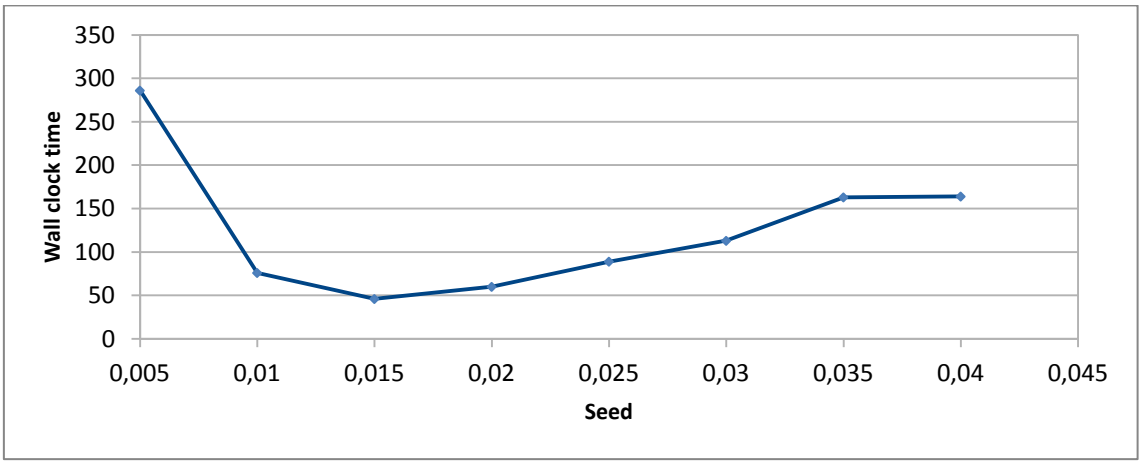

FIGURE 12: COMPUTATIONAL TIME AS FUNCTION OF THE MESH SEED

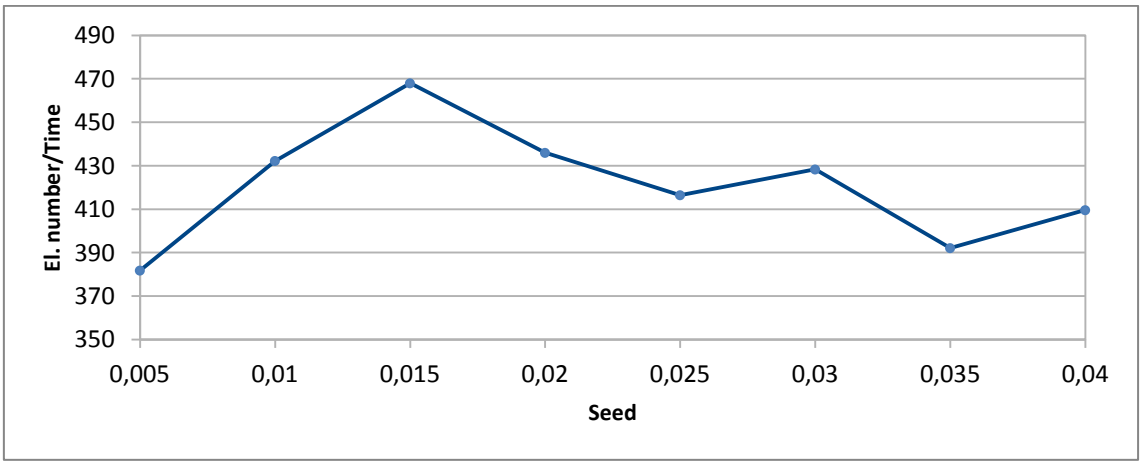

FIGURE 13: ELEMENT NUMBER/TIME RATIO AS A FUNCTION OF THE MESH SEED

For the purpose of this project the geometry was written by convl2g and entered directly into the mesh module. Gmsh then plotted the geometry automatically. Second order triangular elements were used for meshing. On the one hand, second order elements were preferred to first order ones due to their better convergence properties.

On the other hand, triangular elements were used because they are better suited to mesh the kind of geometries used in the project than are quadrilateral elements.

With respect to meshing, it must also be said that fine meshes were created from the beginning, as the effects to be studied in this project are small local second order effects. Because very fine meshes were used in all cases, a mesh scaling analysis was not carried out.

After setting the second order mesh, the new geometry with the mesh data was saved in .inp files, which are readable by ABAQUS.

Up to this point, all that had been created were second order meshed planar geometries. As, to be able to obtain the full elasticity tensor, three-dimensional geometries are needed, the two-dimensional meshed geometry obtained with gmsh is further processed by an in-house program called aba2d3d, which offers the following options:

- Number of layers to be used: these refer the number of identical layers the user wishes to generate in the normal direction. For the purpose of this project just one layer was used for each sample.
- Layers' thickness: a thickness of 0.02 units was used in all samples. This thickness is trivial, as the only purpose of giving the model a length in the normal direction is to obtain three-dimensional models for extracting the three-dimensional elasticity tensor.

Program aba2d3d then extrudes the two-dimensional mesh to obtain a three-dimensional geometry, quadratic wedge elements with 15 nodes each being generated from the quadratic triangles. This mesh data is written to an .inp file that is compatible with ABAQUS.

2.6.1.3 Generation of periodicity boundary conditions

Next, periodicity boundary conditions were created, following equations (2) to (6) given in section 2.1. For this aim, the ILSB in-house program MedTool [10] was used.

MedTool enables the creation of cubic periodic boundary conditions when supplied with the three-dimensional meshed geometry obtained with Aba2d3d. It reads the nodal data from the input file and generates node sets and constraint equations based on the geometrical data. The output file containing the equations is written in

ABAQUS syntax. In addition, another file defining six or (when the thermal case is also considered, seven) independent load cases is provided [10].

FIGURE 14: NODE SETS GENERATED BY MEDTOOL WITH THEIR CORRESPONDING NOTATION [10]

2.6.2 SOLVING: FIELD EVALUATION

When the mesh was set, the stress and strain values in the microfields were computed. For this purpose, simulations were run using the Finite Element method, through the ABAQUS analyzer.

ABAQUS is a suite of software for finite element analysis that is known for its high performance, quality and ability to solve all kinds of simulations. If offers powerful and complete solutions that can be applied to a vast spectrum of industrial applications [12].

For carrying out field evaluation, ABAQUS Analysis was used. It has served to analyze ABAQUS input files and obtain output files that hold information related to the stress and strain microfields, as well as information about the displacements and engineering moduli. The input file entered for analysis purposes has the following structure:

- Node and element definitions: these are included through a calling to the geometry file obtained from Aba2d3d.
- Material data: matrix and fiber material data is entered. The Young's modulus and the Poisson number are specified here for an isotropic material.
- Boundary conditions:
    - Periodic boundary conditions are entered through a calling to the boundary condition file output from Medtool.

- Displacement boundary conditions are inserted to the master nodes SWB, SEB and NWB, following the indications shown on the Figure below:

```
*BOUNDARY, TYPE=DISPLACEMENT
SWB, 1, 3, 0
SEB, 3, 3, 0
NWB, 3, 3, 0
NWB, 1, 1, 0
```

FIGURE 15: DISPLACEMENT BOUNDARY CONDITIONS

According to these equations,

  - Node SWB has its movement restricted in all three directions (from direction 1 to direction 3: 1, 2 and 3).
  - Node SEB has its movement restricted in Z axis.
  - Node NWB has its movement restricted in X and Z axis (1 and 3; from 1 to 1 and from 3 to 3).

- Insertion of 7 independent load cases. The first 6 of them correspond to elastic load cases and are required to obtain the full elastic tensor, while the last of them is a temperature load case that is used to compute the coefficient of thermal expansion (CTE). The load cases are listed below:
  - Axial load in X direction.
  - Axial load in Y direction.
  - Axial load in Z direction.
  - Shear load in XY direction.
  - Shear load in XZ direction.
  - Shear load in YZ direction.
  - Temperature load case.

The mechanical load cases are solved in a “perturbation step”. The Finite Element Method discretizes the Navier-Cauchy equations of linear elasticity into an algebraic system of equations of the type:

$$(K)(U) = (F) \tag{14}$$

Where (K) is the global stiffness matrix, which in the present case is identical for all mechanical load cases. (F) is the force vector, which is different for each mechanical load case, and (U) is the vector of unknown displacements, which must be solved for.

In order to save computational costs and make the computation of the displacements easier, $(K)^{-1}$ is factorized first. Formally this may be represented by the expression:

$$(U) = (K^{-1})(F) \tag{15}$$

which is equivalent to equation (14). In practice the actual evaluation of the inverse of the stiffness matrix is typically avoided, being inefficient. On this basis of equation (15) it is, however, easy to understand that displacement vectors (U) pertaining to the six mechanical force vectors (F) can be obtained by just carrying out back substitution step, provided the problem is formulated such that (K) is not modified in the process. Doing the factorization of the stiffness matrix (K) only once obviously allows considerable savings in computational effort and analysis time. In the case of the thermal expansion load, the global stiffness matrix must be reformulated and factorized once more.

It is worth keeping in mind that, as mentioned in section 2.6.1.2, quadratic finite elements were used. This way, use can be made of the flexibility of the second-order isoparametric wedge elements for closely approximating the shape of the fibers, viz., circular cylinders, illustrated for the case of the tetrahedral elements in Figure 16. In addition, the second order shape functions provide increased accuracy in representing curved deformed shapes, as is indicated in Figure 16, again for the example of tetrahedral elements [2.1].

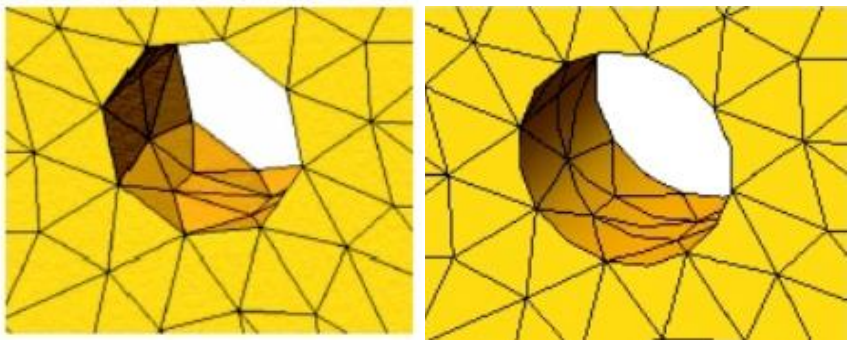

FIGURE 16: APPROXIMATING CURVED GEOMETRIES: FIRST VS SECOND ORDER TETRAHEDRAL MESHING

As can be seen in the example above, the first order elements cause imprecise element mapping to the whole, while second order ones, due to their extended deformation properties, map precisely to curvilinear geometry. This property is very important for the present work, as fibers of circular cross section approach each other closely in the vast majority of analyzed configurations.

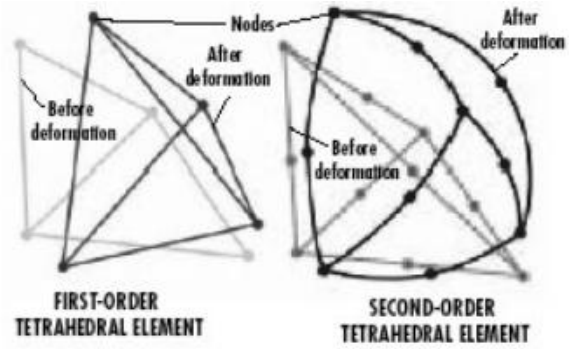

FIGURE 17: FIRST ORDER VS SECOND ORDER TETRAHEDRAL ELEMENTS

The output file generated by ABAQUS/Standard is an .odb file that can be read by the ABAQUS/Viewer module for graphical post-processing, as well as by other post-processing programs, e.g., MedTool, for extracting data on the computed stress and strain fields.

2.6.3 POST- PROCESSING

After solving the micromechanical responses the post processing phase was entered. The ultimate aim of this stage is to extract effective moduli from the microfield data. To obtain representative results, nine tests of different but statistically equivalent geometry arrangements were carried out for each combination of volume fraction and diameter ratio, allowing ensemble averaging over the data obtained from the individual SVEs. These results have proved to be of good quality, as the standard deviations of the components of the elastic tensors obtained this way do not exceed, for the vast majority of cases, a level of 1% of the corresponding ensemble averages.

After obtaining the ensemble averaged results, this data was used to find the closest transversely isotropic tensor, from which the effective moduli were extracted.

The post-processing phase can be divided into two different sub-stages; different tools were used at each of them for carrying out various tasks.

2.6.3.1 EXTRACTION OF FORCES AND DISPLACEMENTS

MedTool also offers post-processing facilities, as it is able to read ABAQUS .odb files. A module called ABAQUS Fu-Reader included in MedTool was used for post-processing. It reads ABAQUS .odb files and extracts the master nodes's displacement and concentrated nodal force data evaluated by the ABAQUS run. It generates special formatted text files [10], and example of which is listed in Figure 18.

```
XYZ; SWB;    [  0  0  0 ]
XYZ; SEB;    [  4  0  0 ]
XYZ; NWB;    [  0  4  0 ]
XYZ; SWT;    [  0  0  4 ]
XYZ; SET;    [  4  0  4 ]
XYZ; NWT;    [  0  4  4 ]
U  ; SEB:Step-1;    [ 3.0494E-03 1.8416E-13 0.0000E+00 ]
RF ; SEB:Step-1;    [ 1.0000E+00 -2.4258E-13 -6.3974E-12 ]
CF ; SEB:Step-1;    [ 0.  0.  0. ]
U  ; SWB:Step-1;    [ 0.0000E+00 0.0000E+00 0.0000E+00 ]
RF ; SWB:Step-1;    [ -1.0000E+00 -1.3215E-10 -1.3231E-12 ]
CF ; SWB:Step-1;    [ 0.  0.  0. ]
...
```

FIGURE 18: EXAMPLE OF TEXT FILE OBTAINED GENERATED BY THE FU-READER [10]

2.6.3.2 COMPUTATION OF ELASTIC MODULI

Another tool included in MedTool, called Fu-Analyzer, reads the master node data from the output of Fu-Reader and evaluates the homogenized elasticity and compliance tensors from them. In addition, it computes the corresponding effective elastic moduli, both being output to a text file [10]. Figure 19 shows an example of such an output file.

```
...
Homogenized   STRESSES
=============================================================================
Step     S_11          S_22          S_33          S_23          S_13          S_12
-----------------------------------------------------------------------------
1 +6.2500e-02  +8.2762e-12  +5.5626e-13  -3.7789e-14  -1.8989e-13  +2.1679e-13
2 -4.4892e-11  +6.2500e-02  -9.2731e-14  +1.9083e-14  +2.9090e-13  -3.5781e-13
3 -5.3601e-12  -1.3094e-13  +6.2500e-02  +3.3074e-15  +1.4393e-14  -1.6485e-14
4 +2.6060e-13  -4.4247e-14  -5.9446e-14  +9.2503e-14  +3.1941e-13  +6.2500e-02
5 -5.9818e-15  -3.2178e-15  +5.8056e-15  -6.2176e-15  +6.2500e-02  +3.8441e-14
6 +4.3263e-14  +1.5912e-14  +2.0401e-14  +6.2500e-02  +1.7858e-14  -3.1143e-14

ENGINEERING Constants
=============================================================================
  E_1 =       81.983     | G_23 =       16.268     | nu_23 =   -0.0046721
  E_2 =       34.261     | G_13 =       45.377     | nu_13 =    0.085774
  E_3 =       552.55     | G_12 =       7.8169     | nu_12 =     0.72004
```

FIGURE 19: EXAMPLE OF TEXT FILE GENERATED BY FU-ANALYZER [10]

After this step, the elastic modulus' data is known for each of the nine tests that were run for each volume fraction and diameter ratio.

2.6.3.3 ENSEMBLE AVERAGING

As said above, nine tests were carried out for each volume fraction and diameter ratio. This number of tests has proven to be sufficient for closely approaching statistically representative volume elements, as the standard deviations obtained from the averaged results are less than 1% of the corresponding averages for the majority of cases, as shown in Figure 21. The program used to obtain these ensemble averaged results is called Avgelt; it is an ILSB in-house code.

The files used by Avgelt for creating the ensemble averaged elastic tensors are the files output by FuAnalyzer, each of which contains the elastic tensor of its test, respectively. As an example, the averaged elastic tensor resulting from the 9 tests

carried out for composites reinforced by identical fibers of volume fraction 0.4 as output by Avgelt in the form:

```
*STIFFNESS Matrix        (averaged, symmetrized)
11 22 33 23 13 12       ** stress/strain component ordering
2                       ** symmetrization factor (2..engineering)
*****************************************************************************
  4.31447E+11  1.95604E+11  1.68430E+11  6.32716E-04 -1.16064E-03  2.38120E+08
  1.95604E+11  4.28157E+11  1.67788E+11 -4.33503E-03 -1.25237E-03  4.26520E+08
  1.68430E+11  1.67788E+11  3.08780E+12 -1.62839E-04  2.23690E-05  1.29524E+08
  6.32716E-04 -4.33503E-03 -1.62839E-04  1.25667E+11  2.18650E+08 -2.79097E-03
 -1.16064E-03 -1.25237E-03  2.23690E-05  2.18650E+08  1.26863E+11 -1.85327E-03
  2.38120E+08  4.26520E+08  1.29524E+08 -2.79097E-03 -1.85327E-03  1.18625E+11
```

FIGURE 20: AVGELT OUTPUT FOR THE ELASTICITY TENSOR GENERATED FROM THE RESULTS PERTAINING TO A CONTINUOUSLY REINFORCED COMPOSITE OF VOLUME FRACTION 0.4

Even though it is symmetric, this elastic tensor is not transversely isotropic, as there are numerical terms that are not zero on the top right side and on the bottom left side. To achieve a transversely isotropic tensor, all these terms should be 0. Apart from this, in a purely transversely isotropic tensor, the pairs of elements corresponding to the transverse directions, i.e. E11 and E22, E12 and E21, should have exactly the same values, and the condition for E_{66} given in equation (11) should be met.

From the tensors given in Figure 20, each modulus can be obtained from relations between the matrix elements of transversally isotropic elasticity tensors, as shown in the equations (16) to (21).

$$E_A = E_{33} - \frac{2E_{13}^2}{E_{11}+E_{12}} \tag{16}$$

$$E_T = E_{11} - \frac{E_{33}E_{12}^2+E_{11}E_{13}^2-2E_{13}E_{12}^2}{E_{33}E_{11}-E_{13}^2} \tag{17}$$

$$\nu_A = \frac{E_{13}}{E_{11}+E_{12}} \tag{18}$$

$$\nu_T = \frac{E_{33}E_{12}-E_{13}^2}{E_{33}E_{11}+E_{13}^2} \tag{19}$$

$$G_A = E_{44} \tag{20}$$

$$G_T = E_{66} \tag{21}$$

$$K_T = 0.5(E_{11} + 2E_{12}) \tag{22}$$

$$K = \frac{1}{9}(E_{33} + 2E_{11} + 4E_{13} + 2E_{12}) \tag{23}$$

In the outputs of both Medtool and Avgelt the 3 direction corresponds to the axial direction, while 1 and 2 directions are the transverse directions.

The standard deviations of the components of the elastic tensor listed in Figure 20, i.e., for the composite reinforced by aligned, identical fibers of volume fraction 0.4 are shown in Figure 21.

```
*STIFFNESS Matrix        (standard deviations, symmetrized)
11 22 33 23 13 12       ** stress/strain component ordering
2                       ** symmetrization factor (2..engineering)
*****************************************************************************
  2.07018E+09  1.40488E+09  1.98443E+08  3.22014E-03  5.00097E-03  1.26664E+09
  1.40488E+09  2.26755E+09  3.32679E+08  3.91986E-03  2.40493E-03  1.18327E+09
  1.98443E+08  3.32679E+08  5.52659E+07  4.76980E-04  4.92551E-04  3.04582E+08
  3.22014E-03  3.91986E-03  4.76980E-04  6.56534E+08  6.31311E+08  3.38538E-03
  5.00097E-03  2.40493E-03  4.92551E-04  6.31311E+08  4.20278E+08  3.07478E-03
  1.26664E+09  1.18327E+09  3.04582E+08  3.38538E-03  3.07478E-03  1.45976E+09
```

FIGURE 21: AVGELT OUTPUT FOR THE STANDARD DEVIATIONS PERTAINING TO THE ENSEMBLE AVERAGED ELASTIC TENSOR LISTED IN FIGURE 20

As mentioned above, the standard deviations pertaining to the tensor elements that must be nonzero for transverse isotropy are less than 1% of the corresponding ensemble averages in most cases. The standard deviations of the other components are of comparable or smaller magnitude. Equation (24) lists this data set in a format that is easier to read and equation (25) presents the standard deviations of the "active components" of the elasticity tensor as percentages with respect to the corresponding ensemble averages. The other tensor components, for which normalization does not make sense, are marked by asterisks.

$$\begin{pmatrix} 431.4 \pm 2.07 & 195.6 \pm 1.40 & 168.4 \pm 0.20 & 0 & 0 & 0 \pm 1.27 \\ 195.6 \pm 1.40 & 428.2 \pm 2.27 & 167.8 \pm 0.33 & 0 & 0 & 0 \pm 1.18 \\ 168.4 \pm 0.20 & 167.8 \pm 0.33 & 3087.8 \pm 0.05 & 0 & 0 & 0 \pm 0.30 \\ 0 & 0 & 0 & 125.7 \pm 0.66 & 0 \pm 0.63 & 0 \\ 0 & 0 & 0 & 0 \pm 0.63 & 126.9 \pm 0.42 & 0 \\ 0 \pm 1.27 & 0 \pm 1.18 & 0 \pm 0.30 & 0 & 0 & 118.6 \pm 1.46 \end{pmatrix} \quad (24)$$

$$\begin{pmatrix} 0.48\% & 0.72\% & 0.12\% & 0 & 0 & 0 \\ 0.72\% & 0.53\% & 0.2\% & 0 & 0 & 0 \\ 0.12\% & 0.2\% & 0\% & 0 & 0 & 0 \\ 0 & 0 & 0 & 0.52\% & 0 & 0 \\ 0 & 0 & 0 & 0 & 0.3\% & 0 \\ 0 & 0 & 0 & 0 & 0 & 1.23\% \end{pmatrix} \quad (25)$$

2.6.3.4 FINDING THE CLOSEST TRANSVERSELY ISOTROPIC ELASTICITY TENSOR

To find the closest transversely isotropic elasticity tensors to the ensemble averaged results obtained with Avgelt the in-house program called closelt was

employed. This program finds the closest transversely isotropic elasticity tensor following [24] and computes the corresponding transversely isotropic moduli.

The transversely isotropic tensor was output by closelt for the case analyzed in this section (identical aligned fibers, volume fraction 0.4, compare Figure 21) is shown in Figure 22.

```
#elasticity tensor
  4.30559D+11  1.94842D+11  1.68108D+11  0.00000D+00  0.00000D+00  0.00000D+00
  1.94842D+11  4.30559D+11  1.68108D+11  0.00000D+00  0.00000D+00  0.00000D+00
  1.68108D+11  1.68108D+11  3.08780D+12  0.00000D+00  0.00000D+00  0.00000D+00
  0.00000D+00  0.00000D+00  0.00000D+00  1.26263D+11  0.00000D+00  0.00000D+00
  0.00000D+00  0.00000D+00  0.00000D+00  0.00000D+00  1.26263D+11  0.00000D+00
  0.00000D+00  0.00000D+00  0.00000D+00  0.00000D+00  0.00000D+00  1.17859D+11
```

FIGURE 22: CLOSELT OUTPUT FOR THE TRANSVERSELY ISOTROPIC TENSOR TO THE ENSEMBLE AVERAGED ELASTIC TENSOR LISTED IN FIGURE 20

Here, the terms that do not have a relation to the transversely isotropic elastic moduli are zero, demonstrating that this is really a transversely isotropic tensor. On the other hand, the terms that flagged as having to be equal in the previous section can be seen to be equal.

As mentioned before the elastic moduli that are of interest for this work were also computed directly by closelt, the output for the present example being given in Figure 23.

```
#elastic moduli
   EA=2.99742D+12   ET=3.39584D+11   GA=1.26263D+11   GT=1.17859D+11
  nuA=2.68801D-01  nuT=4.40642D-01   KT=3.12701D+11    K=5.56782D+11
```

FIGURE 23: CLOSELT OUTPUT FOR THE TRANSVERSELY ISOTROPIC MODULI PERTAINING TO THE ELASTICITY TENSOR LISTED IN FIGURE 21

2.6.4 COMPARISON WITH ANALYTICAL RESULTS

As mentioned in section 2.5, analytical results were obtained with this the ILSB in-house code `compcomp`. It is a program that provides access to a number of analytical micromechanical models for evaluating the overall elastic, thermoelastic, and conduction properties of two-phase materials and composites from the constituent properties.

In addition, simple strength predictions from some of these models can be obtained and effective elastic and concentration tensors can be output for some of the models. For selecting program modes, micromechanical models etc. the user is offered a list of possible choices. Installations of `compcomp` may come with a Material Data

Library, from which information is taken to generate data based on different analytical models.

The first step that must be taken when working with `comcomp` is selecting the evaluation models. `compcomp` provides micromechanical models for eight classes of two-phase materials, but for the purpose of this project just two of them were used.

- composites containing continuous, unidirectional constituents
- porous materials

Secondly, the customized material data that the user wants to use can be input by hand or by reading a compatible text file. The required material symmetries of the constituents must also be selected among different options. For the present work, isotropic constituent material was used, the elastic behavior being defined via Young's modulus and Poisson's number.

Finally, the analytical model for obtaining the results has to be chosen. If continuous unidirectional constituents were selected at the first step, the user is given the choice to select between twelve available models, all of which give transversally isotropic behavior. From the available database, the three-point bound and the Hashin-Shtrikman bounds were selected, as they provide lower and upper bounds for random fiber arrangements of identical, aligned fibers.

In the case of porous materials, twelve models are also available in `compcomp`, from which, as for the composite, the upper three-point Bounds and Hashin-Shtrikman upper bounds for porous materials model were chosen. These models evaluate the three-point and two-point bounds for materials containing spherical or continuously aligned cylindrical pores, the lower bound being trivial.

It must also be noted that the analytical three-point bounding method only provides results for the equal size fiber diameter case. Therefore, comparisons can't be made for the different fiber diameter ratio cases [11].

3. RESULTS

3.1 GENERAL REMARKS

3.1.1 GEOMETRY

Volume elements of right hexahedral shape were used for modeling. Their side lengths are 1m in the 1- and 2- directions and 0.02m in the 3-direction. It is worth noting that in elastic micromechanical analyses the absolute size of the unit cell does not influence the predicted elastic moduli. Each unit cell contains 80 fibers that either are identical (i.e. have the same diameter) or have two different diameters of ratio 1:2, 1:3 or 1:4. In the case of the non-unity diameter ratios, the bigger fibers take up to 80% of the total fiber volume and the smaller ones 20%.

3.1.2 MATERIAL

Two different inhomogeneous materials were studied. The first of them is a fiber reinforced composite, consisting of a fictitious matrix material and a fictitious fiber material. Both materials are isotropic and are described as follows:

- Matrix material
  - Youngs' modulus: 130 GPa
  - Poisson's coefficient: 0.344
  - Coefficient of thermal expansion: $1.7 \times 10^{-5}\ K^{-1}$
- Fiber material
  - Young's modulus: 6500 GPa
  - Poisson's coefficient: 0.2
  - Coefficient of thermal expansion: $1.7 \times 10^{-6}\ K^{-1}$

The corresponding entries in the ABAQUS' input file are listed in Figure 24:

```
*MATERIAL, NAME=MatrixMat
*ELASTIC, TYPE=isotropic
*****     E,       nu,     TEMP
      130000000000,     0.344,      0.0
*EXPANSION, TYPE=isotropic
1.7E-05
*MATERIAL, NAME=FiberMat
*ELASTIC, TYPE=isotropic
*****     E,       nu,     TEMP
     show,     0.2,      0.0
*EXPANSION, TYPE=iso
1.7E-06
```

FIGURE 24: ABAQUS MATERIAL INPUT SECTION FOR THE THERMOELASTIC PROPOERTIES OF THE CONSTITUENTS OF THE COMPOSITE

The second inhomogeneous material, a matrix containing aligned, cylindrical, continuous pores, has the same matrix as the composite material shown above, i.e.

- Matrix material
  - Young's modulus: 130 GPa
  - Poisson's coefficient: 0.344

The porous material, as its name indicates, doesn't have any fiber material, having just void space instead.

3.1.3 BOUNDARY CONDITIONS

Unit cells together with the boundary conditions (BCs) prescribed on them must generate valid tilings both for the original geometry and for all deformed states pertinent to a given micromechanical problem. Accordingly, gaps and overlaps between neighboring unit cells must not be allowed, as the cells must be geometrically compatible. In order to achieve this, boundary conditions for the unit cells must be specified in such a way that all deformation modes appropriate for the load cases to be studied can be attained [4]. As discussed in section 2.1.4 periodicity boundary conditions were used in the present study.

3.1.4 NUMBER OF SIMULATIONS

Equal numbers of tests were run for both studied inhomogeneous materials, organized as shown in Figure 25:

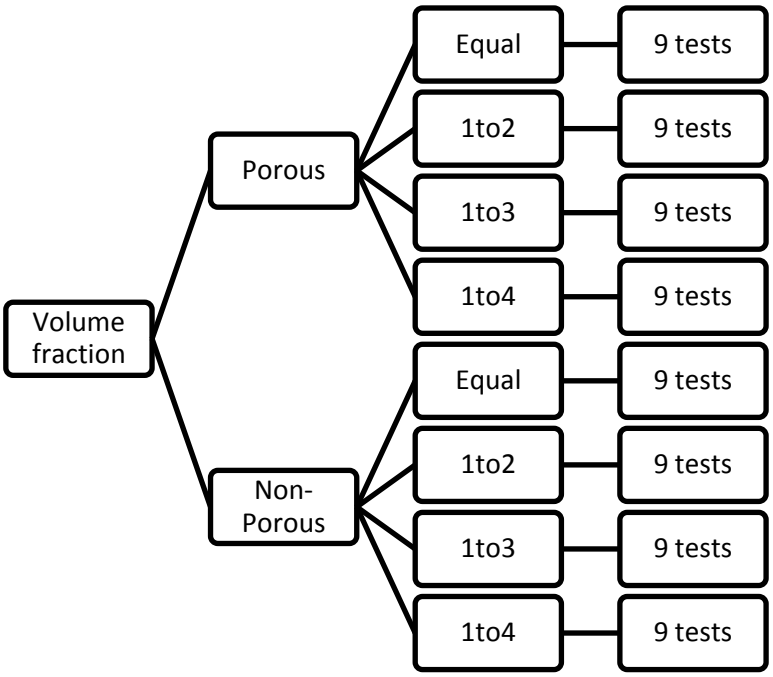

FIGURE 25: HIERARCHY OF MOELING RUNS

After running the 9 tests for each case, the results were averaged using the program `Avgelt` and the closest transversely isotropic tensor was evaluated using the program `closelt`. 9 tests were used for creating statistical models that approach actual representative volume elements in accuracy, at least for most of the cases. This can be seen in the values of the standard deviations related to the averaged elastic tensor in equation (24). In the majority of cases the standard deviations were found to be below 1%, which indicates an acceptable accuracy of the results.

3.1.5 Analytical results

The table 3 lists analytical results obtained with the program `compcomp`. Among the available analytical models, the Hashin-Shtrikman and the three-point bounds were chosen, as they provide values for the upper bounds in the porous case and upper as well as lower bounds in the non-porous case. All numerical data should fall in the range of the Hashin-Shtrikman bounds and results for identical fibers should fulfill the three-point bounds in order to be considered accurate and acceptable.

As can be easily seen, the three-point Bounds are tighter than the Hashin-Shtrikman ones. It most cases, the numerical results fall inside the range of validity defined by these two theories. In the cases where this is not the case, the numerical values typically are extremely close to the appropriate Three-point bounds. The numerical predictions are practically always inside the Hashin-Shtrikman bounds. There are some values that do not follow the analytical bounds, which may be due to insufficient statistics.

3.2 Macroscopic behavior

3.2.1 Composite material

3.2.1.1 Transverse Young's modulus of the composite

The numerical results obtained for the transverse Young's modulus E_T are listed in table 2. All values are given in GPa. Obviously, the stiffness of the composite grows with increasing reinforcement volume fraction. As for the diameter ratio, it must be noted that it is a second order effect. Therefore, the predicted differences in stiffness due to different diameter ratios are much smaller than the effects of reinforcement volume fraction.

The E_T values show different tendencies for different diameter ratios as the volume fraction increases. For lower amounts of reinforcement (fiber volume fractions from 0.3 to 0.5) the stiffness tends to increase very slightly as the diameter ratio

decreases. However, for higher volume fractions, a decrease in the transverse Young's modulus appears as the diameter ratio decreases. The differences in absolute value between the equal diameter case and the 1:4 case tend to grow as the volume fraction increases.

ET		Diameter Ratio			
		Equal	1:2	1:3	1:4
Volume Fraction	0.3	243	244	245	245
	0.35	270	271	272	272
	0.4	303	304	304	306
	0.45	340	342	344	347
	0.5	386	387	387	392
	0.55	450	440	444	446
	0.6	539	518	519	523
	0.65	624	634	621	613

TABLE 2: NUMERICAL RESULTS FOR THE TRANSVERSE YOUNG'S MODULUS OF THE COMPOSITE

Table 3 shows the analytical predictions obtained for the lower and upper Hashin-Shtrikman as well as three-point bounds. All values are given in GPa.

Fiber VF	ET Lower 3PB	ET Upper 3PB	ET Lower HSB	ET Upper HS
0	130	130	130	130
0.05	153	157	153	257
0.1	168	184	168	385
0.15	184	220	183	520
0.2	201	267	199	665
0.25	221	326	217	821
0.3	243	398	238	989
0.35	269	487	261	1170
0.4	300	594	288	1370
0.45	336	722	320	1580
0.5	380	876	357	1820
0.55	433	1060	402	2080
0.6	499	1280	457	2360
0.65	584	1540	527	2680
0.7	694	1860	617	3040

TABLE 3: THREE POINT AND HASHIN-SHTRIKMAN BOUNDS FOR THE TRANSVERSE YOUNG'S MODULUS OF THE COMPOSITE

In Figure 26 both analytical and numerical results (the latter pertaining to identical fibers) for the transverse Young's modulus are plotted as functions of the fiber volume fraction.

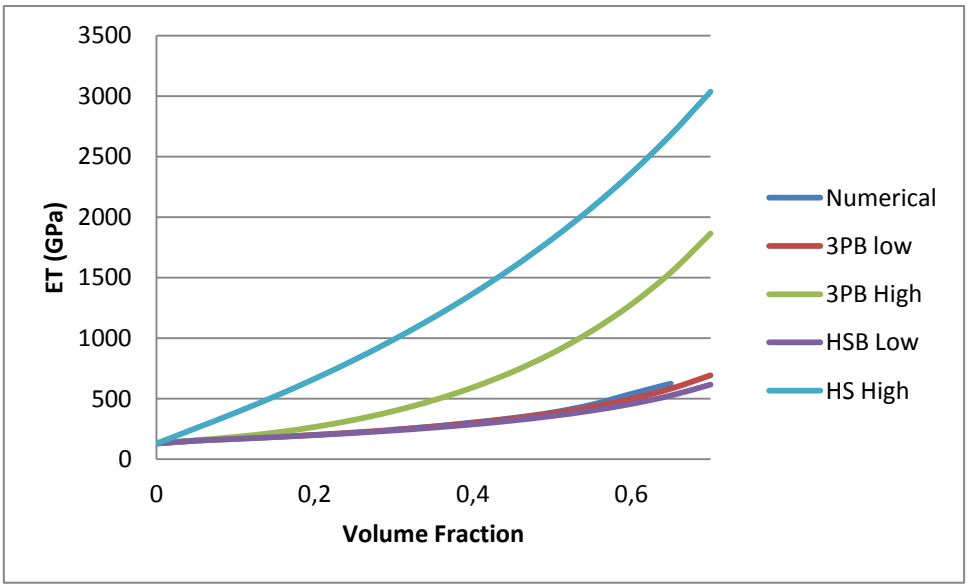

FIGURE 26: NUMERICAL RESULTS AND ANALYTICAL LOWER AND UPPER BOUNDS FOR ET

As the fibers are stiffer than the matrix material, the results follow quite closely the lower three point and Hashin-Strikman bounds. A more detailed view is therefore provided in Figure 27.

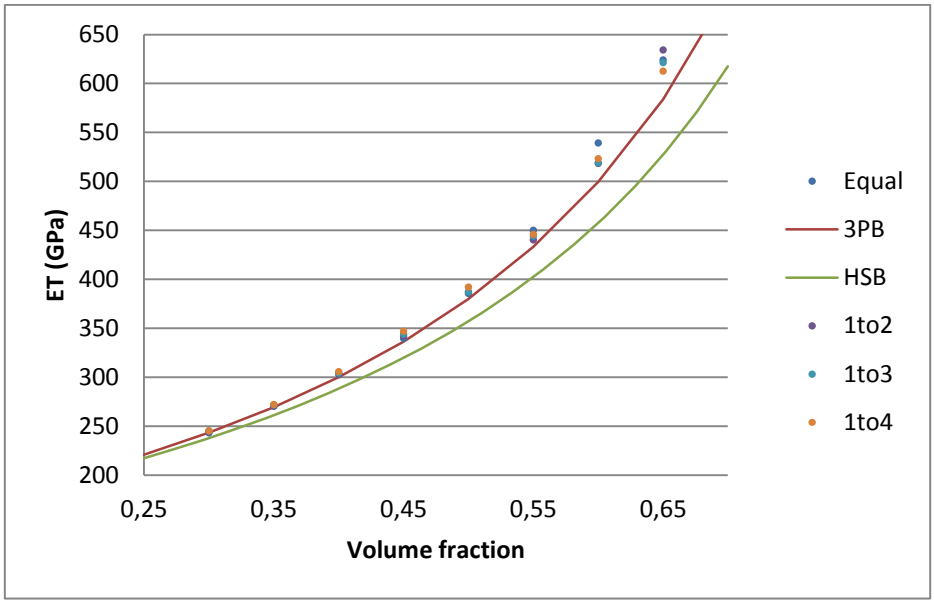

FIGURE 27: NUMERICAL VALUES FOR ET IN COMPARISON WITH LOWER BOUNDS

This graph shows the evolution of the transverse Young's modulus for different volume fractions. For each volume fraction tests with diameter ratios of 1, 0.5, 0.33 and 0.25 were done, respectively. Comparisons with the three-point bounds can only be made for samples with diameter ratio 1, as models only provide information for cylindrical fibers of equal diameter ratio. For all data studied the numerical results are above the Hashin-Shtrikman bounds.

Figures 28 to 30 show detailed data regarding the fiber volume fractions 0.35, 0.5 and 0.65 respectively. Results show that the differences in diameter ratio have a stronger influence in the transverse Young's modulus as the volume fraction increases. For the volume fraction of 0.35 results fall within an interval of 2 GPa (0.7% of the value of the transverse Young's modulus), whereas for the volume fraction of 0.65 the interval is approximately 22 GPa (3% of the transverseYoung's modulus). As the target for the standard deviation is 1% of the value of the moduli, the results obtained for the predictions between 0.5 and 0.65 volume fractions are statistically significant.

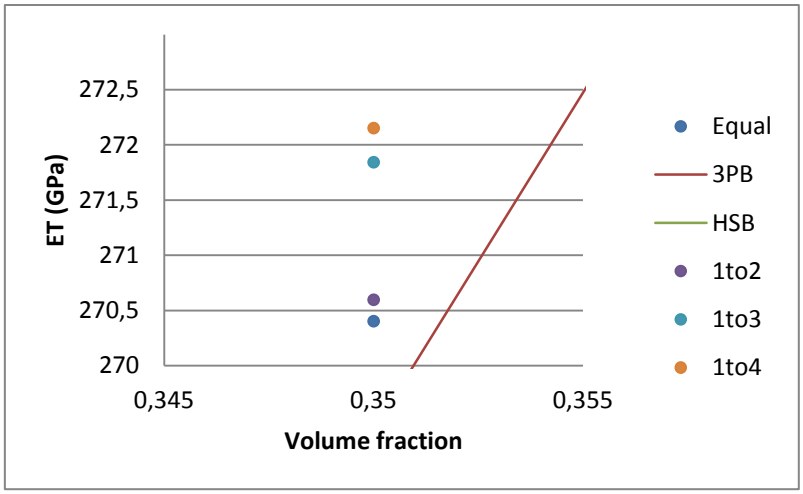

FIGURE 28: DETAIL FOR THE TRANSVERSE YOUNG'S MODULUS AT FIBER VOLUME FRACTION 0.35

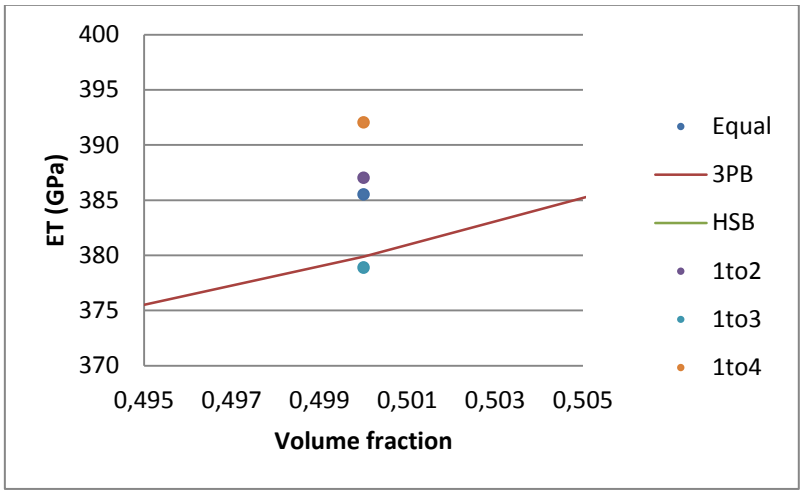

FIGURE 29: DETAIL FOR THE TRANSVERSE YOUNG'S MODULUS AT FIBER VOLUME FRACTION 0.5

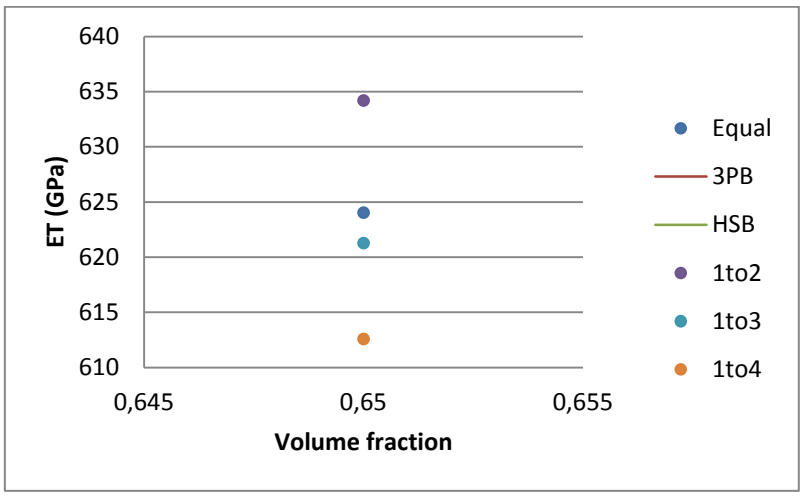

FIGURE 30: DETAIL FOR THE TRANSVERSE YOUNG'S MODULUS AT FIBER VOLUME FRACTION 0.65

3.2.1.2 AXIAL YOUNG'S MODULUS

Table 4 lists numerical predictions for the axial Young's modulus in units of GPa. As was to be expected, this modulus shows no dependence on the diameter ratio of the fibers. The analytical bounds are essentially identical to the numerical estimates and are not shown here.

EA		Diameter Ratio			
		Equal	1:2	1:3	1:4
Volume Fraction	0.3	2040	2040	2040	2040
	0.35	2360	2360	2360	2360
	0.4	2680	2680	2680	2680
	0.45	2990	2990	2990	2990
	0.5	3320	3320	3320	3320
	0.55	3630	3630	3630	3630
	0.6	3950	3950	3950	3950
	0.65	4270	4270	4270	4270

TABLE 4: NUMERICAL RESULTS FOR THE AXIAL YOUNG'S MODULUS OF THE COMPOSITE

3.2.1.3 TRANSVERSE SHEAR MODULUS OF THE COMPOSITE

The results for the transverse shear modulus G_T are given in GPa as well, see table 5. As for the transverse Young's modulus, the results show two opposite tendencies in the dependence on the diameter ratio for different fiber volume fractions. The transverse shear modulus' value increases with decreasing diameter ratio for volume fractions up to 0.5 (inclusive). For higher volume fractions, the tendency is reversed. It may be noted that the central volume fractions e.g. 0.45, 0.5 and 0.55, tend to give the lowest absolute differences between the equal diameter reinforcements and the case with the 1to4 diameter ratio.

GT		Diameter Ratio			
		Equal	1:2	1:3	1:4
Volume Fraction	0.3	82.8	83.3	83.6	83.6
	0.35	92.6	92.7	93.1	93.2
	0.4	105	105	105	106
	0.45	118	119	119	121
	0.5	135	136	135	137
	0.55	159	155	157	157
	0.6	193	185	185	186
	0.65	226	230	224	220

TABLE 5: NUMERICAL RESULTS FOR THE TRANSVERSE SHEAR MODULUS OF THE COMPOSITE

The corresponding predictions for the lower and upper Hashin-Shtrikman and three-point bounds are listed in Table 6.

Fiber VF	GT lower 3PB	GT upper TPB	GT lower HSB	GT upper HSB
0	48.4	48.4	48.4	48.4
0.05	52.4	54.0	52.4	93.1
0.1	56.9	63.3	56.8	141
0.15	62.1	76.7	61.7	193
0.2	68.0	94.6	67.2	248
0.25	74.9	118	73.4	308
0.3	82.8	147	80.5	373
0.35	92.1	182	88.6	444
0.4	103	226	98.0	522
0.45	116	279	109	607
0.5	132	343	122	700
0.55	152	420	138	804
0.6	176	512	158	920
0.65	208	624	182	1050
0.7	249	760	214	1200

TABLE 6: THREE-POINT AND HASHIN-SHTRIKMAN BOUNDS FOR THE TRANSVERSE SHEAR MODULUS OF THE COMPOSITE

Figure 31 shows a comparison between a fit to the numerical estimates for the identical fibers and the analytical bounds. As the fibers are stiffer than the matrix, the numerical results closely approach the lower bounds, especially the three-point bounds.

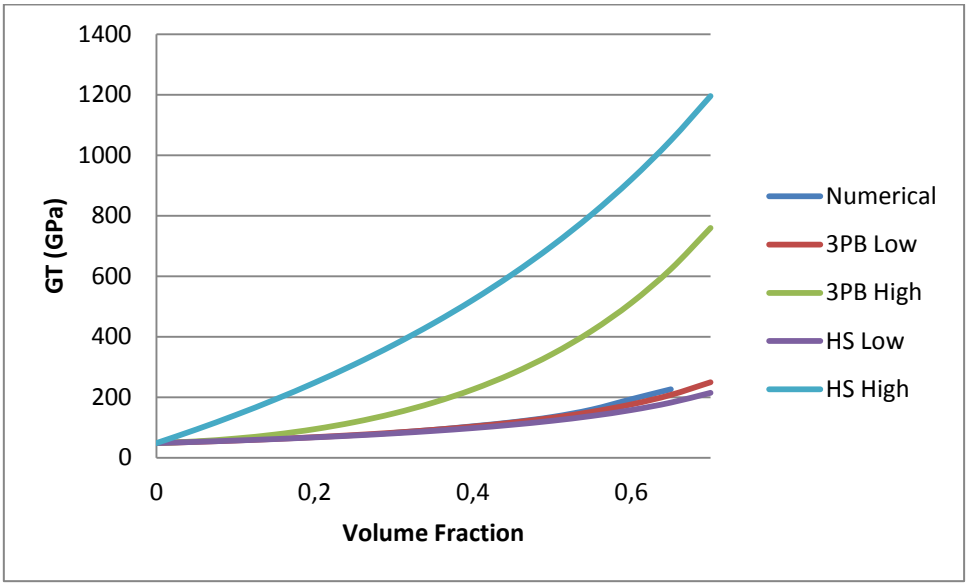

FIGURE 31: NUMERICAL RESULTS AND ANALYTICAL LOWER AND UPPER BOUNDS FOR GT

Figure 32 shows the evolution of the transverse shear modulus for different volume fractions and different diameter ratios. All ensemble averages obtained for identical fibers exceed both the three-point and the Hashin-Shtrikman bounds.

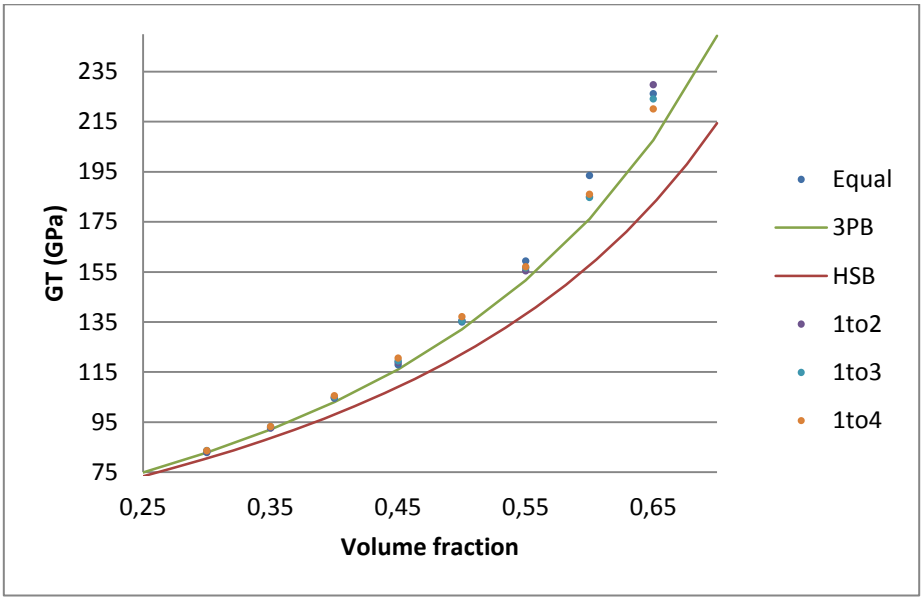

FIGURE 32: NUMERICAL RESULTS FOR GT COMPARED WITH LOWER BOUNDS FOR THE COMPOSITE

Figures 33 to 35 show that the maximum separation between the different diameter ratios is no bigger than 10GPa for all the three volume fractions displayed.

Some small differences can be noticed between the three volume fractions, the separation growing smaller from the volume fraction of 0.35 to the volume fraction of 0.5 and increasing again for the volume fraction 0.65. The predicted ranges of the transverse shear modulus due to fiber diameter effects range between 1% and 4% of the pertinent value of the modulus. The results can only be viewed as statistically significant for the volume fractions of 0.6 and 0.65.

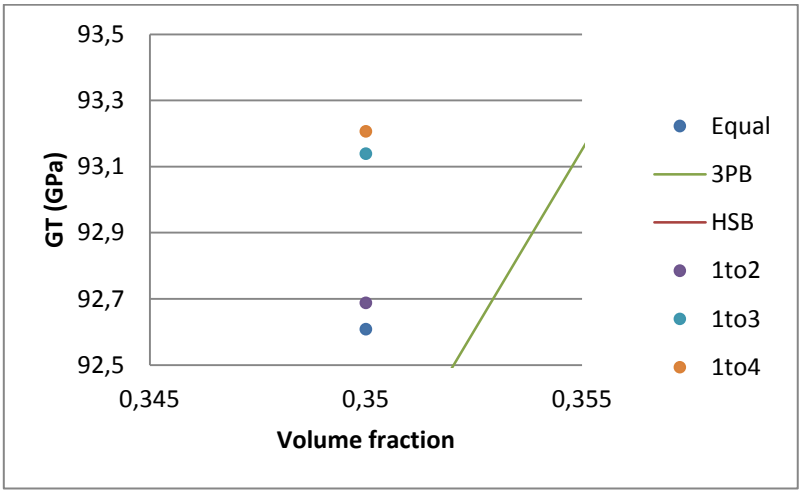

FIGURE 33: DETAIL FOR THE TRANSVERSE SHEAR MODULUS AT FIBER VOLUME FRACTION 0.35

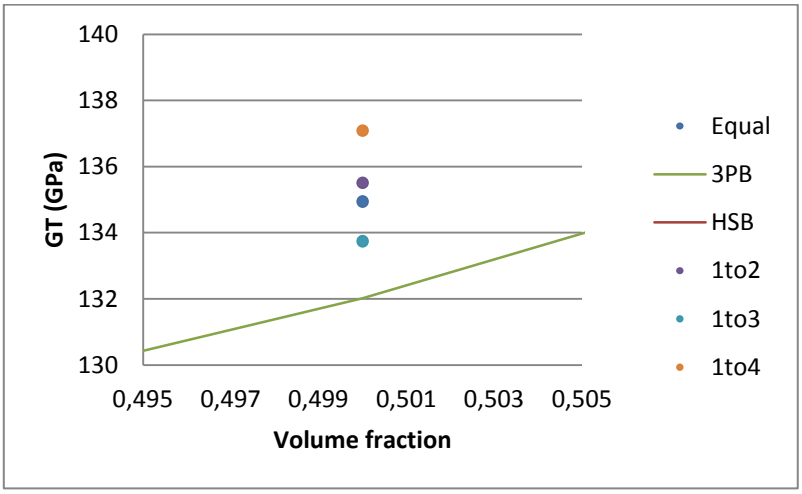

FIGURE 34: DETAIL FOR THE TRANSVERSE SHEAR MODULUS AT FIBER VOLUME FRACTION 0.5

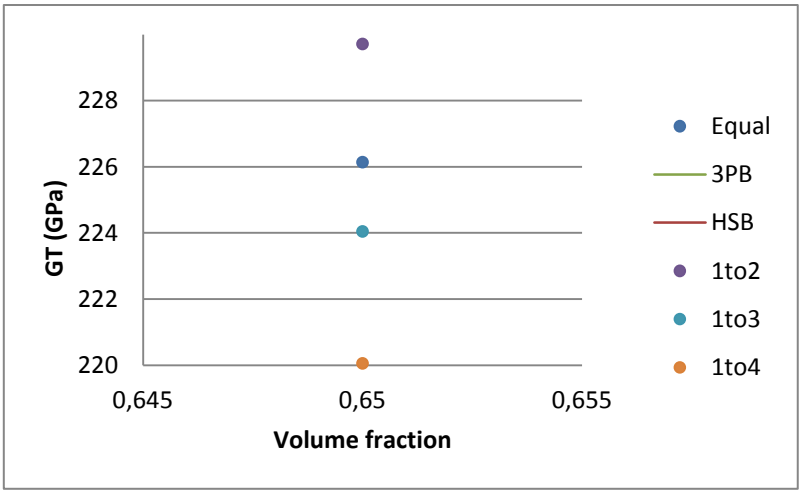

FIGURE 35: DETAIL FOR THE TRANSVERSE SHEAR MODULUS AT FIBER VOLUME FRACTION 0.65

3.2.1.4 AXIAL SHEAR MODULUS OF THE COMPOSITE

The predictions for the axial shear modulus G_A are also given in GPa. This modulus tends to increase with increasing fiber volume fraction, compare Table 7. Again changes due to differences in diameter ratio are very small compared to changes derived from differences in volume fraction. Regarding the effects of the diameter ratio, the results show a tendency to give a higher stiffness as diameter ratio decreases, for almost all volume fractions considered here.

GA		Diameter Ratio			
		Equal	1:2	1:3	1:4
Volume Fraction	0.3	88.8	89.4	82.6	90.2
	0.35	99.6	99.8	101	101
	0.4	112	113	113	114
	0.45	126	128	130	132
	0.5	143	144	146	150
	0.55	168	164	167	170
	0.6	203	194	198	202
	0.65	231	239	236	235

TABLE 7: NUMERICAL RESULTS FOR THE AXIAL SHEAR MODULUS OF THE COMPOSITE

Table 8 shows the three-point and Hashin-Shtrikman bounds obtained for the axial shear modulus.

Fiber VF	GA Lower 3PB	GA Upper 3PB	GA Lower HSB	GA Upper HSB
0	48.4	48.4	48.4	48.4
0.05	53.3	55.4	53.3	118
0.1	58.9	67.3	58.7	191
0.15	65.1	84.7	64.7	268
0.2	72.2	108	71.5	349
0.25	80.4	138	79.1	434
0.3	89.7	174	87.8	525
0.35	100	219	97.7	621
0.4	113	273	109	722
0.45	128	337	123	830
0.5	146	413	139	946
0.55	168	502	158	1070
0.6	194	608	181	1200
0.65	228	732	211	1340
0.7	272	879	250	1490

TABLE 8: THREE-POINT AND HASHIN-SHTRIKMAN BOUNDS FOR THE AXIAL SHEAR MODULUS OF THE COMPOSITE

Figure 36 compares the numerical predictions obtained for G_A (using identical fibers) and the analytical bounds. It can be observed that the numerical values are really close to the lower three point bound, to the point that they are hardly distinguishable from it. It can also be appreciated how the Hashin-Strikman bounds are slacker that the three point bounds, due to their two point bound nature.

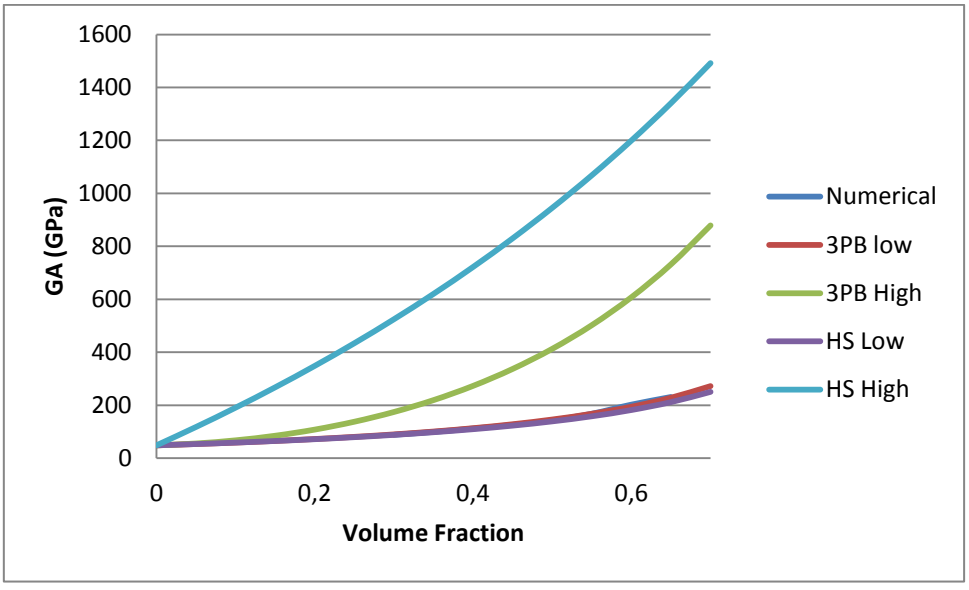

FIGURE 36: NUMERICAL RESULTS AND ANALYTICAL LOWER AND UPPER BOUNDS FOR GA

Figure 37 again plots the axial shear modulus versus the volume fraction. The results for identical fibers fall slightly below the lower three-point bounds for the four lowest volume fractions, but are always above the Hashin-Shtrikman bounds.

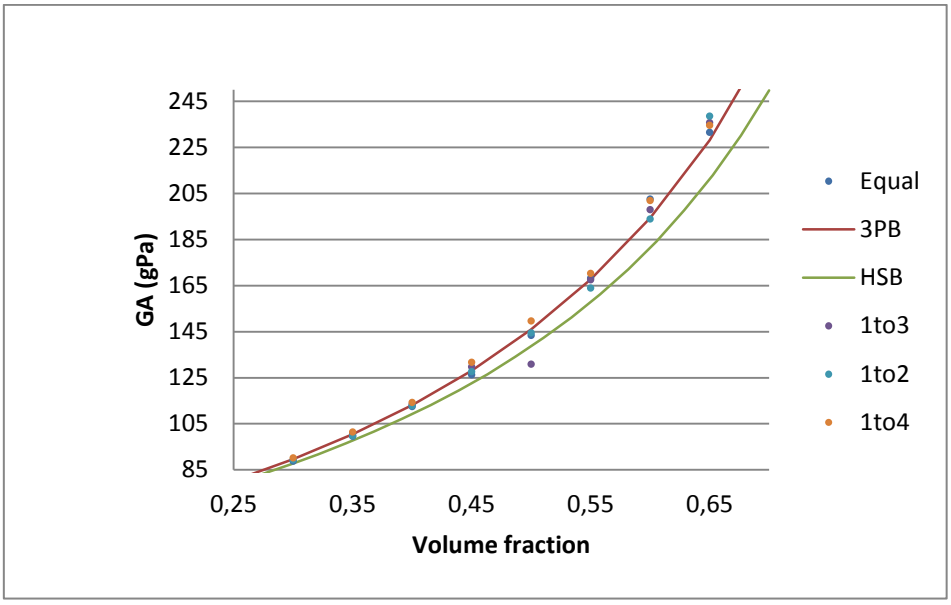

FIGURE 37: NUMERICAL RESULTS FOR GA COMPARED WITH LOWER BOUNDS FOR THE COMPOSITE

In Figures 38 to 40, the differences in stiffness for different diameter ratios tend to become more marked as the volume fraction increases and identical fibers give the lowest shear modulus for all volume fractions. The stiffness increases as the aspect ratio decreases for the 0.35 and 0.45 volume fraction cases, but not for the highest volume fraction, where the 0.25 and 0.5 aspect ratio averaged test results exchange positions.

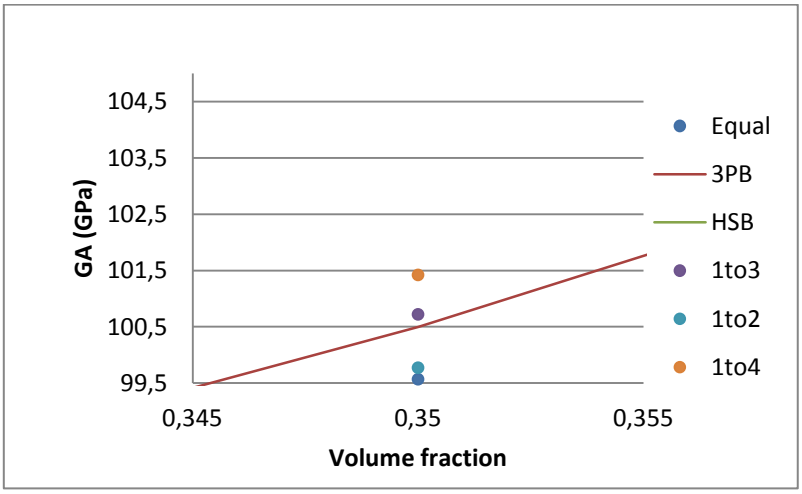

FIGURE 38: DETAIL FOR THE AXIAL SHEAR MODULUS AT FIBER VOLUME FRACTION 0.35

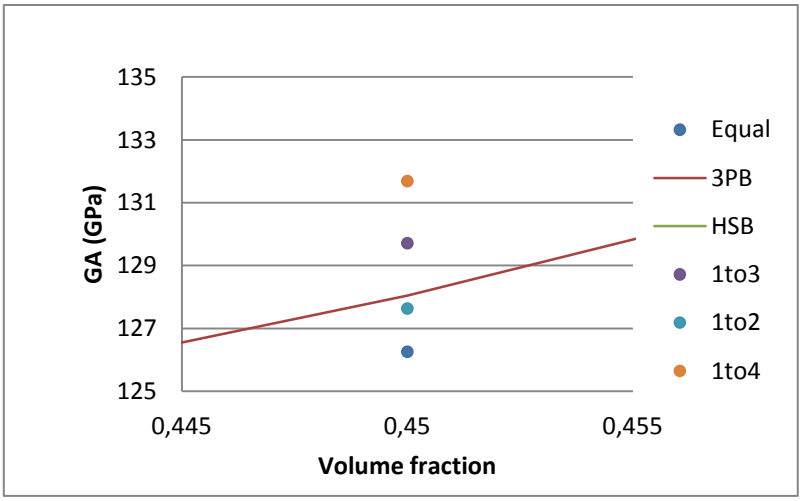

FIGURE 39: DETAIL FOR THE AXIAL SHEAR MODULUS AT FIBER VOLUME FRACTION 0.45

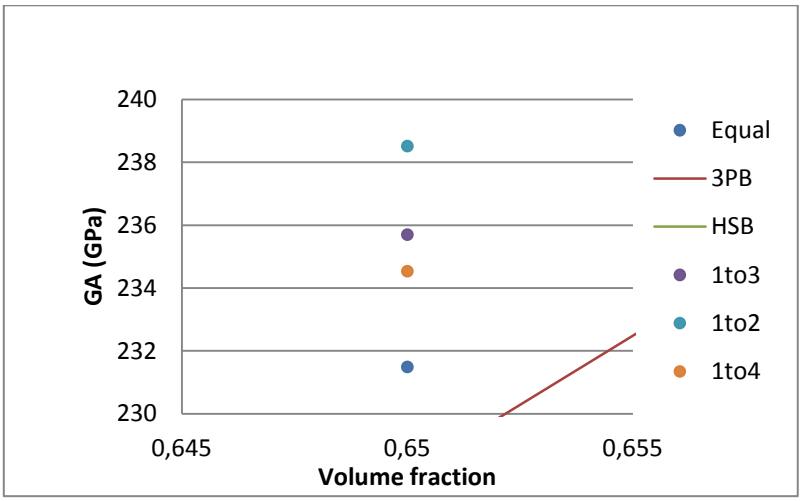

FIGURE 40: DETAIL FOR THE AXIAL SHEAR MODULUS AT FIBER VOLUME FRACTION 0.65

3.2.1.5 TRANSVERSE BULK MODULUS

The predictions for the transverse bulk modulus k_T, which are also given in GPa, show a rather small dependence on the diameter ratio, compare Table 9. Nevertheless, some small increase can be appreciated from the equal ratio case to the 0.25 ratio case for the smaller volume fractions. The higher volume fraction cases do not show any clear dependence on the diameter ratio regarding the transverse bulk modulus.

KT		Diameter Ratio			
		Equal	1:2	1:3	1:4
Volume Fraction	0.3	238	238	239	239

	0.35	259	259	260	261
	0.4	285	285	285	286
	0.45	313	314	316	313
	0.5	347	348	349	354
	0.55	394	388	392	394
	0.6	457	444	448	453
	0.65	517	526	520	517

TABLE 9: NUMERICAL RESULTS FOR THE TRANSVERSE BULK MODULUS OF THE COMPOSITE

Table 10 shows the analytical upper and lower bounds Hashin-Shtrikman and three point bounds. The values are given in GPa.

Fiber VF	KT lower 3PB	KT upper 3PB	KT lower HSB	KT upper HSB
0	155	155	155	155
0.05	165	167	165	244
0.1	177	185	176	339
0.15	189	209	189	440
0.2	204	240	203	548
0.25	220	278	219	664
0.3	239	325	237	788
0.35	260	382	257	922
0.4	285	451	281	1070
0.45	314	533	308	1220
0.5	348	631	341	1390
0.55	390	748	380	1580
0.6	441	889	428	1780
0.65	504	1060	488	2000
0.7	587	1270	566	2250

TABLE 10: ANALYTICAL BOUNDS FOR THE TRANSVERSE BULK MODULUS

Figure 41 provides a comparison between the numerical values obtained for the bulk modulus (identical fibers) and the analytical bounds provided by the Hashin-Shtrikman and the three-point bound methods. As for all the other moduli seen before, the numerical values are very close to the lower bound due to the higher stiffness of the fibers. In this case, both Hashin-Shtrikman and three-point bounds methods give rise to very similar results, which are, also really close to the obtained numerical results.

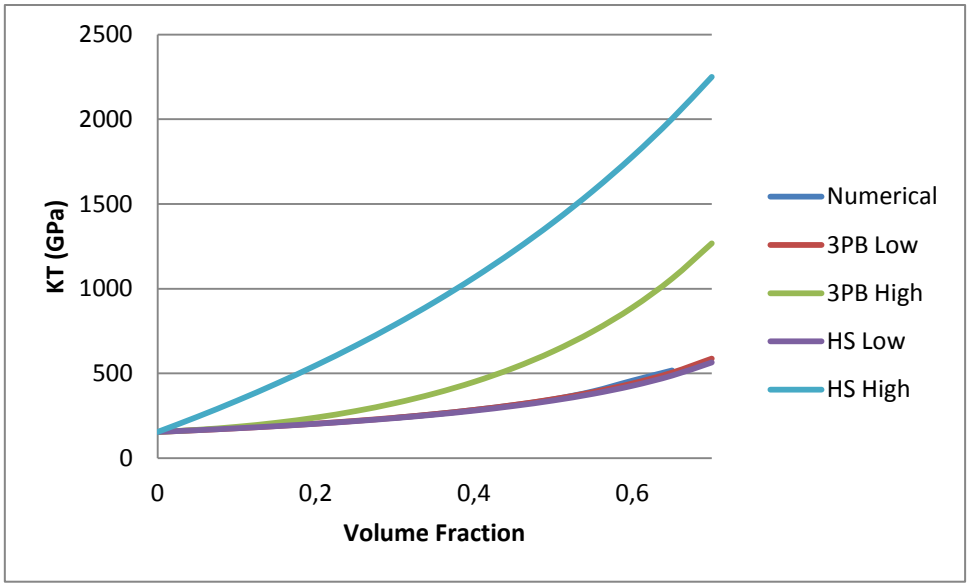

FIGURE 41: NUMERICAL RESULTS AND ANALYTICAL LOWER AND UPPER BOUNDS FOR KT

In Figure 42 the numerical results for K_T pertaining to identical fibers are compared to the lower bounds. Some of the numerical values shown there fall below the bounds.

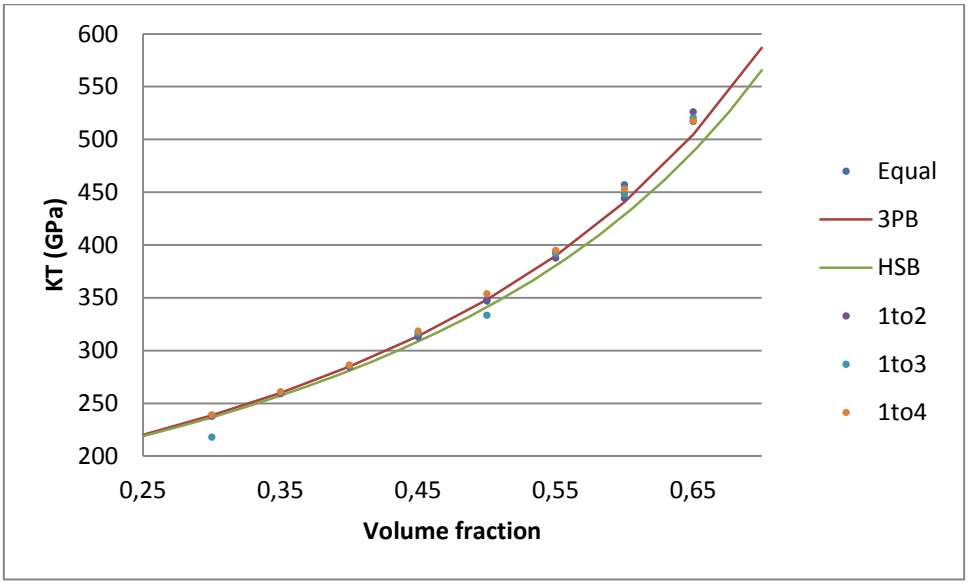

FIGURE 42: NUMERICAL RESULTS FOR KT COMPARED WITH LOWER BOUNDS FOR THE COMPOSITE

At the volume fraction of 0.35 the numerical values for all studied diameter ratios have a span of only 2 GPa. This range increases between with increasing volume fraction. The smaller diameter ratio gives the highest transverse bulk modulus for all volume fractions, and the identical fibers lead to the lowest value.

The value corresponding to the latter configuration cannot be seen for the 0.35 volume fraction because it is identical to the point for diameter ratio of 0.5.

Figures 43 to 45 show the detailed predictions of the numerical values of the transverse shear modulus for the volume fractions of 0.35, 0.5 and 0.65

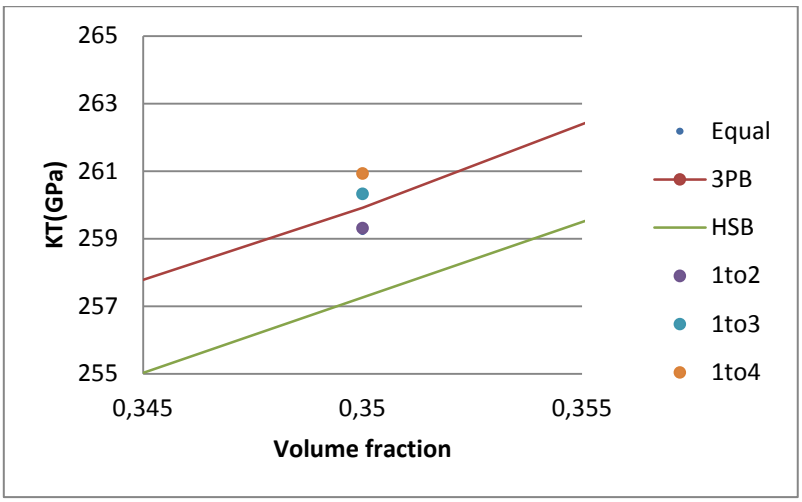

FIGURE 43: DETAIL FOR THE TRANSVERSE BULK MODULUS AT FIBER VOLUME FRACTION 0.35

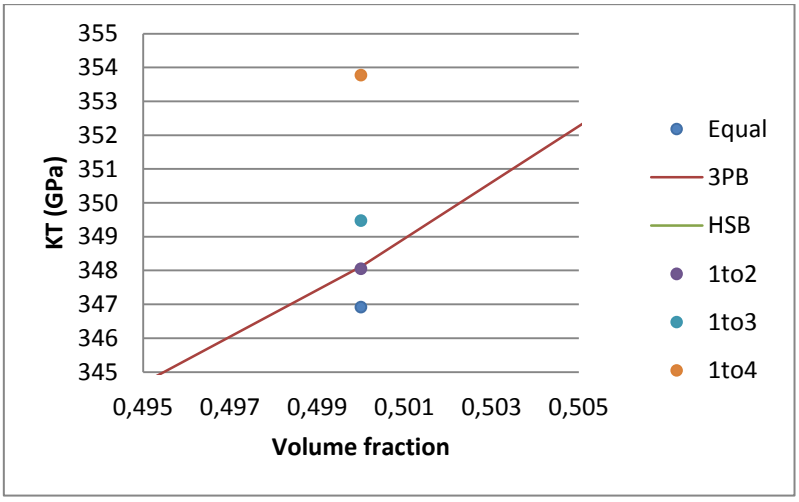

FIGURE 44: DETAIL FOR THE TRANSVERSE BULK MODULUS AT FIBER VOLUME FRACTION 0.5

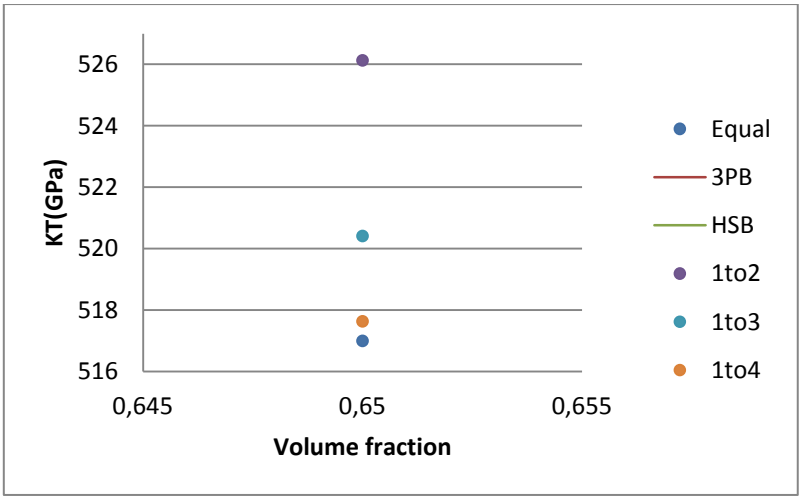

FIGURE 45: DETAIL FOR THE TRANSVERSE BULK MODULUS AT FIBER VOLUME FRACTION 0.65

3.2.1.6 TRANSVERSE POISSON COEFFICIENT OF THE COMPOSITE

The results for the transverse Poisson coefficient are not dimensional, as they indicate the ratio between two transverse strains. In table 11 no significant dependence on the diameter ratio is evident for the lower volume fractions. For volume fractions exceeding 0.55, the transverse Poisson coefficient tends to increase a little with decreasing diameter ratio.

υ^T		Diameter Ratio			
		Equal	1:2	1:3	1:4
Volume Fraction	0.3	0.468	0.467	0.466	0.467
	0.35	0.460	0.460	0.459	0.460
	0.4	0.450	0.450	0.450	0.449
	0.45	0.440	0.439	0.440	0.438
	0.5	0.428	0.428	0.417	0.429
	0.55	0.412	0.416	0.418	0.420
	0.6	0.394	0.401	0.405	0.407
	0.65	0.379	0.380	0.386	0.392

TABLE 11: NUMERICAL RESULTS FOR THE TRANSVERSE POISSON COEFFICIENT OF THE COMPOSITE

3.2.1.7 AXIAL POISSON COEFFICIENT OF THE COMPOSITE

The axial Poisson's coefficient is also non dimensional. In table 12 no significant difference can be observed here for different diameter ratios at any given volume fraction.

υ^A		Diameter Ratio			
		Equal	1:2	1:3	1:4
Volume Fraction	0.3	0.292	0.292	0.293	0.292
	0.35	0.284	0.284	0.284	0.283
	0.4	0.276	0.276	0.276	0.276
	0.45	0.269	0.268	0.268	0.267
	0.5	0.262	0.261	0.244	0.260
	0.55	0.254	0.255	0.254	0.253
	0.6	0.245	0.247	0.246	0.246
	0.65	0.240	0.239	0.239	0.240

TABLE 12: NUMERICAL RESULTS FOR THE AXIAL POISSON COEFFICIENT OF THE COMPOSITE

3.2.2 POROUS MATERIAL

3.2.2.1 TRANSVERSE YOUNG'S MODULUS OF THE POROUS MATERIAL

In Table 13 the numerical predictions for the transverse Young's modulus of the porous materials are listed in units of GPa. Obviously the values for the transverse Young's modulus are lower than the ones obtained for the composite, as there are no reinforcements to add extra stiffness here. The transverse elastic modulus decreases with increasing void volume fraction and also shows a dependence on the diameter ratio. For the same volume fraction, the stiffness tends to decrease with decreasing diameter ratio in the case of the lower volume fractions (from 0.3 to 0.5, both inclusive). For the highest volume fractions however this tendency is reversed, giving the 1:4 diameter ratio a higher stiffness than the equal diameter ratio case.

ET		Diameter Ratio			
		Equal	1:2	1:3	1:4
Volume Fraction	0.3	55.1	54.0	53.5	53.0
	0.35	46.5	46.1	45.5	44.7
	0.4	38.2	37.7	37.5	36.9
	0.45	32.0	31.3	30.6	29.6
	0.5	26.2	25.9	24.9	24.7
	0.55	19.8	20.8	2..2	20.0
	0.6	13.4	15.2	15.2	15.0
	0.65	10.5	9.82	11.0	10.7

TABLE 13: NUMERICAL RESULTS FOR THE TRANSVERSE YOUNG'S MODULUS OF THE POROUS MATERIAL

Table 14 lists the upper Hashin-Shtrikman and three-point upper bounds for the transverse Young's modulus. The values are given in GPa.

VF	ET upper HSB	ET upper 3PB
0.3	61.0	57.7
0.35	53.7	49.9
0.4	47.2	42.9
0.45	41.2	36.7
0.5	35.8	31.2
0.55	30.8	26.2
0.6	26.3	21.7
0.65	22.1	17.7

TABLE 14: THREE-POINT AND HASHIN-SHTRIKMAN UPPER BOUNDS FOR THE TRANSVERSE YOUNG'S MODULUS OF THE POROUS MATERIAL

Figure 46 shows the comparison between the upper analytical bounds and the numerical values obtained for the equal fiber diameter case. The obtained numerical values fall into the range proposed by both types of bounds. As for the composite material, the three point bounds are tighter than the Hashin-Shtrikman bounds.

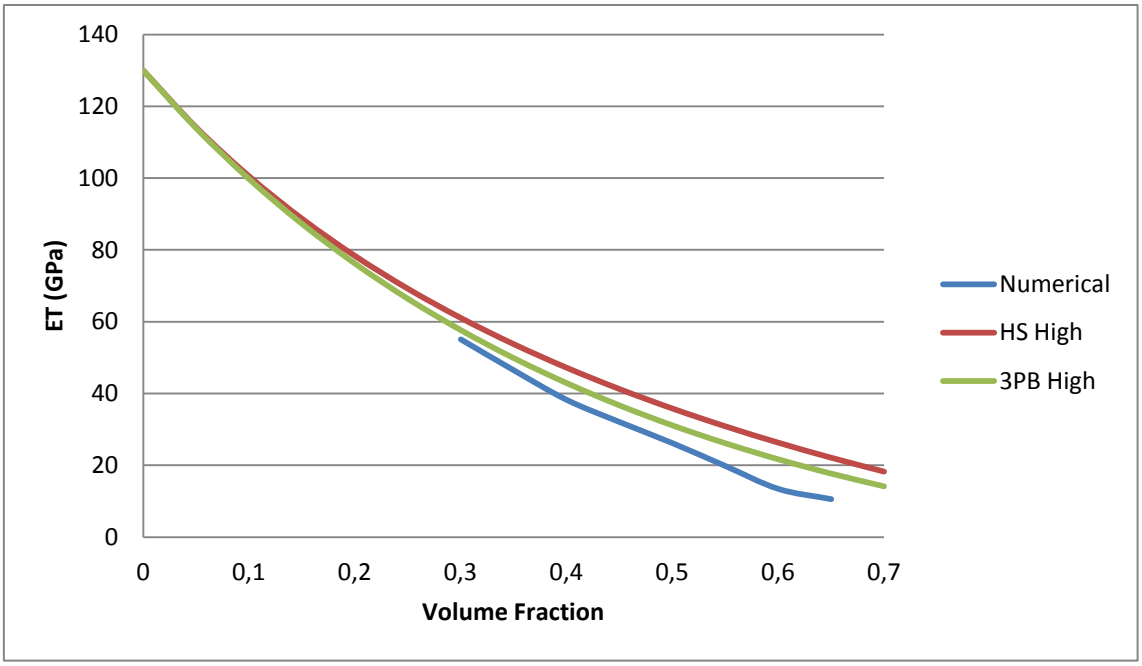

FIGURE 46: NUMERICAL RESULTS AND ANALYTICAL UPPER BOUNDS FOR ET

Figure 47 shows numerical test results in comparison with analytical bound models. For the porous material, the inhomogeneities have vanishing stiffness, so that both the Hashin-Shtrikman and the three-point lower bounds give the trivial result of zero. The numerical predictions are close to and lower than the analytical upper bounds.

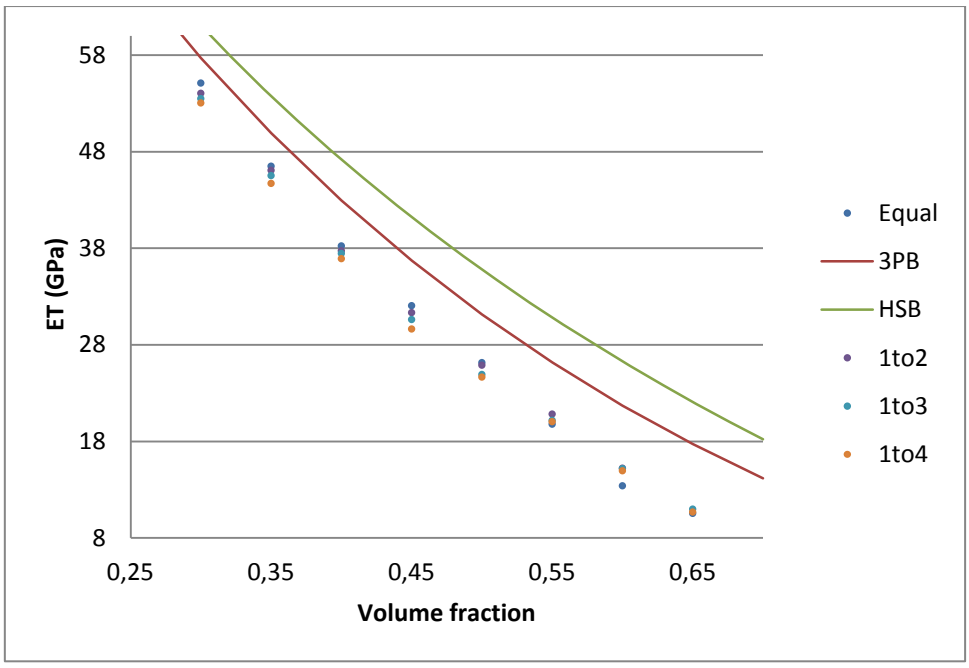

FIGURE 47: NUMERICAL RESULTS OF ET COMPARED WITH UPPER BOUNDS FOR THE POROUS MATERIAL

From the detailed plots, Figures 48 to 50, the ranges of the transverse Young's modulus covered by the different diameter ratios can be seen to be

approximately 1.8, 1.5 and 1.2 GPa for the volume fractions 0.35, 0.5 and 0.65 respectively, corresponding to approximately 4, 6 and 12% of the averaged numerical values obtained for the transverse Young's modulus. All of these ranges are clearly larger than the standard deviations, giving statistical significance to the results.

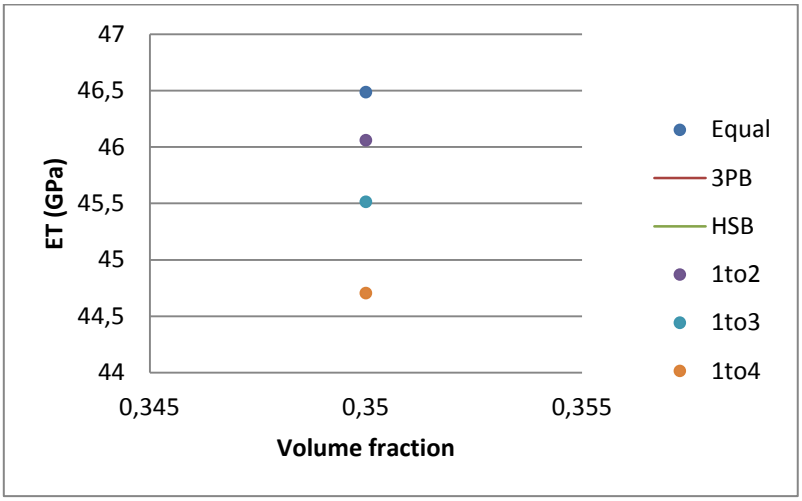

FIGURE 48: DETAIL FOR THE TRANSVERSE YOUNG'S MODULUS AT PORE VOLUME FRACTION 0.35

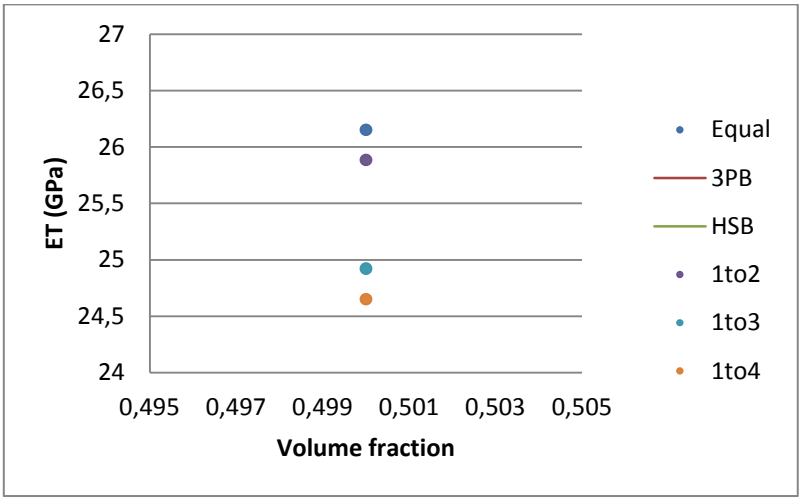

FIGURE 49: DETAIL FOR THE TRANSVERSE YOUNG'S MODULUS AT PORE VOLUME FRACTION 0.5

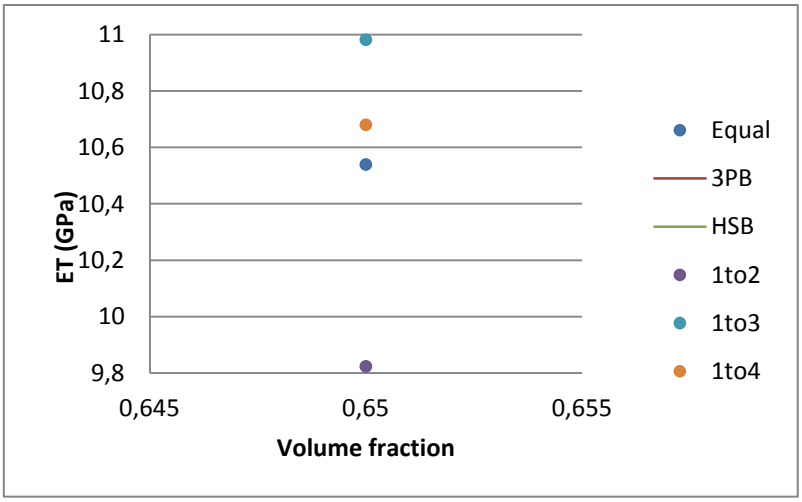

FIGURE 50: DETAIL FOR THE TRANSVERSE YOUNG'S MODULUS AT PORE VOLUME FRACTION 0.65

3.2.2.2 AXIAL YOUNG'S MODULUS

The numerical predictions for the axial Young's modulus are given in GPa. They do not show and they don't show any dependence on the diameter ratio for a given volume fraction, compare Table 15. This behavior is expected for configurations containing voids aligned with the loading direction.

EA		Diameter Ratio			
		Equal	1:2	1:3	1:4
Volume Fraction	0.3	91.0	91.0	91.0	91.0
	0.35	84.5	84.5	84.5	84.5
	0.4	78.0	78.0	78.0	78.0
	0.45	71.5	71.5	71.5	71.5
	0.5	65.0	65.0	65.0	65.0
	0.55	58.5	58.5	58.5	58.5
	0.6	52.0	52.0	52.0	52.0
	0.65	45.5	45.5	45.5	45.5

TABLE 15: NUMERICAL RESULTS FOR THE AXIAL YOUNG'S MODULUS OF THE POROUS MATERIAL

3.2.2.3 TRANSVERSE SHEAR MODULUS OF THE POROUS MATERIAL

The values of the transverse shear modulus are again given in GPa. As for the transverse Young's modulus, the stiffness decreases with falling diameter ratio for the lowest volume fractions and reverses this behavior for volume fractions exceeding 0.5.

GT		Diameter Ratio			
		Equal	1:2	1:3	1:4
Volume Fraction	0.3	20.5	20.0	19.8	19.7
	0.35	17.1	16.9	16.7	16.5
	0.4	13.8	13.6	13.5	13.3
	0.45	11.4	11.1	10.9	10.5
	0.5	9.10	9.02	8.69	8.64
	0.55	6.65	7.07	6.87	6.88
	0.6	4.30	4.99	5.05	5.01
	0.65	3.30	3.07	3.55	3.44

TABLE 16: NUMERICAL RESULTS FOR THE TRANSVERSE SHEAR MODULUS OF THE POROUS MATERIAL

Table 17 presents the upper bounds obtained for the porous material's transverse shear modulus. The differences between the values given by the analytical methods tend to be bigger as the pore volume fraction increases; the difference between the values given by both methods is 4 GPa for a volume fraction of 0.3, whereas for the 0.65 volume fraction case this difference rises to 10 GPa.

GT Porous	Hashin-Shtrikman bounds	Three Point bounds
0,3	22.8	21,4
0,35	20.4	18,4
0,4	17.6	15,8
0,45	15.4	13,5
0,5	13.3	11,4
0,55	11.5	9,52
0,6	9.8	7,86
0,65	8.2	6,38

TABLE 17: THREE-POINT AND HASHIN-SHTRIKMAN UPPER BOUNDS FOR THE TRANSVERSE SHEAR MODULUS OF THE POROUS MATERIAL

Figure 51 shows the dependence of the numerical predictions for GT on the volume fraction evaluated for identical pores, in comparison with the analytical results presented in Table 17. The difference between analytical and numerical methods grows with increasing volume fraction.

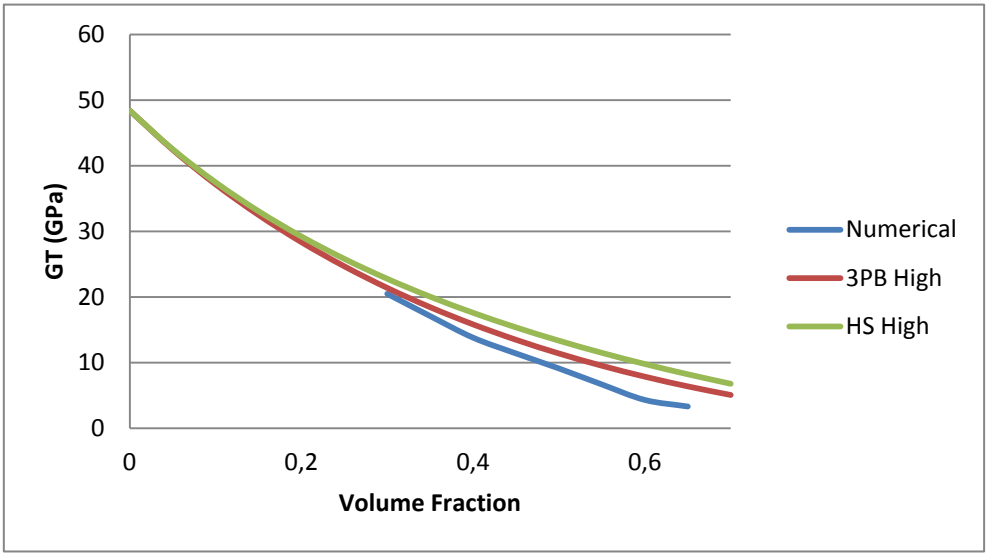

FIGURE 51: NUMERICAL RESULTS AND ANALYTICAL UPPER BOUNDS FOR GT

A clear separation between the numerically obtained data for the different diameter ratio cases and the upper analytical bounds is evident in Figure 52. This difference tends to be more marked as the volume fraction increases.

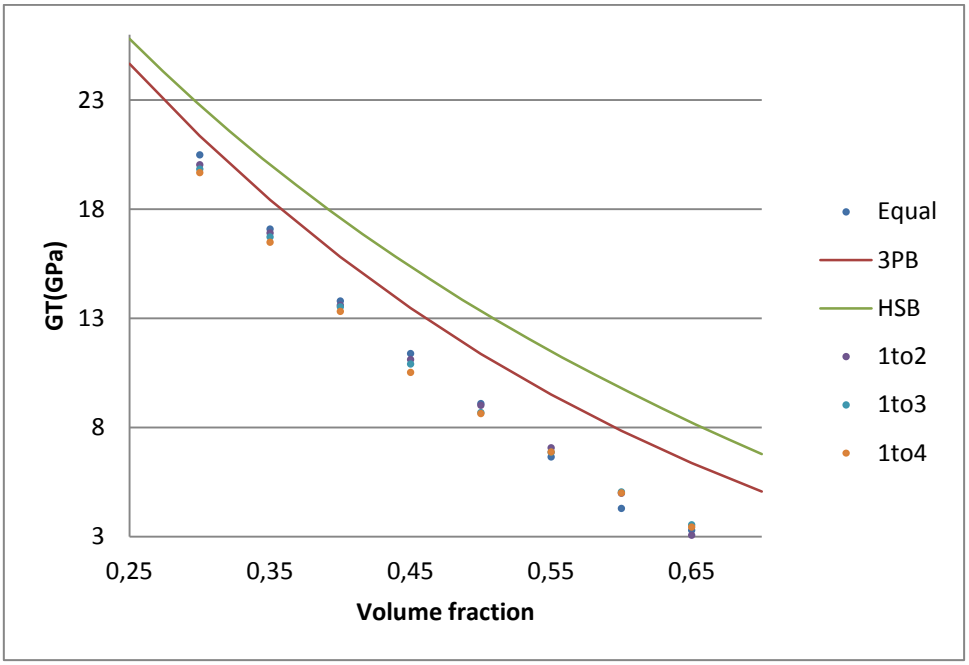

FIGURE 52: NUMERICAL RESULTS FOR GT COMPARED WITH UPPER BOUNDS FOR THE POROUS MATERIAL

Comparing Figures 53 to 55 shows a considerable qualitative difference between the 0.35, 0.5 and 0.65 volume fraction cases.

The absolute value of the difference between the lowest and the highest prediction remain nearly constant at more or less 0.5 GPa. When the sizes of the intervals are referred to the values of the transverse shear modulus, however, relative differences between 6% and 16% are found, which is higher than the standard deviations from the ensemble averaging. Accordingly, there is little question of the statistical significance of the pore size effect.

In the porous case, contrary to what was found for the composite, the diameter ratios that give the lowest stiffness in the 0.35 volume fraction case are 1:3 and 1:4. The same happens for a volume fraction of 0.5, but changes for the highest volume fraction. Diameter ratios of 1 and 0.25 show the opposite behavior.

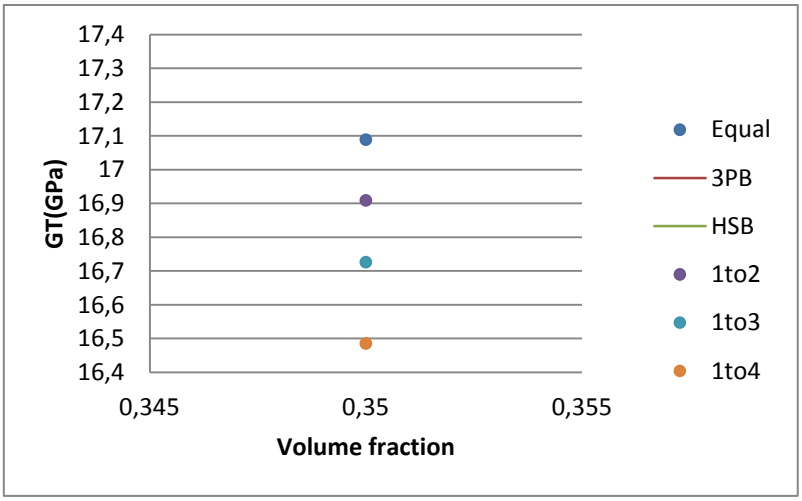

FIGURE 53: DETAIL FOR THE TRANSVERSE SHEAR MODULUS AT PORE VOLUME FRACTION 0.35

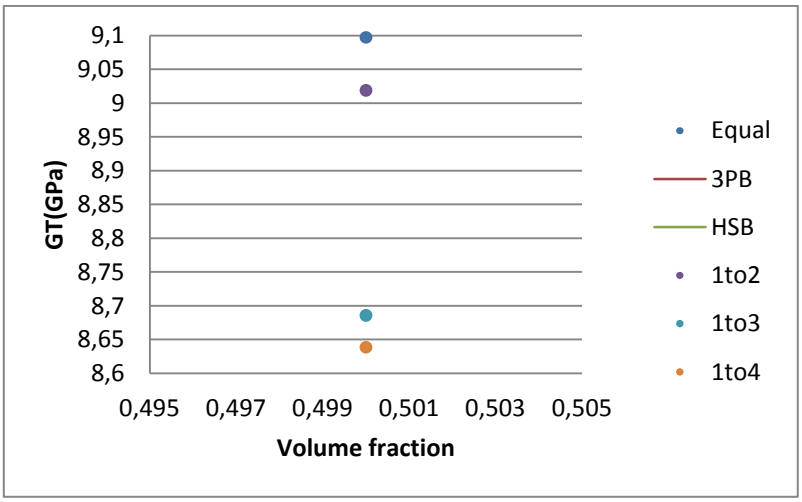

FIGURE 54: DETAIL FOR THE TRANSVERSE SHEAR MODULUS AT PORE VOLUME FRACTION 0.5

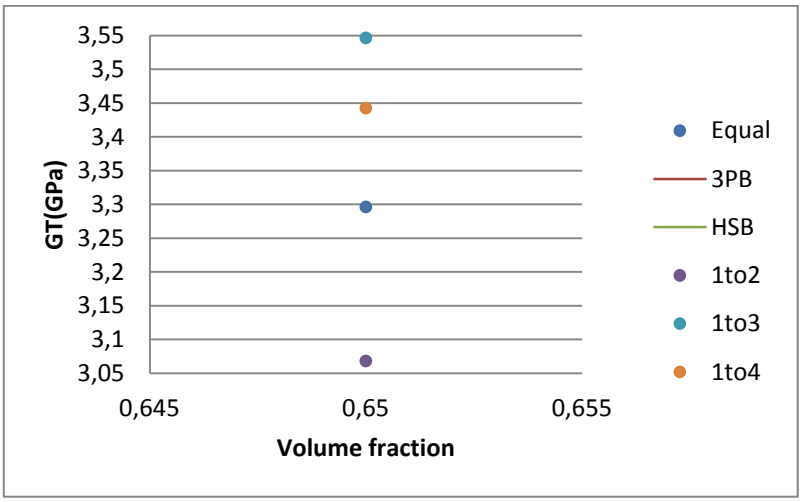

FIGURE 55: DETAIL FOR THE TRANSVERSE SHEAR MODULUS AT PORE VOLUME FRACTION 0.65

3.2.2.4 AXIAL SHEAR MODULUS OF THE POROUS MATERIAL

The numerical predictions for the axial shear modulus are given in GPa in table 18, and they tend to become slightly lower as the diameter ratio decreases for all volume fractions considered. However, the differences between different diameter ratios for the same volume fraction are not as marked as in the case of the transverse shear modulus, being approximately 0.5 GPa.

GA		Diameter Ratio			
		Equal	1:2	1:3	1:4
Volume Fraction	0.3	25.7	25.5	25.4	25.2
	0.35	22.8	22.8	22.6	22.3
	0.4	20.1	20.0	19.8	19.7
	0.45	17.7	17.5	17.2	17.0
	0.5	15.5	15.4	15.0	14.8
	0.55	13.1	13.4	13.1	12.9
	0.6	10.6	11.2	10.9	10.6
	0.65	9.19	8.79	8.87	8.71

TABLE 18: NUMERICAL RESULTS FOR THE AXIAL SHEAR MODULUS OF THE POROUS MATERIAL

Table 19 shows the analytical upper bounds for the axial transverse shear modulus. The differences between the two bounds are quite small, and tend to become smaller with decreasing volume fraction.

GA Porous	Hashin-Shtrikman bounds	Three Point bounds
0.3	26.0	25.4
0.35	23.3	22.6
0.4	20.7	19.9
0.45	18.3	17.5
0.5	16.1	15.2
0.55	14.0	13.1
0.6	12.1	11.2
0.65	10.3	9.3

TABLE 19: THREE-POINT AND HASHIN-SHTRIKMAN UPPER BOUNDS FOR THE AXIAL SHEAR MODULUS OF THE POROUS MATERIAL

In Figure 56 shows the numerical predictions for pores of equal diameter ratio as well as the upper Hashin-Shtrikman and three-point bounds aree. It can be seen that again the three-point bounds are a bit lower than the Hashin-Shtrikman ones, but the difference between them is only of the order of 10 GPa. Numerical values are very close to these two analytical bounds.

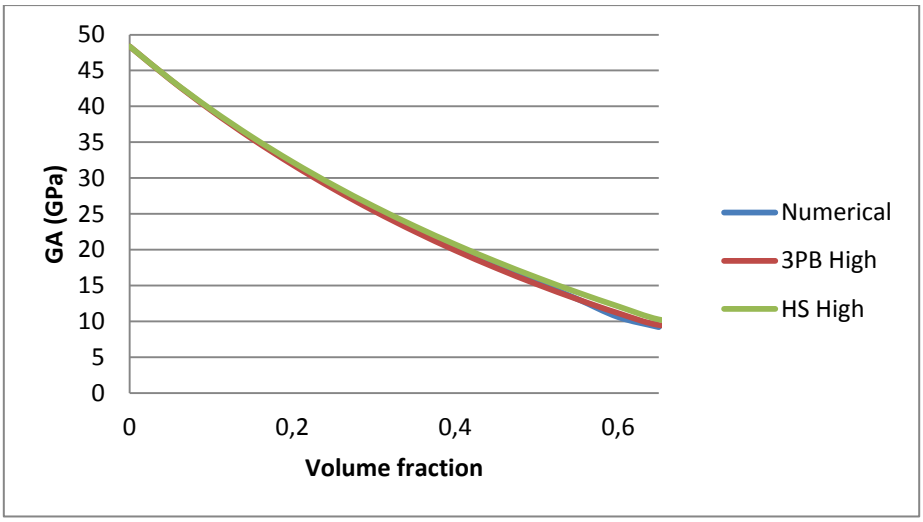

FIGURE 56: NUMERICAL RESULTS AND ANALYTICAL UPPER BOUNDS FOR GA

Figure 57 shows a detailed view, all studied diameter ratio cases being displayed for each volume fraction. In the case of the axial shear modulus, some of the numerical results lie above the upper three-point bounds for low pore volume fractions, but all numerical results are within the Hashin-Shtrikman bounds.

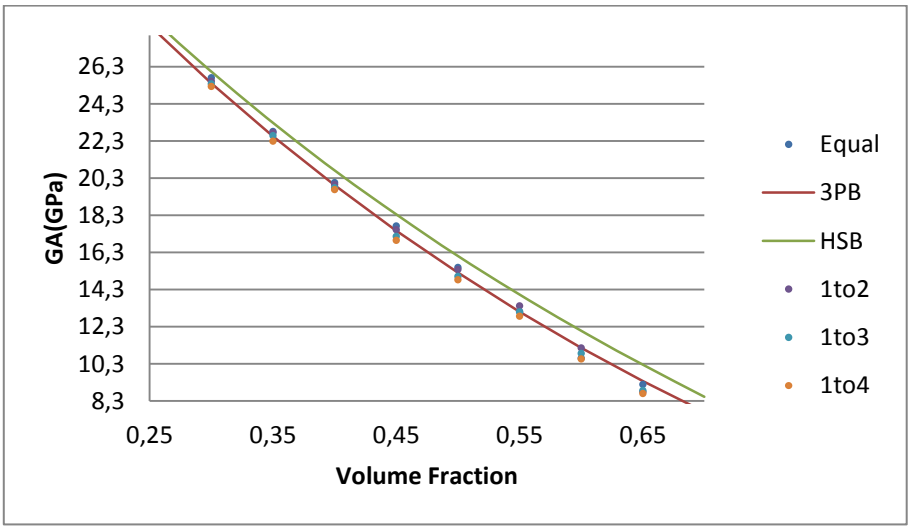

FIGURE 57: NUMERICAL RESULTS FOR GA COMPARED WITH UPPER BOUNDS FOR THE POROUS MATERIAL

The detailed figures 58 to 60 indicate that, for low to intermediate volume fractions, the highest stiffness is, in contrast to the non-porous case, achieved with the

pores of identical diameter. In contrast to the case of the composite, the shear modulus tends to decrease with decreasing pore diameter ratio.

Regarding differences in the moduli between different diameter ratios for the same volume fraction, it can be seen that the intervals tend to become bigger with increasing volume fraction. This tendency is not linear, as the differences between the volume fractions 0.5 and 0.65 volume fractions are relatively much bigger than the differences between the 0.35 and 0.5 volume fractions.

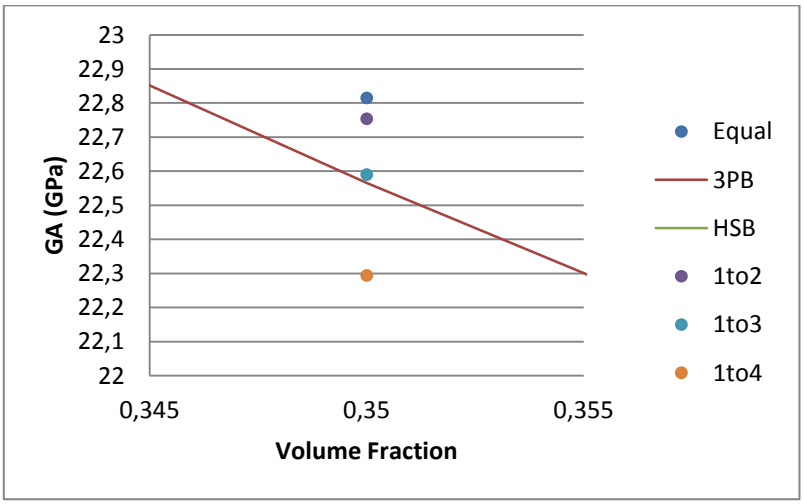

FIGURE 58: DETAIL FOR THE AXIAL SHEAR MODULUS AT PORE VOLUME FRACTION 0.35

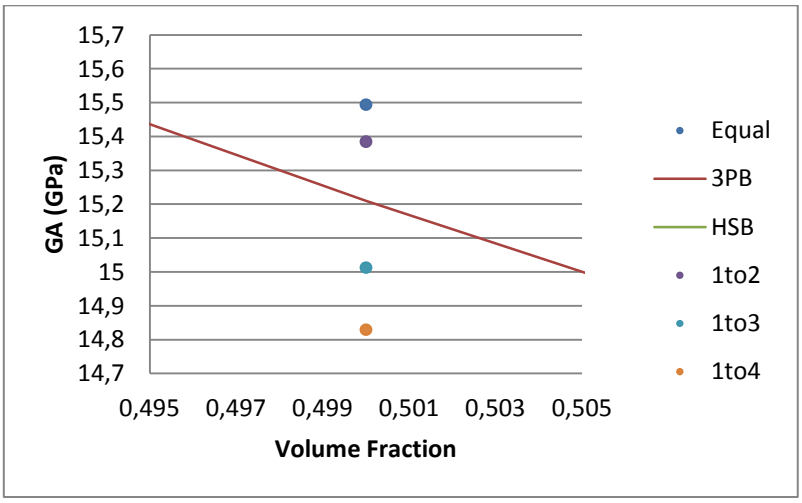

FIGURE 59: DETAIL FOR THE AXIAL SHEAR MODULUS AT PORE VOLUME FRACTION 0.5

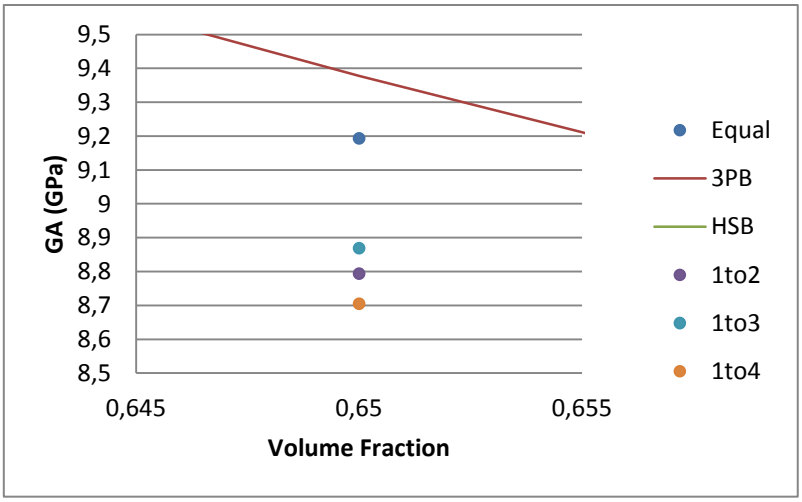

FIGURE 60: DETAIL FOR THE AXIAL SHEAR MODULUS AT PORE VOLUME FRACTION 0.65

3.2.2.5 TRANSVERSE BULK MODULUS OF THE POROUS MATERIAL

The predicted values for the transverse bulk modulus are listed in Table 20 in units of GPa. They show a tendency towards becoming lower as the diameter ratio decreases. The differences between the case of identical pores and that of a diameter ratio of 1:4 are smaller for pore volume fractions exceeding 0.55, decreasing from 2.5 GPa at a volume fraction of 0.5 to 0.6 GPa for a volume fraction of 0.6. In addition, the 0.65 volume fraction case gives a higher value for the diameter ratio of 1:4.

KT		Diameter Ratio			
		Equal	1:2	1:3	1:4
Volume Fraction	0.3	53.8	52.9	52.2	51.6
	0.35	45.6	45.2	44.5	43.1
	0.4	38.4	37.8	37.3	36.7
	0.45	32.9	32.2	30.9	30.0
	0.5	28.0	27.5	26.3	25.5
	0.55	22.8	23.5	22.4	21.6
	0.6	17.6	18.7	17.7	17.0
	0.65	15.2	14.1	13.9	16.0

TABLE 20: NUMERICAL RESULTS FOR THE TRANSVERSE BULK MODULUS OF THE POROUS MATERIAL

The upper Hashin-Shtrikman and three-point bounds evaluated for the transverse bulk modulus of the porous material are listed in table 21

KT	HS	3PB
0	155	155
0,05	127	127
0,1	106	105
0,15	89,0	87,5
0,2	75,6	73,6
0,25	64,5	62,1
0,3	55,3	52,6
0,35	47,5	44,6
0,4	40,8	37,7
0,45	34,9	31,9
0,5	29,8	26,8
0,55	25,2	22,4
0,6	21,2	18,5
0,65	17,6	15,2
0,7	14,3	12,2

TABLE 21: THREE-POINT AND HASHIN-SHTRIKMAN BOUNDS FOR THE TRANSVERSE BULK MODULUS OF THE POROUS MATERIAL

Figure 61 shows a comparison between the numerical predictions for the transverse bulk modulus obtained for identical fibers and the upper Hashin-Shtrikman and three-point bounds. The latter closely follows the line marked by the numerical values.

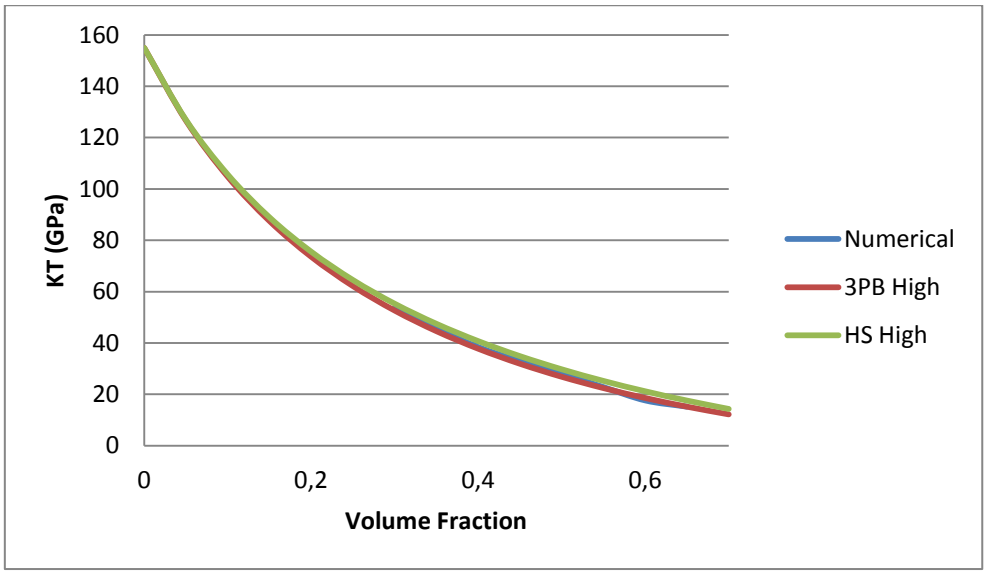

FIGURE 61: NUMERICAL RESULTS AND ANALYTICAL UPPER BOUNDS FOR KT

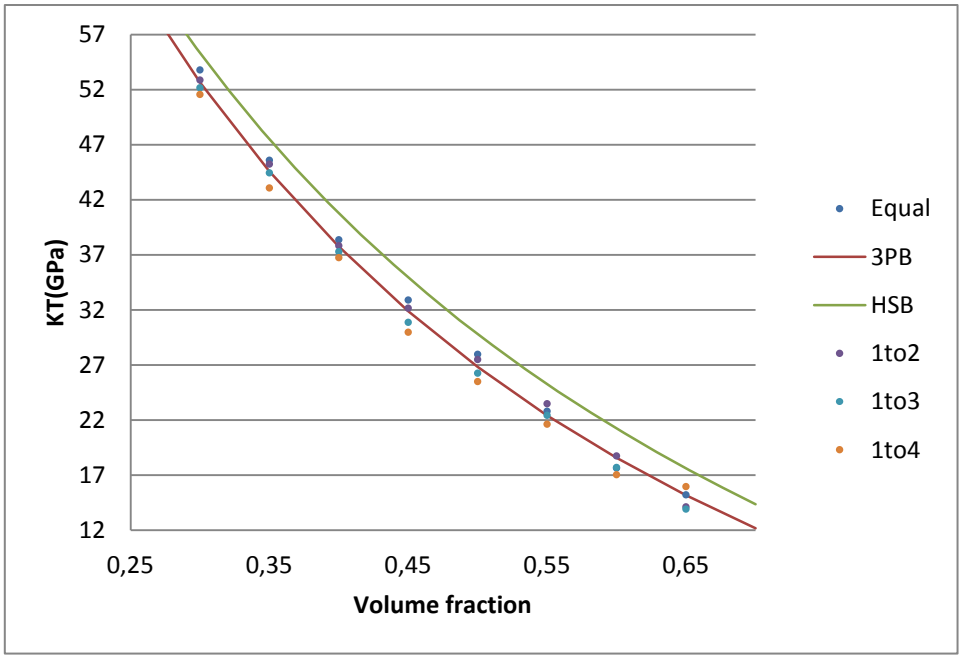

FIGURE 62: NUMERICAL RESULTS FOR KT COMPARED WITH UPPER BOUNDS FOR THE POROUS MATERIAL

Figures 63 to 65 show details for various diameter ratio cases for volume fractions of 0.3, 0.5 and 0.65 volume fractions, respectively. No big differences are evident for the different diameter ratio cases. The separation between the diameter ratio case that gives the highest bulk modulus and the one that gives the slowest one is just 3 Ga for all volume fractions displayed below.

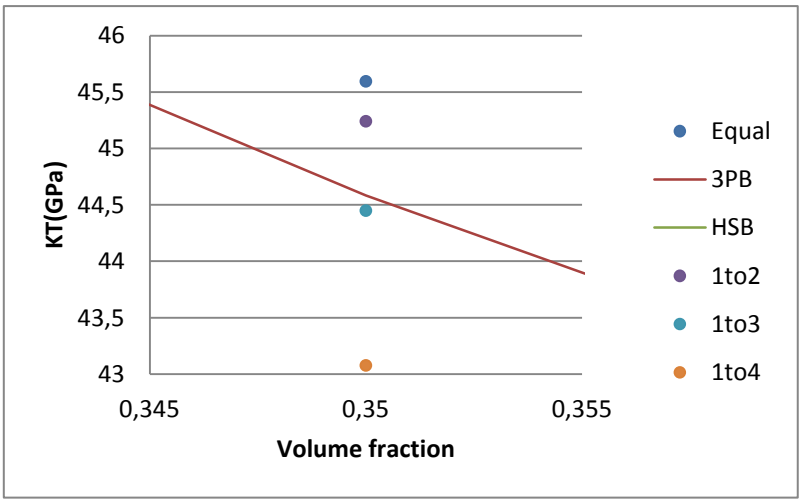

FIGURE 63: DETAIL FOR THE TRANSVERSE BULK MODULUS AT PORE VOLUME FRACTION 0.35

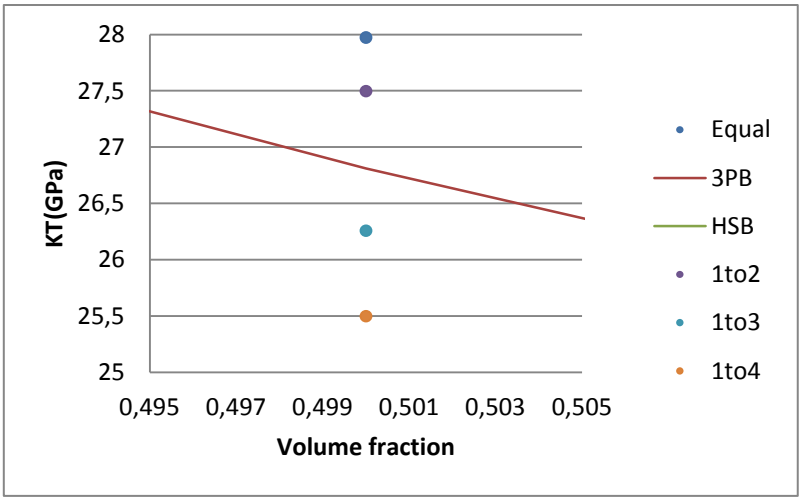

FIGURE 64: DETAIL FOR THE TRANSVERSE BULK MODULUS AT PORE VOLUME FRACTION 0.5

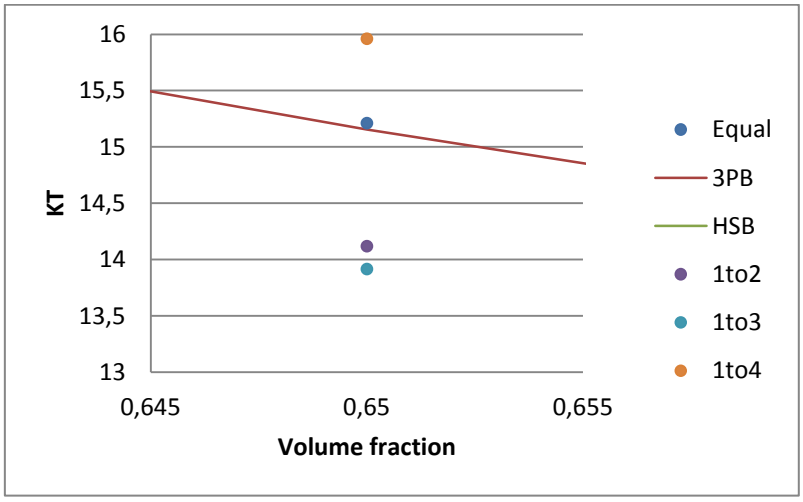

FIGURE 65: DETAIL FOR THE TRANSVERSE BULK MODULUS AT PORE VOLUME FRACTION 0.65

3.2.2.6 TRANSVERSE POISSON'S COEFFICIENT

The results for the transverse Poisson coefficient are, as stated in section 3.2.1.6, non-dimensional. The numerical predictions for the different diameter ratios displayed in Table 22 show different behaviors depending on the pore volume fraction. For volume fractions from 0.3 to 0.45, the results remain rather static for all diameter ratio cases. However, for the 0.5 to 0.65 volume fraction range, the values of the obtained results increase with increasing diameter ratio.

υ^T		Diameter Ratio			
		Equal	1:2	1:3	1:4
Volume Fraction	0.3	0.345	0.349	0.348	0.348
	0.35	0.360	0.362	0.361	0.356
	0.4	0.386	0.387	0.384	0.386
	0.45	0.407	0.409	0.403	0.408
	0.5	0.437	0.435	0.435	0.427
	0.55	0.486	0.472	0.469	0.456
	0.6	0.559	0.525	0.502	0.493
	0.65	0.599	0.601	0.548	0.551

TABLE 22: NUMERICAL RESULTS FOR THE TRANSVERSE POISSON'S COEFFICIENT OF THE POROUS MATERIAL

3.2.2.7 AXIAL POISSON'S COEFFICIENT

The results of the axial Poisson's coefficient listed in Table 23 give the same value for all volume fractions and all diameter ratio cases considered.

υ^A		Diameter Ratio			
		Equal	1:2	1:3	1:4
Volume Fraction	0.3	0.344	0.344	0.344	0.344
	0.35	0.344	0.344	0.344	0.344
	0.4	0.344	0.344	0.344	0.344
	0.45	0.344	0.344	0.344	0.344
	0.5	0.344	0.344	0.344	0.344
	0.55	0.344	0.344	0.344	0.344
	0.6	0.344	0.344	0.344	0.344
	0.65	0.344	0.344	0.344	0.344

TABLE 23: NUMERICAL RESULTS FOR THE AXIAL POISSON'S COEFFICIENT OF THE POROUS MATERIAL

3.3 MICROFIELDS

3.3.1 COMPOSITE MATERIAL

3.3.1.1 UNIAXIAL TRANSVERSE LOADS

In the following, results obtained with uniaxial load in 1-direction are shown. The following Figures show the Von Misses stress response for a volume fraction of 0.45 and a diameter ratio of 1:2. The nomenclature used for nodes edges, and faces follows Figure 5.

Figure 66 displays a map of the Von Misses effective stress pertaining to uniaxial transverse, tensile loading in the 1-direction drawn on an undeformed geometry consisting of identical fibers of volume fraction 0.45 embedded in the matrix. Due to the fibers' higher stiffness, they tipically show higher levels of the Von Misses stress, with stress concentrations forming bands of more or less horizontal orientation whenever such behavior is favored by the local arrangement of groups of fibers.

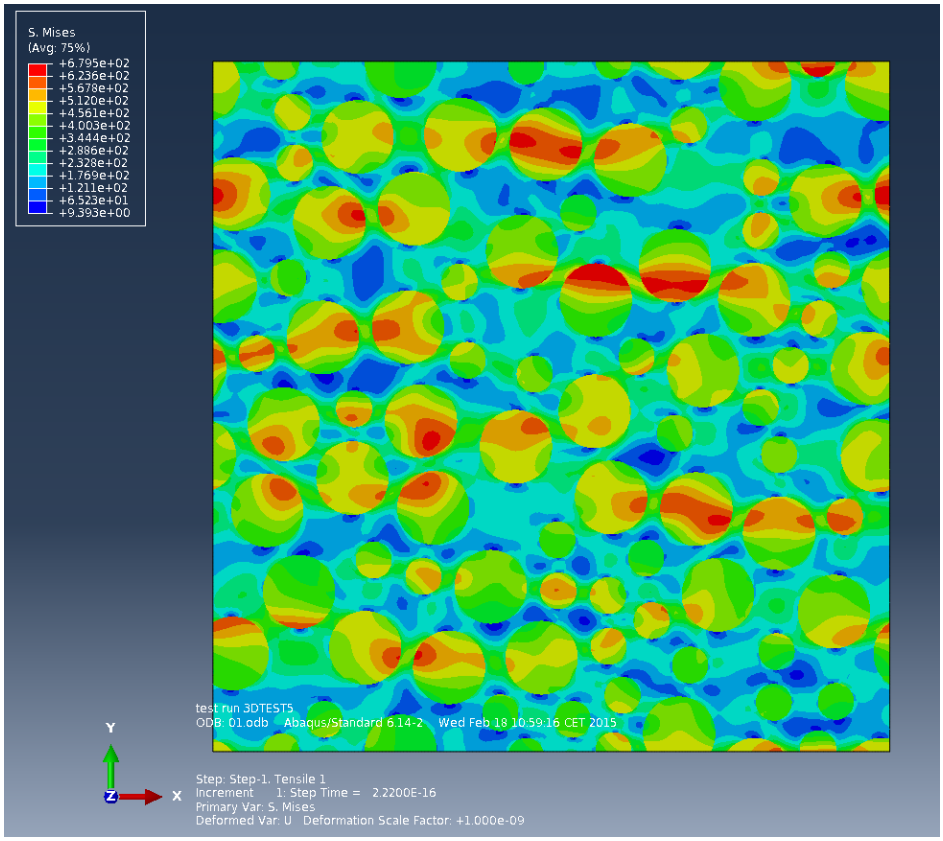

FIGURE 66: VON MISSES STRESSES FOR UNIAXIAL TENSILE TRANSVERSE LOADING IN 1-DIRECTION (IDENTICAL FIBERS OF VOLUME FRACTION 0.45)

In Figure 67, a line plot of the undeformed unit cell (dark region) is overlaid on the stress map drawn on the deformed geometry, the same volume element being used as in Figure 65. Displacements are scaled by a displacement scale factor greater than unity to aid interpretation. It is evident that the displacements of the nodes on face E are determined by the ones of the nodes on face W and by node SEB, with the volume element lengthening in the horizontal direction. In analogy, face T moves downwards and is distorted in lockstep with face B. This, of course, is the behavior to be expected when using periodicity boundary conditions, equations (4) to (6). There is some reduction in the thickness in 3-direction due to the Poisson effect, but this is not shown in Figure 67.

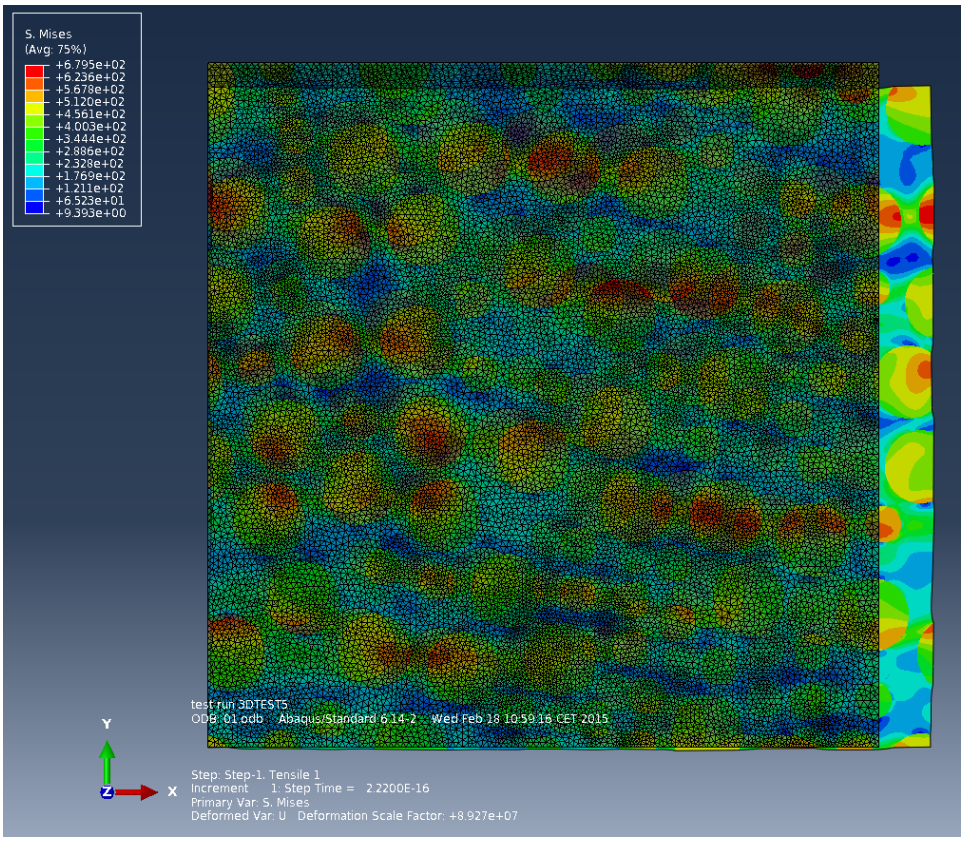

FIGURE 67: COMPARISON BETWEEN THE INITIAL AND DEFORMED STATES FOR UNIAXIAL TENSILE TRANSVERSE LOADING IN 1-DIRECTION (IDENTICAL FIBERS OF VOLUME FRACTION 0.45)

The distribution of the Von Misses stress obtained by loading with a uniaxial transverse tensile stress acting in 2-direction are plotted in figure 68, the undeformed geometry being shown. The volume element is the same one as used in Figures 66 and 67. Here, bands of elevated stresses run approximately in the vertical, rather than the horizontal direction.

Figure 69 again presents the undeformed and deformed geometries, in analogy to Figure 67. For this load case, the load is applied to node NWT. The effects of the periodicity boundary conditions are analogous to Figure 67, with the cell enlarging in Y2 direction and shrinking in 1-direction.

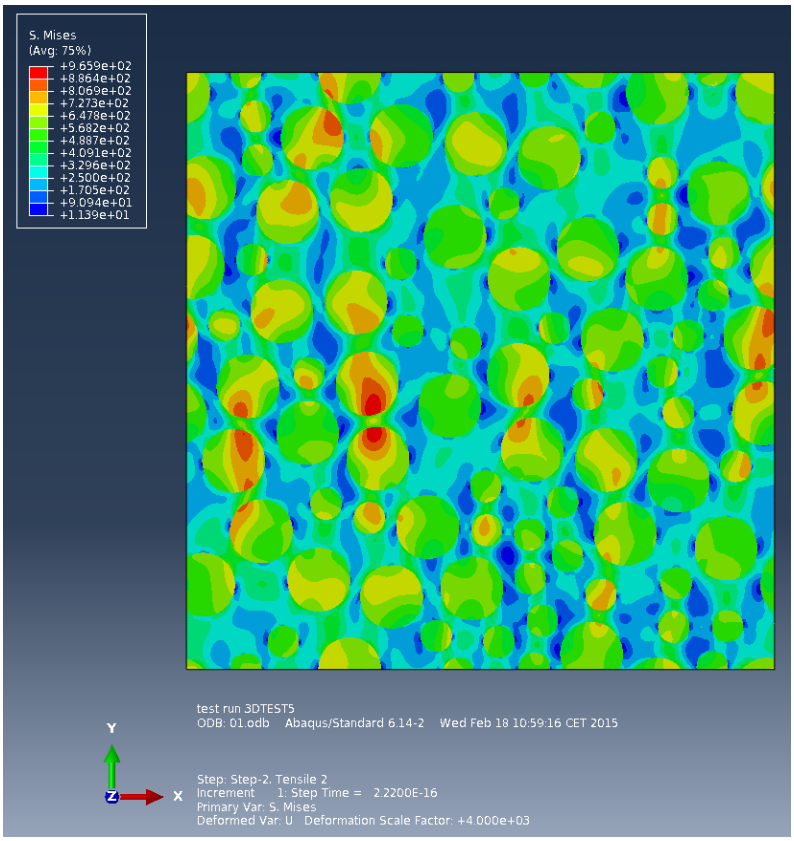

FIGURE 68: MAP OF VON MISSES STRESS FOR UNIAXIAL TENSILE TRANSVERSE LOADING IN 2-DIRECTION (IDENTICAL FIBERS OF VOLUME FRACTION 0.45)

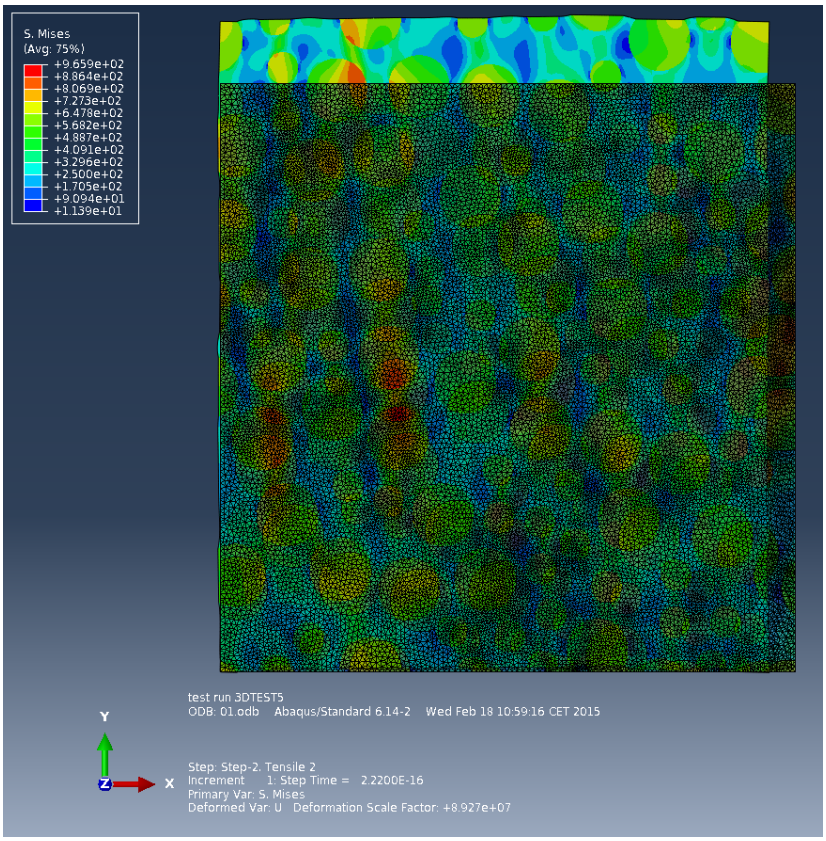

FIGURE 69: COMPARISON BETWEEN THE INITIAL AND DEFORMED STATES FOR UNIAXIAL TENSILE TRANSVERSE LOADING IN 1-DIRECTION

3.3.1.2 UNIAXIAL AXIAL LOADING OF THE COMPOSITE

Uniaxial tensile axial loading is simulated by applying a concentrated load acting in 3-direction on master node SWT. As can be seen in Figure 70, the Von Misses stresses in the matrix and fiber phases are nearly homogeneous, the small perturbations due to the different Poisson's ratios of the constituents not being evident in the plot. The initial, load-free state is again provided in the form of a line plot overlaid on the stress map. Figures 70 and 71 pertain to a composite reinforced by fibers of diameter ratio 1:2 at a volume fraction of 0.45.

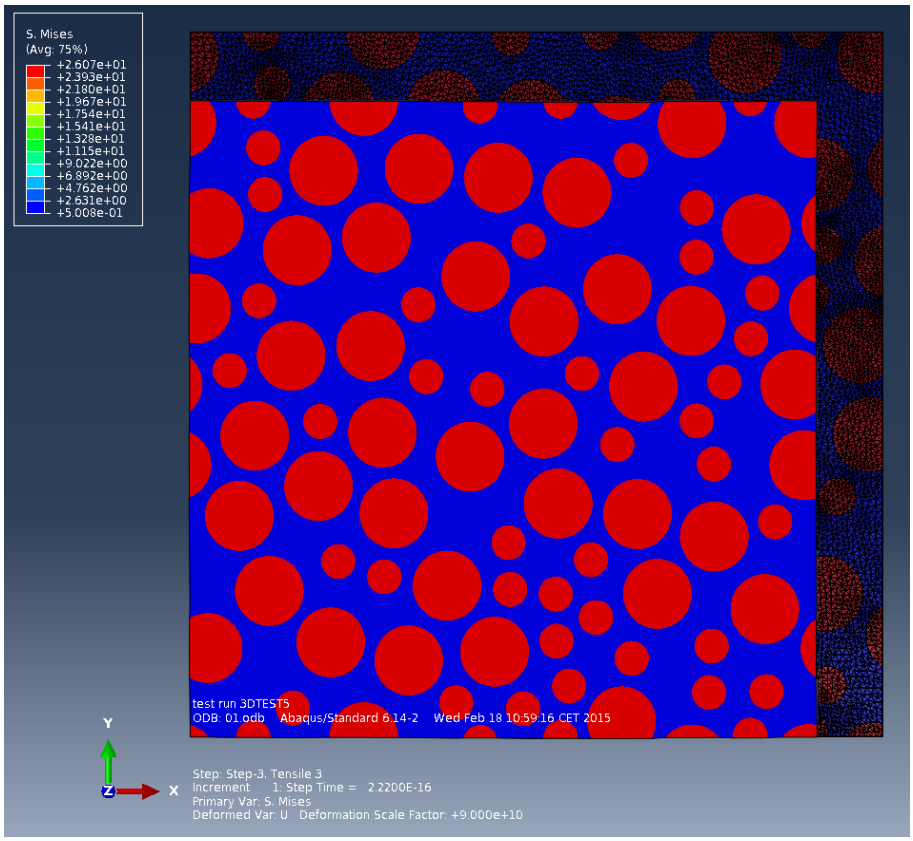

FIGURE 70: COMPARISON BETWEEN THE INITIAL AND DEFORMED STATES FOR UNIAXIAL TENSILE AXIAL LOADING (FIBERS OF DIAMETER RATIO 1:2, VOLUME FRACTION 0.45)

Whereas for this load case the volume element shrinks in the transverse plane, as is evident from Figure 70, it extends in 3-direction, thus increasing in thickness, as shown in Figure 71.

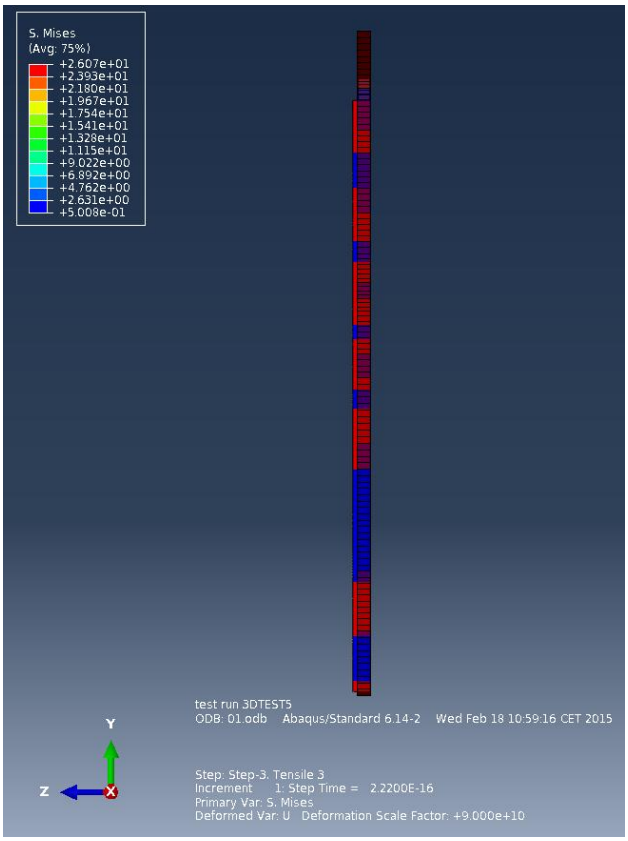

FIGURE 71: CHANGE IN THICKNESS IN 3-DIRECTION FOR UNIAXIAL TENSILE AXIAL LOADING (FIBERS OF DIAMETER RATIO 1:2, VOLUME FRACTION 0.45)

3.3.1.3 TRANSVERSE SHEAR LOADING OF THE COMPOSITE

To create this load case, a load acting in 2-direction was applied to the SEB master node. The W face follows the behavior of the E face and the N face follows that of the S face, giving rise to the deformed geometry shown in Figure 72, which also displays a map of the Von Mises stress. The volume element again corresponds to a diameter ratio of 1:2 and a volume fraction of 0.45.

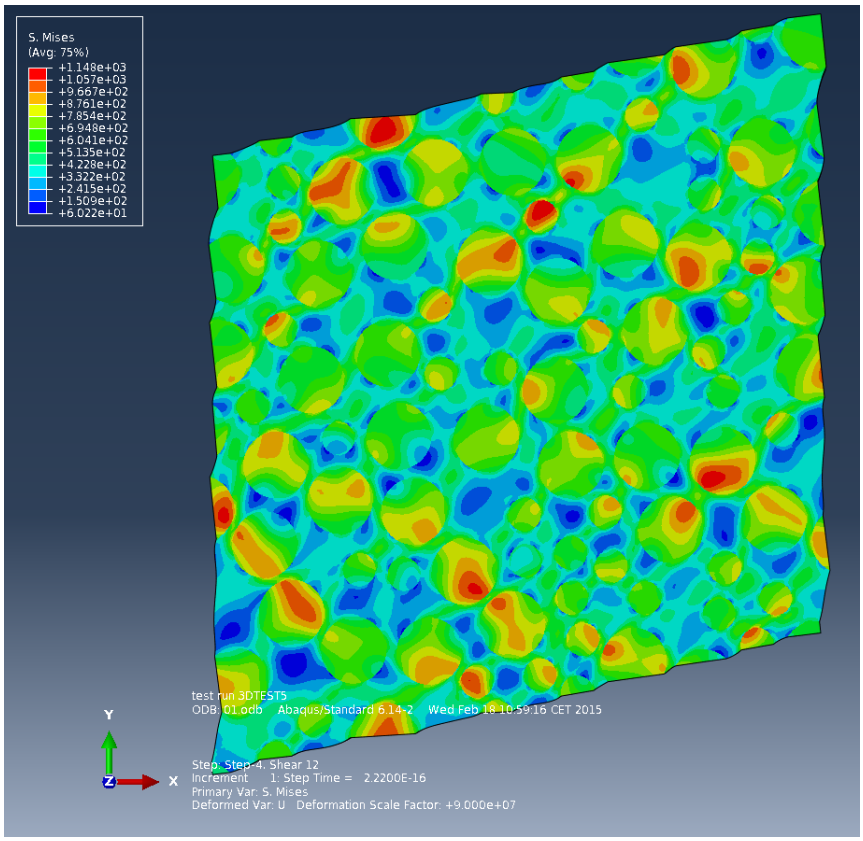

FIGURE 72: DEFORMED STATE AND MAP OF VON MISSES STRESS FOR TRANSVERSE SHEAR LOADING (FIBERS OF DIAMETER RATIO 1:2 AND VOLUME FRACTION 0.45)

In Figure 73 the map of the Von Misses stresses again is overlaid with a line plot of the load-free mesh. It can be observed in figures 72 and 73 that for transverse shear loading regions of concentrations of the Von Mises stress form when fibers are close neighbors in directions oriented approximately at +-45 degrees. Stresses again tend to be higher in fibers due to the latters' higher stiffness.

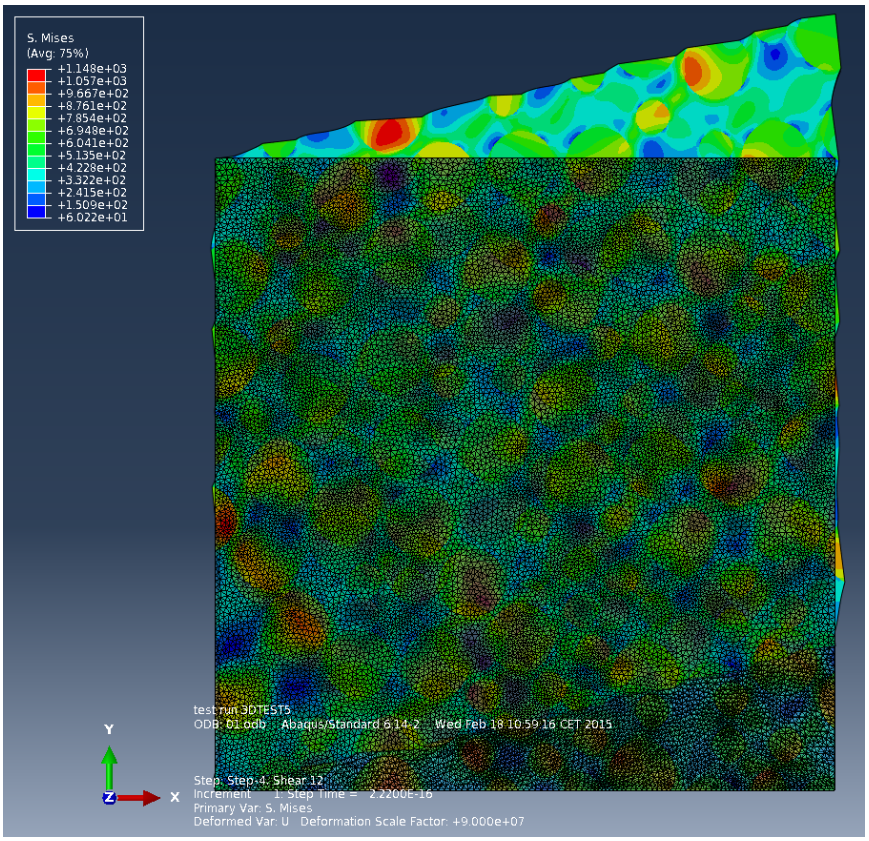

FIGURE 73: COMPARISON BETWEEN THE INITIAL AND DEFORMED STATES FOR UNIAXIAL TENSILE AXIAL LOADING (FIBERS OF DIAMETER RATIO 1:2 AND VOLUME FRACTION 0.45)

3.3.1.4 AXIAL SHEAR LOADING OF THE COMPOSITE

Two different load cases fall into this category, axial shear in the 1-3 and the 2-3 planes. The former can be obtained by applying a concentrated load acting in 1-direction on node SWT, whereas a load acting in 2-direction on the same master node gives rise to the latter load case.

Figures 74 and 75 show maps of the Von Mises stresses plotted on the deformed geometries for the two load cases, respectively. Nearly all the axial shear deformation can be seen to occur in the soft matrix. Both figures pertain to a volume fraction of 0.45 and a diameter ratio of 1:4.

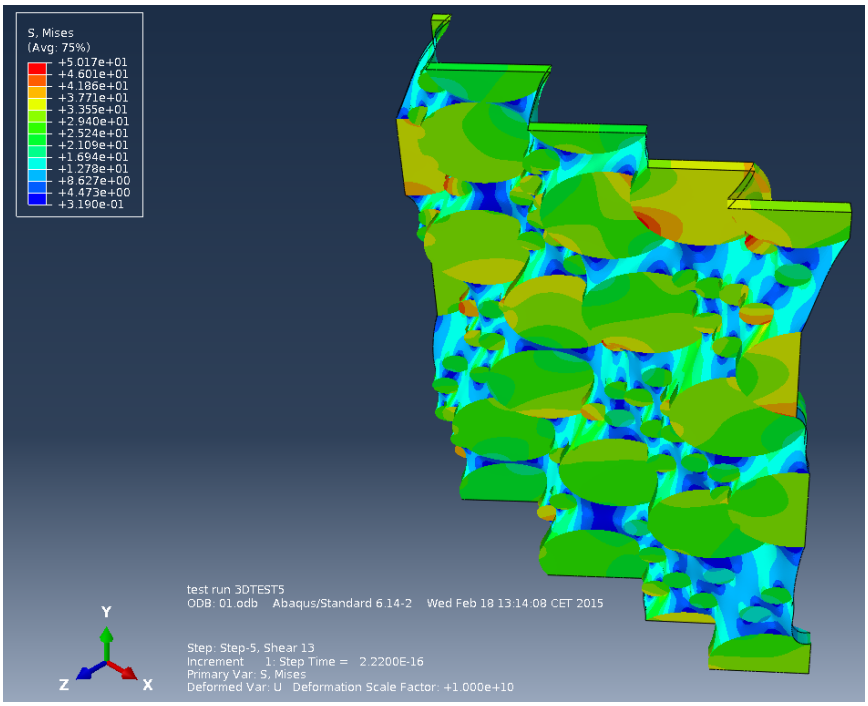

FIGURE 74: DEFORMED STATE AND MAP OF VON MISSES STRESS FOR AXIAL 1-3 SHEAR LOADING (FIBERS OF DIAMETER RATIO 1:4 AND VOLUME FRACTION 0.45)

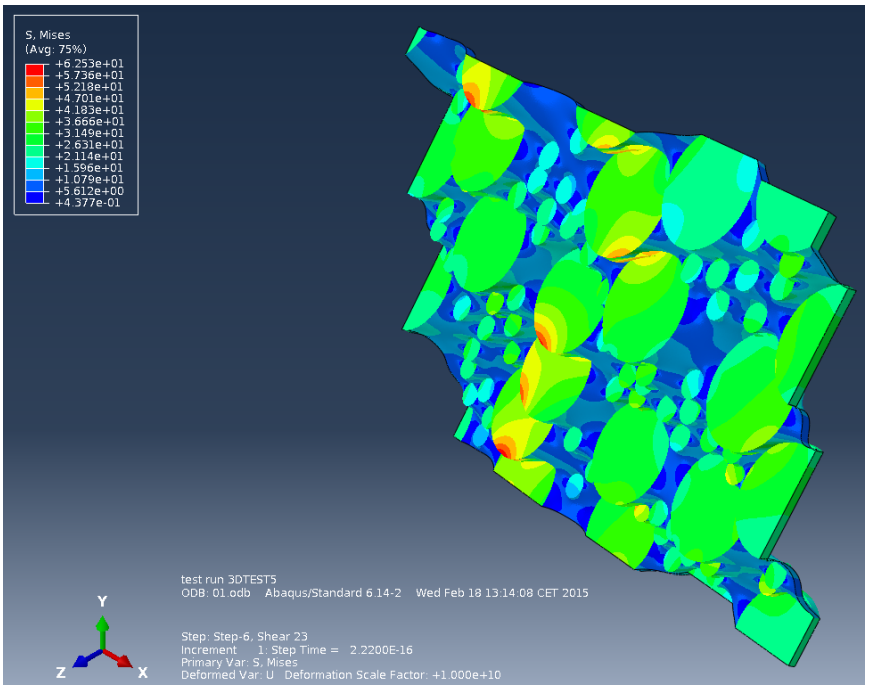

FIGURE 75: DEFORMED STATE AND MAP OF VON MISSES STRESS FOR AXIAL 2-3 SHEAR LOADING (FIBERS OF DIAMETER RATIO 1:4 AND VOLUME FRACTION 0.45)

3.3.1.5 THERMAL LOADING OF THE COMPOSITE

To apply the load case of free thermal expansion, no mechanical loads are applied on the volume element. Rather, it is subjected to a homogeneous increase in temperature, which leads to a slight expansion in the 1-, 2- and 3- directions. Even

though no macroscopic loads act on the unit cell, thermal stresses develop nevertheless, the reason being the different coefficients of thermal expansion of the matrix and fiber phases. Accordingly, the distribution of the Von Mises stress shown in Figure 76, which corresponds to a fiber volume fraction of 0.45 and a diameter ratio of 1:2 is rather inhomogeneous. The highest stresses can be seen to be generated at the interfaces between the fibers and matrix.

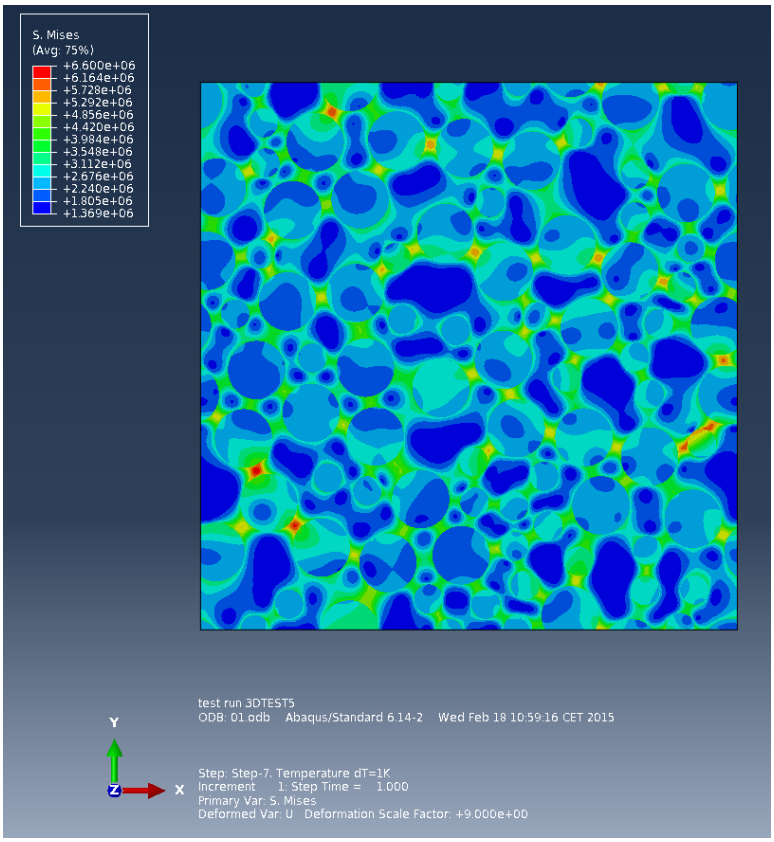

FIGURE 76: MAP OF VON MISSES STRESS UNDER THERMAL LOADING (FIBERS OF DIAMETER RATIO 1:2 AND VOLUME FRACTION 0.45)

3.3.2 POROUS MATERIAL

3.3.2.1 TRANSVERSE UNIAXIAL LOADING OF THE POROUS MATERIAL

As in the case of the composite material, the stresses tend to show horizontal regions of concentrations for uniaxial loading in X-direction and vertical ones for uniaxial loading in Y-direction. The figures below show a porous material with a 0.45 void volume fraction and a pore diameter ratio of 0.5.

Obviously, the loads applied to the porous unit cells are analogous to the ones used for describing corresponding load cases for the composite in section 3.3.1. Figure 77 shows the load-free and deformed configurations predicted for a material containing 45 vol.% of pores of diameter ratio 1:2 subjected to loading in the 1-

direction. Due to the vanishing stiffness of the pores they change their shapes to some extent. However, it is worth noting that the pore ovalisation evident in the following Figures is considerably exaggerated by scaling the displacements. Actually, these shape changes remain very modest in the elastic range displacements (note that, in fact, the present FE runs, do not account for geometrical nonlinearities and, accordingly, could not account for such large deformations).

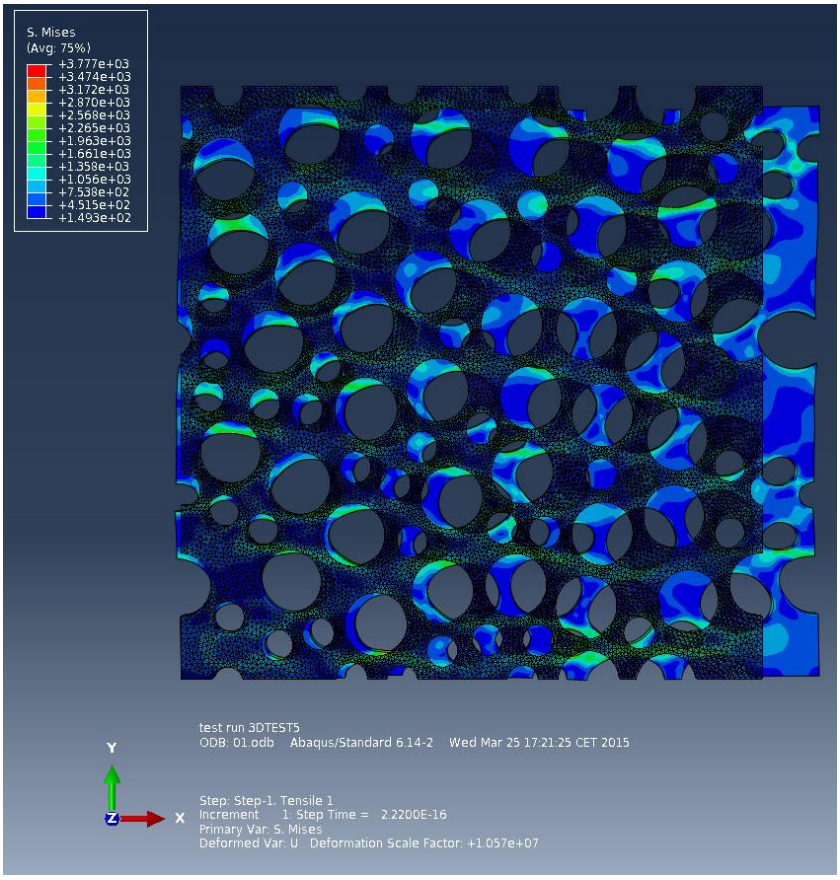

FIGURE 77: COMPARISON BETWEEN THE INITIAL AND DEFORMED STATES FOR UNIAXIAL TENSILE TRANSVERSE LOADING IN 1-DIRECTION (PORES OF DIAMETER RATIO 1:2 AND VOLUME FRACTION 0.45)

The corresponding results obtained for transverse tensile loading in 2-direction are presented in Figure 78.

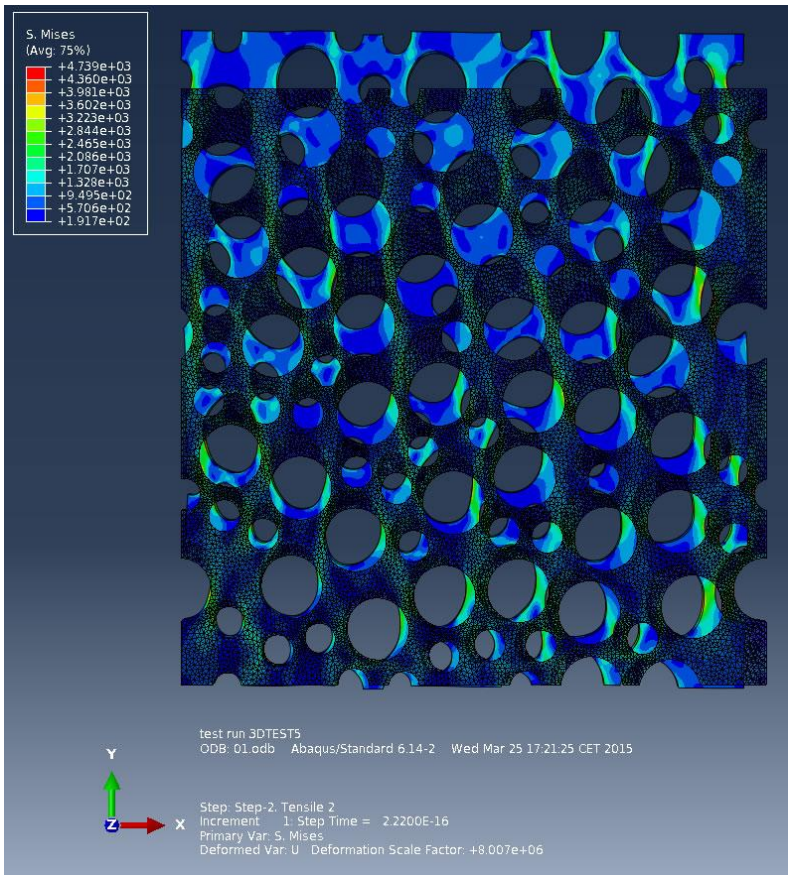

FIGURE 78: COMPARISON BETWEEN INITIAL AND DEFORMED STATES FOR THE UNIAXIAL TENSILE TRANSVERSE LOADING IN 2-DIRECTION (PORES OF DIAMETER RATIO 1:2 AND VOLUME FRACTION 0.45)

3.3.2.2 AXIAL UNIAXIAL LOADING OF THE POROUS MATERIAL

The uniaxial tensile axial load case is covered by figures 79 and 80, which again pertain to a pore volume fraction of 0.45 and a pore diameter ratio of 1:2. As expected, the unit cell shrinks in the 1-2 plane and expands in 3-direction. Due to the pores' vanishing stiffness a homogeneous stress state results for this load case.

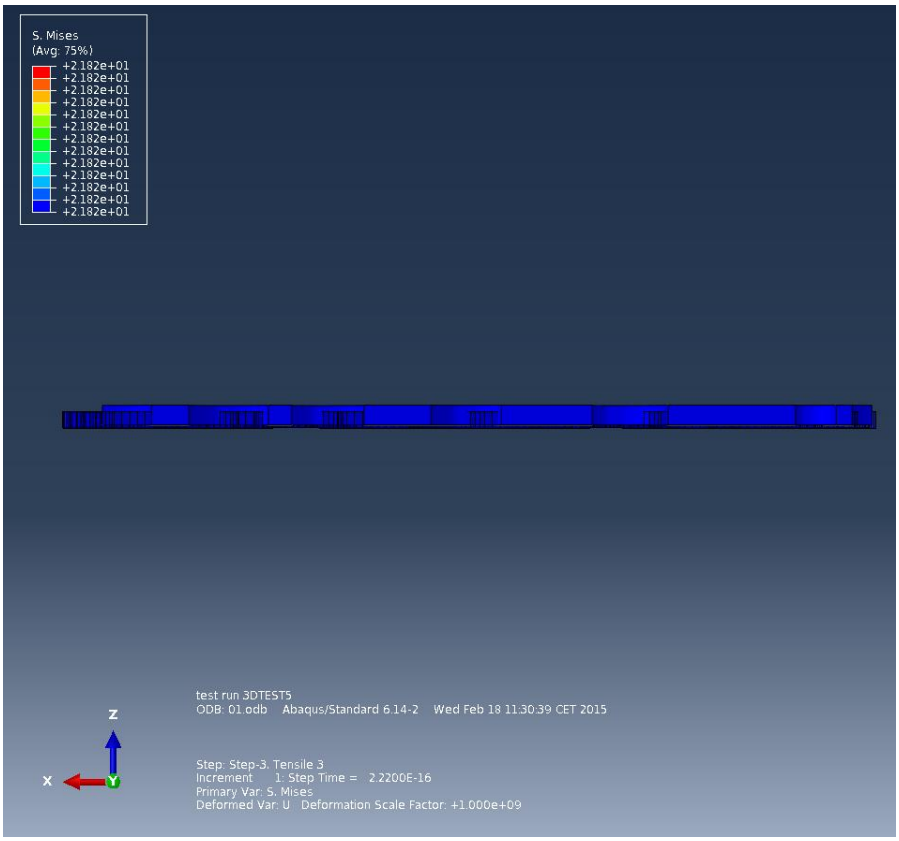

FIGURE 79: CHANGE IN THICKNESS IN 3-DIRECTION FOR UNIAXIAL TENSILE AXIAL LOADING (PORES OF DIAMETER RATIO 1:2, VOLUME FRACTION 0.45)

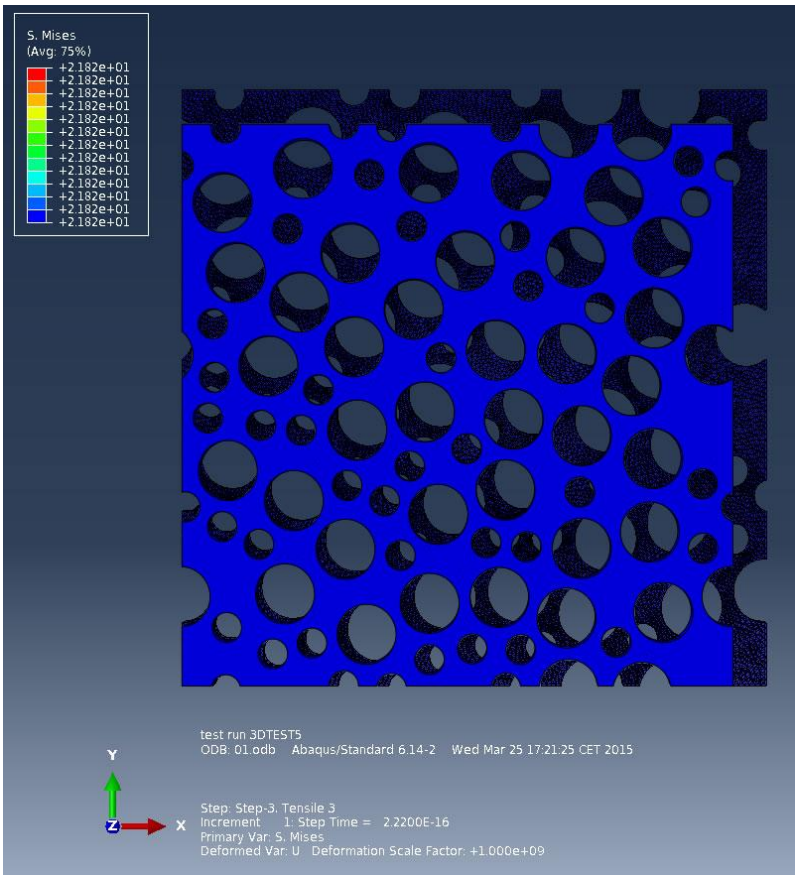

FIGURE 80: COMPARISON BETWEEN THE INITIAL AND DEFORMED STATES FOR UNIAXIAL TENSILE AXIAL LOADING (PORES OF DIAMETER RATIO 1:2, VOLUME FRACTION 0.45)

3.3.2.3 TRANSVERSE SHEAR LOADING OF THE POROUS MATERIAL

The behavior under transverse shear loading (i.e., shear in the 1-2 plane) is qualitatively similar to the one shown by the composite material. In Figure 81, again, regions of elevated equivalent stress are oriented at angles of approximately +-45 degrees. The deformation of the pores shows an analogous tendency. The figure corresponds to a void volume fraction of 0.45 and a diameter ratio of 1:2.

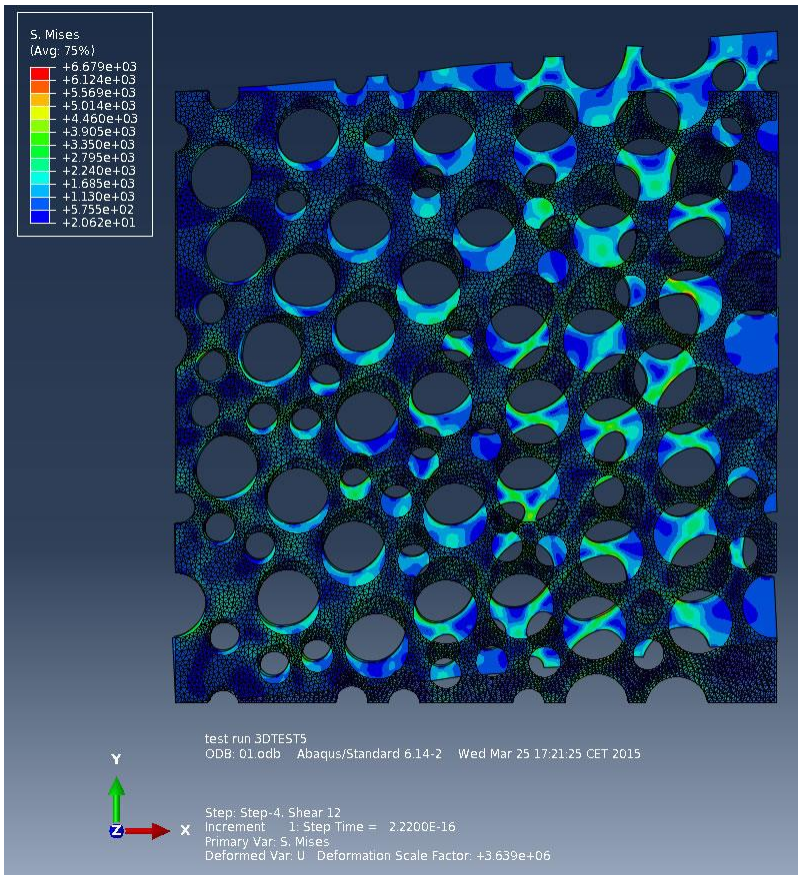

FIGURE 81: DEFORMED STATE AND MAP OF VON MISSES STRESS FOR TRANSVERSE SHEAR LOADING (PORES OF DIAMETER RATIO 1:2 AND VOLUME FRACTION 0.45)

3.3.2.4 AXIAL SHEAR LOADS

The behavior under axial shear loading is quite similar to, but maybe less dramatic than that of the composite discussed in section 3.3.1.4. Figure 82 shows predictions for shear in the 1-3-plane and Figure 83 for shear in the 2-3-plane. The maximum Von Mises stresses can be seen to occur in some the matrix bridges between closely approaching voids; these positions are quite different for the two load cases. The volume element again describes aligned cylindrical pores at a volume fraction of 0.45 and a diameter ratio of 1:2

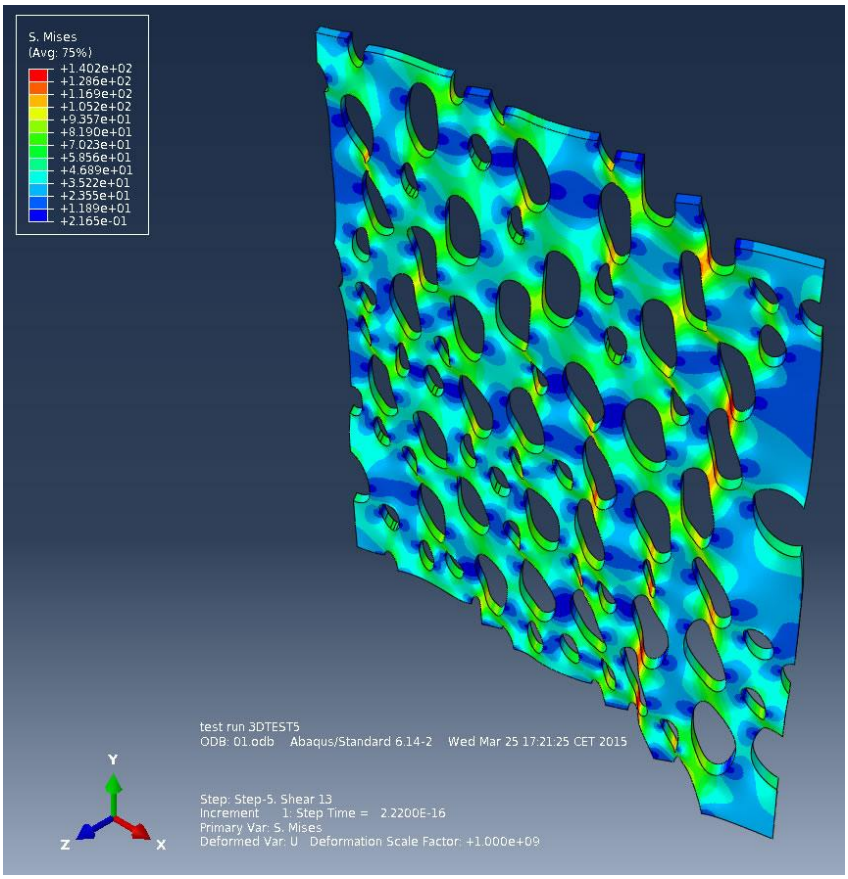

FIGURE 82: DEFORMED STATE AND MAP OF VON MISSES STRESS FOR AXIAL 1-3 SHEAR LOADING (PORES OF DIAMETER RATIO 1:2 AND VOLUME FRACTION 0.45)

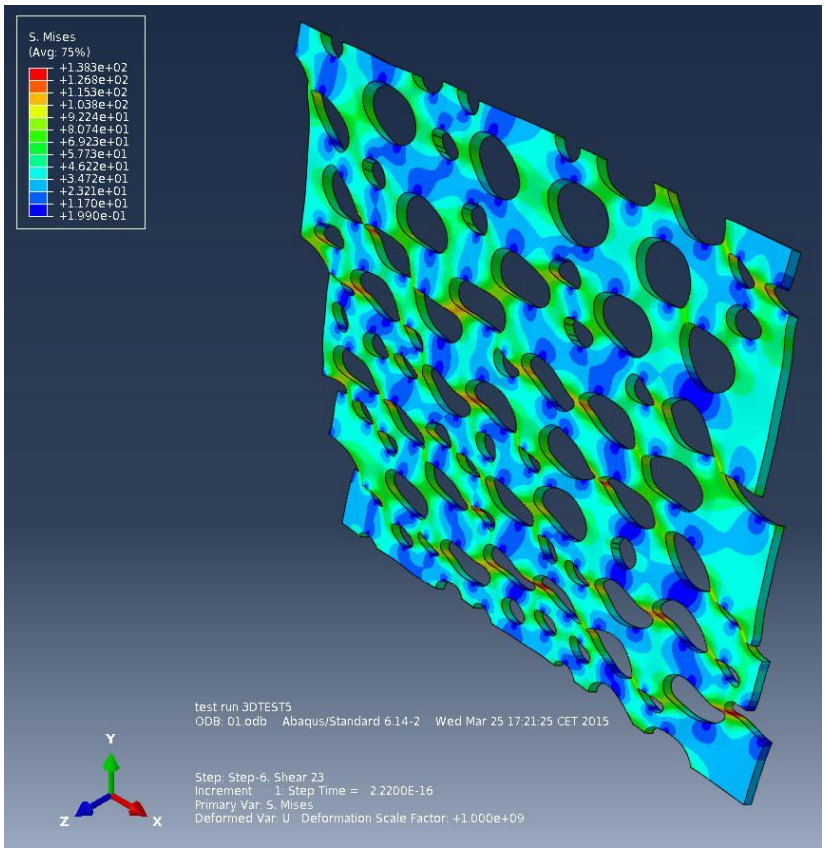

FIGURE 83: DEFORMED STATE AND MAP OF VON MISSES STRESS FOR AXIAL 2-3 SHEAR LOADING (PORES OF DIAMETER RATIO 1:2 AND VOLUME FRACTION 0.45)

3.3.2.4 THERMAL LOADING OF THE POROUS MATERIAL

Finally, Figures 84 and 85 show the deformed shape and Von Mises stresses obtained for free thermal expansion of a porous material with void volume fraction 0.45 and a diameter ratio of 1:2.

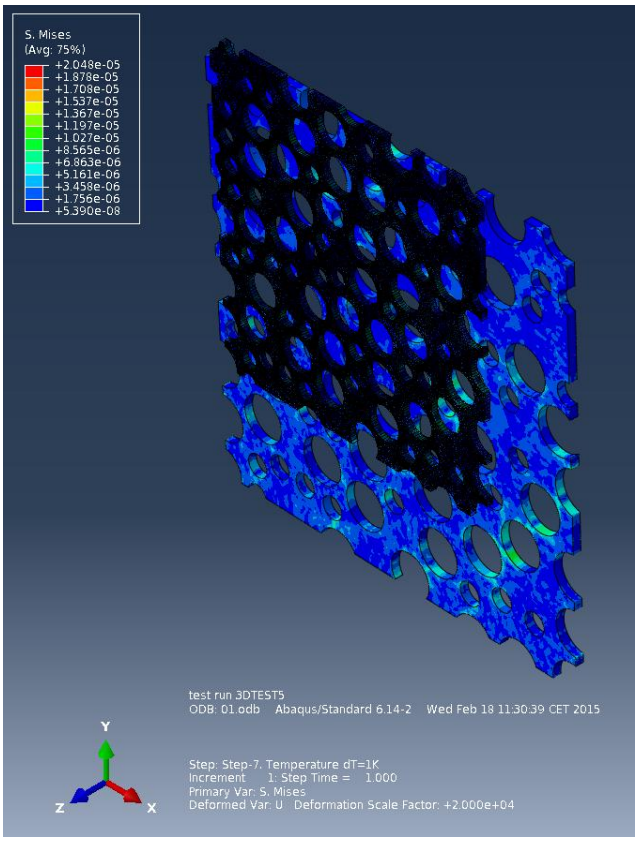

FIGURE 84: MAP OF VON MISSES STRESS UNDER THERMAL LOADING (PORES OF DIAMETER RATIO 1:2 AND VOLUME FRACTION 0.45)

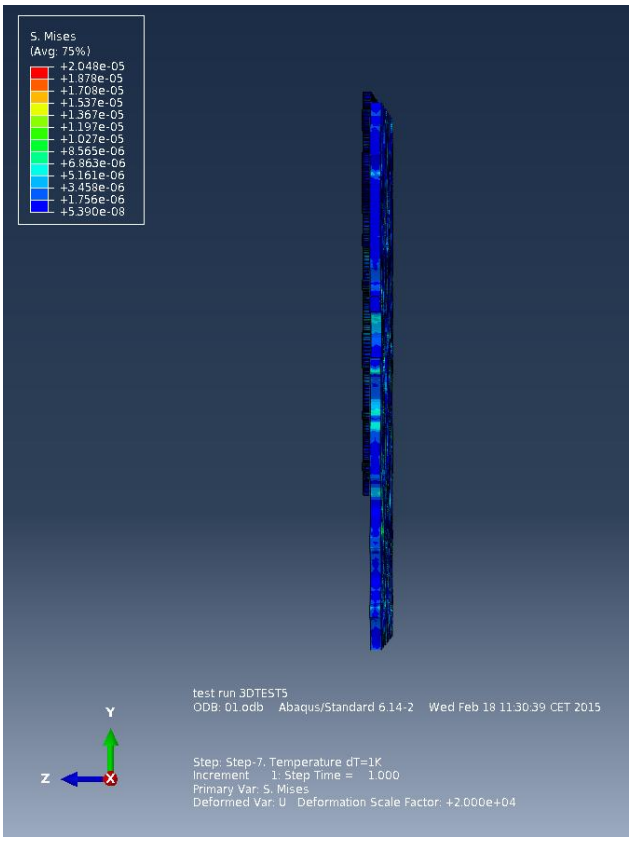

FIGURE 85: CHANGE IN THICKNESS IN 3-DIRECTION FOR THERMAL LOADING (PORES OF DIAMETER RATIO 1:2, VOLUME FRACTION 0.45)

CONCLUSIONS

The effects of the relative sizes of inhomogeneities were observed to be small. Some minor differences in the macroscopic elastic behavior appeared due to the influence of relative fiber diameter ratio, but they cannot be said to be relevant for practical issues.

Transverse elastic and shear moduli give similar behaviors, showing dependence on the relative sizes of inhomogeneities for both the composite and porous materials. To end with, the transverse bulk modulus and the transverse Poisson's coefficient show some minor dependence on the relative sizes of inhomogeneities only for some volume fractions.

It must be kept in mind that the small effects were found due to the specialized tools available at the institute where the thesis was done. These effects cannot be captured with standard tools that companies use for evaluating effects of inhomogeneities. However, there is no practical need to do so either, as these effects are irrelevant for most practical fields outside research.

REFERENCES

[1] Chawla KK. Composite Materials: Science and Engineering. *Springer, New York, 1987.*

[2] Schier JF, Juergens RJ. Design impact of composites on fighter aircraft. Pt.1. They force a fresh look at the design process. *Astronautics Aeronautics*., *21:44–49, 1983*

[3] Chawla KK. Fibrous materials. *Cambridge University Press, Cambridge,2008.*

[4] Böhm HJ. A short introduction to basic aspects of continuum micromechanics. *ILSB Report 206 Institute of Lightweight Design and Structural Biomechanics, Vienna University of Technology, Vienna, Austria. 1998 (updated 2014).*

[5] Mishnaevsky LL, Schmauder S. Continuum mesomechanical finite element modeling in materials development: A state-of-the-art review. *Appl.Mech.Rev. 54:49–67, 2001.*

[6] Papadopoulos P. Introduction to the Finite Element Method. *University of Berkeley, Berkeley, CA, 2010. URL: http://www.me.berkeley.edu/ME280A/chapter1.pdf*

[7] Böhm HJ. ARIGEN documentation. *Institute of Lightweight Design and Structural Biomechanics, Vienna University of Technology, Vienna, Austria, 2014*.

[8] Geuzaine C, Remade JF. Gmsh: a three-dimensional finite element mesh generator with built-in pre- and post-processing facilities. *Version 2.8.5, July 9, 2014. URL: geuz.org/gmsh*

[9] Pahr DH. Introduction to Finite Element Methods in Solid Mechanics. *Course Notes, Institute of Lightweight Design and Structural Biomechanics, Vienna University of Technology, Vienna, Austria, 2014.*

[10] Pahr DH. Overview of Medtool 3.7. *Institute of Lightweight Design and Structural Biomechanics, Vienna University of Technology, Vienna, Austria, 2014.*

[11] Böhm HJ. COMPCOMP documentation. *Institute of Lightweight Design and Structural Biomechanics, Vienna University of Technology, Vienna, Austria, 2014*.

[12] From *http://www.3ds.com/products-services/simulia/products/abaqus/*

[13] From http://www.mscsoftware.com/training_videos/patran/Reverb_help/index.html#page/Functional%20Assignments/materials_forms.5.6.html

[14] Corcolle R. Comparison between different approaches in homogeneization: Mean-field approach vs full-field approaches*. Proceedings of COMPUMAG 2013, Budapest, Hungary, 2013.*

[15] From http://www-f1.ijs.si/~vilfan/SM/ln4a.pdf

[16] Hashin Z. The elastic moduli of heterogeneous materials. *J.Appl.Mech.*, 29:143–150, 1962.

[17] Davis LC. Flow rule for the plastic deformation of particulate metal matrix composites. *Comput.Mater.Sci.*, 6:310–318, 1996.

[18] Torquato S. Random heterogeneous media: Microstructure and improved bounds on effective properties. *Appl.Mech.Rev.*, 44:37–75, 1991.

[19] Kanit T, Forest S, Gallier I, Mounoury V, Jeulin D. Determination of the size of the representative volume element for random composites: Statistical and numerical approach. *Int.J.Sol.Struct.*, 40:3647–3679, 2003.

[20] Smit RJM, Brekelmans WAM, Meijer HEH. Prediction of the mechanical behavior of non-linear heterogeneous systems by multi-level finite element modeling. *Comput. Meth.Appl.Mech.Engng.*, 155:181–192, 1998

[21] From http://machinedesign.com/news/closer-look-model-meshing

[22] Böhm HJ. Composites Engineering, Part II. *Course Notes, Institute of Lightweight Design and Structural Biomechanics, Vienna University of Technology, Vienna, Austria, 2014.*

[23] Torquato S. Random Heterogeneous Materials. *Springer, New York, 2002.*

[24] Moakher M, Norris AN. The closest elastic tensor of arbitrary symmetry to an elastic tensor of lower symmetry. *J.Elast., 82:273–296, 2006.*

[25] Segurado J. Micromecánica computacional de materiales compuestos reforzados con partículas. *Doctoral Thesis, Universidad Politécnica de Madrid, Madrid, Spain, 2004.*

[26] Torquato S, Lado M. Improved bounds on the effective moduli of random arrays of cylinders. *J.Appl. Mech., 59:1–6, 1992.*